Diss. ETH No. 21514

EMF Risk Assessment: Exposure Assessment and Safety Considerations in MRI and other Environments

A dissertation submitted to the

ETH ZURICH

for the degree of

DOCTOR OF SCIENCES
(Dr. sc. ETH Zurich)

presented by

MANUEL JOHANNES MURBACH
Master of Science, ETH Zurich
born July 26, 1979
citizen of Zurich ZH

accepted on the recommendation of

Prof. Dr. K. P. Prüssmann, examiner
Prof. Dr. N. Kuster, Prof. Dr. T. Samaras, co-examiners

2013

– it's in between,
where complexity kicks in.

Contents

Summary **xiii**

Zusammenfassung **xvii**

Acknowledgments **xxi**

1 Introduction **1**
1.1 Exposure To Electromagnetic Fields 1
1.2 Electromagnetic Spectrum 2
1.3 Outline of the Thesis 3

I Radiofrequency Exposure and Safety Issues in Magnetic Resonance Imaging **7**

2 Background in MRI Safety **9**
2.1 Motivation and Objectives 9
2.2 Magnet Resonance Imaging (MRI) 10
2.3 The B1 field in MRI 11
2.4 RF Exposure in MR 12
2.5 Limiting RF Exposure, IEC Standard 16
2.6 Modeling of the Incident B1 Field 17
2.7 RF Shimming and Multitransmit Coils 20
2.8 RF Simulations with Human Anatomical Models . . . 22
2.9 Human Thermoregulation 23
2.9.1 Whole-Body Thermoregulation 23

2.9.2 Local Thermoregulation 24
2.10 Thermal Simulations 25
2.11 Thermal Dose (CEM43) and Damage Thresholds . . 25
2.12 Validation Methods 27
2.13 Safety Standard and History of Safe Use (HoSU) . . . 28

3 Incident Field Measurements and Classification of MRI Field Generating Units 29
3.1 Objectives 29
3.2 Selected MR Systems 29
3.3 Methods 31
3.3.1 RF Measurement Protocol 31
3.3.2 Measurement Phantoms, Jigs and Grid 31
3.3.3 Measurement Equipment 32
3.3.4 RF Test Sequence and Probe Calibration . . . 32
3.3.5 Data Evaluation 35
3.4 Results 35
3.5 Conclusions 36

4 Local SAR Enhancements in Anatomically Correct Children and Adult Models as a Function of Position within 1.5 T MR body coil 41
4.1 Abstract 41
4.2 Introduction 42
4.3 Methods 44
4.3.1 Simulation Configuration 44
4.3.2 Electromagnetic Simulation 46
4.3.3 Data Evaluation 47
4.4 Results 48
4.5 Uncertainty Analysis 52
4.6 Discussion and Conclusion 52

5 Whole–Body and Local RF absorption in Human Models as a Function of Anatomy and Position within 1.5T MR Body Coil 55
5.1 Abstract 55
5.2 Introduction 56
5.3 Methods 58

5.4 Results 61
5.5 Numerical Uncertainty 64
5.6 Discussion 66
5.7 Conclusion 68
5.8 Acknowledgements 69

6 Thermal Damage Tissue Models Analyzed for Different Whole-Body SAR and Scan Duration for Standard MR Body Coils 71
6.1 Abstract 71
6.2 Introduction 72
6.3 Methods 74
6.3.1 Anatomical Models and Simulation Scenario . 74
6.3.2 Tissue Properties and Local Thermoregulation 75
6.3.3 Electromagnetic and Thermal Simulation . . . 78
6.3.4 Data Evaluation 81
6.3.5 Thermal Doses (CEM43) and Damage Threshold Levels 82
6.3.6 Experimental Validation 83
6.4 Results 84
6.5 Numerical Uncertainty 87
6.6 Discussion & Conclusion 92
6.7 Acknowledgements 96

7 Outlook 97
7.1 Future Concepts for MRI Safety Standards 97
7.2 Compliance with Thermal (Dose) Based Safety Standards. 99
7.2.1 Pre-Scan Evaluation Methods 99
7.2.2 On-The-Fly Estimations 100
7.2.3 On-The-Fly Monitoring, MRI Thermometry . . 100
7.3 Challenges in Parallel Transmit MRI 101
7.4 Challenges in High Field MRI 102

II Exposure Assessment in Human for Health

Risk Research **103**

8 Background in Human RF Provocation Studies **105**
8.1 Motivation and Objectives 105
8.2 Mobile Phone Exposure 106
8.3 Non-Thermal Effects 107
8.3.1 Effect on EEG Spectral Power 108
8.3.2 Effect on Sleep-Dependent Performance Improvement 110
8.4 Hypothesized Interaction Mechanisms 111

9 Flexible Human Exposure System for Hypothesis Driven EMF Research **113**
9.1 Abstract 113
9.2 Introduction 114
9.3 Objectives 114
9.4 Methods 115
9.5 Validation 118
9.6 Results 118
9.7 Study Configurations 122
9.8 Uncertainty 122
9.9 Conclusions 123

10 Evaluation of Electrode Artifacts and Thermal Ripples of EEG RF Experiments **125**
10.1 Abstract 125
10.2 Introduction 126
10.3 Methods 128
10.3.1 Setup A: Flat homogeneous model 131
10.3.2 Setup B: Flat tissue layered head model 131
10.3.3 Setup C: Homogeneous SAM model 131
10.3.4 Setup D: Anatomical model Ella 132
10.4 Results 133
10.4.1 Setup A: Flat homogeneous model 134
10.4.2 Setup B: Flat tissue layered head model 134
10.4.3 Setup C: Homogeneous SAM model 134
10.4.4 Setup D: Anatomical model Ella 137
10.4.5 Translation of RF pulses to ΔT ripples 140

10.4.6 Uncertainty Analysis 140
10.4.7 Discussion and Conclusion 143

11 Stimulation of the brain with radiofrequency electromagnetic field pulses affects sleep-dependent performance improvement 145
11.1 Abstract 145
11.2 Introduction 146
11.3 Materials and methods 148
11.3.1 Subjects 148
11.3.2 Procedure 148
11.3.3 Exposure setup 149
11.3.4 EEG recordings 150
11.3.5 Spectral analysis 151
11.3.6 Event-related spectral power (ERSP) and intertrial coherence (ITC) 151
11.3.7 Motor performance 152
11.3.8 Statistics 153
11.4 Results 154
11.4.1 Minor effects of RF EMF exposure on sleep architecture 154
11.4.2 RF EMF changed EEG spectral power during NREM sleep 154
11.4.3 Induction of SWA by pulsed RF EMF 155
11.4.4 RF EMF exposure affected sleep-dependent motor performance improvement 158
11.5 Discussion 160
11.6 Supplementary Materials 163
11.6.1 Exposure Setup 163
11.6.2 Dosimetric Evaluation 164
11.6.3 Exposure Condition 165

12 Outlook 167
12.1 Current Status of EMF Sleep Research 167
12.2 Interaction Mechanisms 167
12.3 Future Research 168

III Epilogue **171**

13 Conclusions **173**

IV Appendix **177**

A List of Acronyms **179**

B List of Symbols **181**

C List of Publications **183**
C.1 Journal Publications Included in this Thesis 183
C.2 Other Journal Publications 184
C.3 Other Publications 185

Bibliography **195**

Curriculum Vitae **213**

Summary

Elevated levels of electromagnetic radiation in the MHz region (VHF – UHF, 30 – 3000 MHz) have been around for only little longer than a century. Before Heinrich Hertz generated the first 40 MHz radiation in 1886 — proving their existence predicted by James Maxwell in 1864 — electromagnetic exposure of living creatures below the spectrum of the sunlight (THz region) and above (quasi) static fields was limited to thunderstorms and thermal atmospheric and cosmic background noise . It is not surprising that we do not have any natural sense for this dimension of radiation.

Nowadays, a culmination of technical developments has changed the situation dramatically. Human made electromagnetic fields (EMF) may reach high levels and are omnipresent. Thus, it's adequate to carefully evaluate all possible safety issues, especially since the effects of radiation on the higher side of the spectrum (X-rays) had been dramatically underestimated.

Currently, the highest exposures for "Joe Public" originate from (1) mobile communication devices operating on the GSM, UMTS, or DECT standard of ca. 900 and 1900 MHz, and (2) in the clinical environment, inside a magnet resonance imaging (MRI) scanner, typically at 64 or 128 MHz.

In contrast to X-rays, the quantized energy of EMF in the MHz region is not sufficient to directly interact with biomolecules such as DNA, and is thus referred to as non-ionizing radiation (NIR). The main and undisputed safety-relevant effect of which is the heating of conductive lossy matter, e.g., most biological tissues. Potential effects of mobile phone exposure have usually been referred to as "non-

thermal biological response", as the EMF-induced temperature increases are very small and considered biologically non-relevant. The scientific and societal debate about adverse (or beneficial) non-thermal effects is still ongoing. These two different safety concerns (thermal and non-thermal) are reflected in the two parts of my thesis.

Part I addresses unresolved issues in EMF exposure assessment and evaluations for patients in an MRI environment, covering the whole chain of interaction.

Chapter 3 describes the assessment of the radiofrequency (RF) incident field distributions in typical MRI scanners, which has closed a crucial gap for the classification of existing RF field distributions. As coil design is partially considered to be trade secrets by the MRI manufacturers, typical field patterns and inter-brand comparisons were not available. Measurement procedures were defined and suitable equipment was selected for appropriate RF field assessments. The measurement results provide a gross overview of currently utilized coil geometries and field distributions. Large variations in applied electric field levels have been found, strongly depending on the bore size.

Human RF energy absorption is investigated in Chapters 4 & 5 as a function of different MRI positions for various anatomical human models, and as a correlation to human anatomy. These studies provide profound insights into the specific RF absorption mechanisms in MRI. High local levels of the 10 g-averaged peak spatial specific absorption rate (psSAR10g) were found for torso imaging positions (> 80 W/kg) in the allowed MRI operating modes. The psSAR10g levels have a spread of a factor of 3 that correlates with gross body metrics (larger patients have higher local exposure), and can increase by factor $\gg 2$ when forming anatomical RF loops.

Chapter 6 addresses the RF-induced thermal load and potential thermal tissue damage in MRI exposures. The vast thermal parameter space has been fathomed by investigating the impact of thermal tissue properties, basal and thermoregulated blood perfusion, thermal boundary conditions (sweating, airflow), accumulation of thermal dose, and tissue damage thresholds. The human body has a pronounced ability to maintain a stable core temperature, even at the high overall exposure levels in MRI. For local body temperatures, our results indicate a strong dependence on the local thermoregulation

abilities by means of increased local vasodilation. The accumulated thermal dose (CEM43) points towards safe MR scantimes on the order of one hour for realistic scan scenarios. Full exploitation of the exposure limits defined in the product standards may result in thermal tissue damage; a revision of the corresponding standards is suggested.

Part II is dedicated to research on effects of low-level EMF in humans, which are believed to be of a non-thermal nature, due to the small temperature increases below 0.6°C. Besides the hardware equipment and control software, the well-defined EMF exposure of volunteers requires a detailed dosimetric assessment and a profound investigation on all potential confounders.

Adequate EMF exposure equipment for innovative research in human provocation studies are presented in Chapter 9. Exposure levels and patterns for both RF and extremely low frequency (ELF) fields, are estimated in detail and are validated experimentally. The assessment included functional subregions of the brain, as well as two different RF frequencies and a comparison to older exposure equipment for the integration of former study conclusions.

Chapter 10 is dedicated to a specific potential confounder, assessing the effect of electroencephalographic (EEG) electrodes and their leads within the RF field. This addresses concerns expressed by several members of the scientific community, and it is particularly important, as many studies applied EMF exposure with attached EEG electrodes. The various simulation and measurement results of this study indicate that neither the locally enhanced field levels, the subsequent temperature increase around the electrodes, nor the temperature ripples from RF pulsing is a plausible explanation for the observed EMF effects in humans.

Finally, the Chapter 11 portrays a full human provocation study, assessing the effect of EMF by the means of sleep EEG recording and sleep-dependent performance improvement. In this joint project with the University Children's Hospital of Zurich, my part was to provide a novel all–night EMF exposure system based on a circularly polarized patch antenna. Evaluation of the sleep EEG showed an increased slow-wave activity towards the end of the sleep period and also after the RF EMF bursts in event-related EEG spectral power and phase changes. Sleep-dependent performance improvement after overnight

RF EMF exposure was significantly reduced (–20%, P = 0.03) compared to the sham overnight treatment.

The Chapters 4 – 6 and 9 – 11 have been published in peer-reviewed journals and were presented to standards building bodies and government agencies. The MT40 group working on the MRI product standard IEC 60601-2-33 is integrating the findings in future revisions.

After a general introduction to EMF (Chapter 1), Parts I & II begin with backgrounds of their specific topics and conclude with an outlook comprising future developments and challenges.

Zusammenfassung

Erhöhte Pegel elektromagnetischer Strahlung im MHz-Bereich (VHF – UHF, 30 – 3000 MHz) gibt es noch nicht viel länger als ein Jahrhundert. Nachdem James Maxwell im Jahr 1864 diese Art von elektromagnetischen Feldern vorausgesagt hatte, war es Heinrich Hertz der die erste 40 MHz Strahlung generierte. Zuvor war die Exposition von Lebewesen ausserhalb der Spektren von Sonnenlicht (THz Region) und (quasi) statischen Feldern beschränkt auf das thermisch atmosphärische und kosmische Hintergrundrauschen. So überrascht es nicht, dass wir kein Sensorium für diese Dimension von Strahlung entwickelt haben.

Heutzutage hat der technologische Fortschritt die Situation grundlegend verändert. Künstliche elektromagnetische Felder (EMF) können sehr hohe Niveaus erreichen und sind omnipräsent. Deshalb ist es durchaus ratsam, alle möglichen Sicherheitsrisiken gründlich auszuloten, zumal die Gesundheitseffekte im höheren Bereich des Spektrums (Röntgenstrahlen) drastisch unterschätzt wurden.

Im Moment werden die höchsten Strahlenbelastungen für den Durchschnittsbürger verursacht von (1) mobilen Kommunikationsgeräten im GSM, UMTS oder DECT Standard bei ca. 900 oder 1900 MHz, und (2) von Kernspin Tomographen (Magnetresonanz Imaging, MRI) in einem klinischen Umfeld, typischerweise bei 64 oder 128 MHz.

Im Gegensatz zur Röntgenstrahlung ist die quantifizierte Energie von EMF in der MHz Region viel zu klein, um direkt mit biologischen Molekülen — z.B. mit der DNS — zur interagieren. Deshalb wird diese Strahlung als nicht-ionisierend (NIR) bezeichnet. Ihre unstrittig anerkannte Wirkung ist die Erhitzung von verlustbehafteten Materialien,

also von fast allen biologischen Geweben. Mögliche Effekte der Strahlung von Mobiltelefonen werden üblicherweise als “nicht-thermische biologische Reaktion” bezeichnet, da die EMF-induzierten Temperaturerhöhungen sehr klein sind, und als biologisch nicht-relevant erachtet werden. Die wissenschaftliche und soziale Debatte über schädliche (oder auch nützliche) nicht-thermische Effekte ist noch immer im Gange. Diese zwei unterschiedlichen Sicherheitsbedenken (thermisch und nicht-thermisch) reflektieren sich in den zwei Teilen meiner Doktorarbeit.

Teil I widmet sich wenig geklärten Belangen in der Beurteilung und Einschätzung der elektromagnetischen Exposition von Patienten in Kernspin Tomographen. Dabei wird die nötige Bandbreite abgedeckt, von der Feld Erzeugung bis zur möglichen thermischen Gewebeschädigung.

Kapitel 3 beschreibt die Beurteilung von einfallenden radiofrequenz (RF) Feldern in typischen MRI Apparaten. Dies schliesst eine entscheidende Lücke in der Klassifizierung von bestehenden RF Feldverteilungen. Da das Design von MRI Spulen von den Herstellern teilweise als Geschäftsgeheimnis gehandhabt wird, waren typische Feldmuster und Vergleiche zwischen Topographen nur bedingt verfügbar. Messverfahren wurden definiert und MRI kompatibles Messequipment selektiert für eine zweckdienliche Felddaten-Erhebung. Die Resultate geben eine grobe Übersicht von den derzeitig verwendeten Spulengeometrien und Feldverteilungen. Es wurden grosse Unterschiede der elektrischen Feldpegel gefunden, besonders in Abhängigkeit vom Röhrendurchmesser.

Die RF Energie Absorption im Menschen wurde im Kapitel 4 & 5 untersucht, dies in Abhängigkeit von unterschiedlichen Bildgebungs-Positionen in verschiedenen anatomischen Modellen und als Korrelation zur menschlichen Anatomie. Diese Studien erlauben einen tiefschürfenden Einblick in die spezifischen Absorptions-Mechanismen in MRI Geräten. Hohe lokale Werte in der 10 g gemittelten räumlichen spezifischen Absorptionsrate (psSAR10g) wurden gefunden in Torso Scan-Positionen (> 80 W/kg) innerhalb der erlaubten MRI Operations-Modi. Die psSAR10g Werte sind um einen Faktor 3 verteilt und korrelieren mit generellen Körpergrössen (grössere Patienten haben eine grössere lokale Exposition). Das Formieren von sogenannten RF-

Schleifen kann die lokale Exposition nochmals um einen Faktor $\gg 2$ erhöhen.

Kapitel 6 befasst sich mit den RF induzierten Temperaturbelastung und der potenziell daraus resultierenden thermischen Gewebeschädigung. Der gewaltige Parameter-Raum wurde ausgelotet durch Untersuchung der Einflüsse von thermischen Gewebeeigenschaften, von der basalen und thermoregulierten Blutperfusion, der thermischen Randbedingungen (Transpiration, Atmung), der Akkumulation der thermischen Dosis und durch das Anwenden von gewebespezifischen Schädigungs-Schwellenwerten. Der menschliche Körper hat eine ausgeprägte Fähigkeit, die innere Körpertemperatur konstant zu halten, sogar bei den hohen Expositionen im MRI. Für die lokalen Temperaturen zeigen unsere Resultate eine starke Abhängigkeit von der lokalen Thermoregualtion, welche sich vor allem durch einen erhöhten Blutfluss in den lokal erweiterten Gefässen auszeichnet. Die Auswertung der kumulierten thermischen Dosis (CEM43) deutet auf thermisch unbedenkliche Scanzeiten in der Grössenordung von einer Stunde für realistische MRI Scan-Szenarien. Werden jedoch die in den Produktstandards festgelegten Expositionslimiten bis zum Äussersten ausgereizt, können thermische Gewebeschädigungen nicht ausgeschlossen werden; deshalb wird eine Revision der entsprechenden Standards empfohlen.

Teil II setzt sich mit den Effekten von tiefen EMF Expositionen auf den Menschen auseinander, welche aufgrund der kleinen Temperaturanstiege — üblicherweise unter 0.6°C — als nicht-thermisch eingestuft werden. Neben den ganzen Gerätschaften und der Kontrollsoftware benötigt eine klar definierte Exposition von Versuchspersonen eine detaillierte dosimetrische Beschreibung und eine rigorose Überprüfung aller möglichen Störfaktoren.

Geeignetes Equipment für innovative Forschungsstudien am menschen wird in Kapitel 9 vorgestellt. Die Expositionsbelastungen sowie die Feldverteilungen in RF und extrem tieffrequenten (ELF) Feldern werden im Detail bestimmt und mittels Experimenten validiert. Funktionellen Subregionen im Gehirn wurden muteinbezogen, ebenso wie verschiedene RF Frequenzen und ein Vergleich zu früheren Systemen.

Das Kapitel 10

is dedicated to a specific potential confounder, assessing the effect of electroencephalographic (EEG) electrodes and their leads within

the RF field. This addresses concerns expressed by several members of the scientific community, and it is particularly important, as many studies applied EMF exposure with attached EEG electrodes. The various simulation and measurement results of this study indicate that neither the locally enhanced field levels, the subsequent temperature increase around the electrodes, nor the temperature ripples from RF pulsing is a plausible explanation for the observed EMF effects in humans.

Finally, the Chapter 11 portrays a full human provocation study, assessing the effect of EMF by the means of sleep EEG recording and sleep-dependent performance improvement. In this joint project with the University Children's Hospital of Zurich, my part was to provide a novel all–night EMF exposure system based on a circularly polarized patch antenna. Evaluation of the sleep EEG showed an increased slow-wave activity towards the end of the sleep period and also after the RF EMF bursts in event-related EEG spectral power and phase changes. Sleep-dependent performance improvement after overnight RF EMF exposure was significantly reduced (–20%, $P = 0.03$) compared to the sham overnight treatment.

The Chapters 4 – 6 and 9 – 11 have been published in peer-reviewed journals and were presented to standards building bodies and government agencies. The MT40 group working on the MRI product standard IEC 60601-2-33 is integrating the findings in future revisions.

After a general introduction to EMF (Chapter 1), Parts I & II begin with backgrounds of their specific topics and conclude with an outlook comprising future developments and challenges.

Acknowledgments

This thesis represents my 5 years of work at the IT'IS Foundation as a PhD Student. It's been a extraordinarily great and challenging time, and at first, I'd like to thank my friends and family — and those friends that became family — for their unconditional support. And thank you, Salome, for being awesome.

I was warned not to join the IT'IS Foundation from several sides. But I'm grateful that I did. I started working at Zeughausstrasse 43 in February 2007, and enrolled for the PhD program in 2008. It's been a fascinating culmination of people, knowledge, and spirit.

I'd like to thank the director of the IT'IS Foundation, Prof. Niels Kuster, for giving me the chance to take part in this venture. It's rare to meet someone with such elevated levels of vision, intelligence, commitment, and demand. His ability to multitask and to stay focused at the same time is outstanding.

My studies would not have been successful without the excellent academic environment I found myself in. I would like to express my gratitude to Prof. Klaas Prüssmann and his staff at the Biomedical Institute for welcoming me into their research group and for supervising my work. And I'd like to thank Prof. Theodoros Samaras, whose scientific backup was fundamental, and his enthusiastic approach to work has pushed me forward.

Further, I'd like to thank all friends and co-workers at "Zeugi", the exceptional crew of IT'IS, SPEAG, and ZMT. They incredibly enriched my daily life and supported me in many ways. I received a lot of outstanding inspiration from Sven, who has been sitting across from my desk for all these years, from scientific background knowledge to

good music. I enjoyed fruitful discussions with all other IT'IS project leaders: Marie-Christine, Andreas, Myles, Esra, Michael, Eugenia, Mark, Earl, and Ferenc.

For the human provocation studies and sleep research, I very much enjoyed the collaboration with Prof. Peter Achermann's group and the joint work with Maria Christopoulou. My deepest gratitude goes to Peter, Sabine, Sarah, Aleksandra, and Marc. I enjoyed the hours spent in your sleep-cave. Also, I'm grateful for the excellent joint venture with Reto Huber and Caroline Lustenberger. The largest part of these studies were conducted within the NRP57 framework, where I'd like to thank Alexander Borbély, Sonja Nevogetic, Sabine Regel, and Mirjana Moser.

The MRI related research would not have been possible without the support of Andreas, Esra, Earl, and Max; the incredible staff of IBT: Klaas, David, Roger; and all partners from the MRI+ framework: Gerard van Rhoon, Georg Frese, Gerhard Brinker, Johan van den Brink, and Wolfgang Kainz.

I had many extremely friendly encounters through the worldwide distribution of my exposure systems (sXc). Meike Mevissen and Emina Besic in Switzerland and many others from my more than 30 customers all over Europe, the U.S., China, Japan, and Israel.

The "Zeugi" family has tremendously grown during my time here. The number of people has doubled, giving a nice mix of newcomers and "old fighters". Thanks to my most faithful allies through these years, (more or less in order of appearance) Sven, Marie-Christine, Bruno, Michael, Myles, Maria, Eugene, Peter S., Peter F., Mar, Iris, Adamos, Juliette, Anastasija, Davnah, and many more.

It was brilliant to have an administration that "just works"! Jacqueline, Yvonne, Theresa, Sibyl, and Rebekka covered any administrative question and my need for shipping logistics. Software came from above, the incredible SEMCAD team, Nik, Stefan B., Pedro, Mar, and many more; hardware came from below, Bruno, Peter, Manuel, Sasha, Mirko, and their team. And my English writing got so much better, thanks to Jane and Pat!

Finally, I'd like to thank all financial contributors, the NFP57 National Research Program, Forschungsstiftung Mobilkommunikation, the CTI for supporting the MRI+ project, the European framework projects SEAWIND and ARIMMORA, as well as to all MRI Manu-

facturers that contributed to my studies: Siemens, Philips, GE, and Toshiba.

My deepest thankfulness belongs to my parents, Lea and Herbert, for their unshakable support. And from all stories I've heard from my Dad, earning a PhD was a similar process 40 year ago.

Chapter 1

Introduction

1.1 Exposure To Electromagnetic Fields

We are subjected to continuous exposure of a broad range of electromagnetic fields (EMF), every day. The sun may be the most prominent source, together with other natural sources, like the earth's magnetic field. A detailed overview of all types of EMF can be found in Section 1.2.

Within recent decades, exposures to EMF in the MHz region (VHF – UHF, 30 – 3000 MHz) have increased continuously, due to the vast number of novel wireless applications. The best known examples in everyday life are radio and television broadcasting services, mobile phone communication services, and wireless LAN computer networks. In a medical framework, typical sources of EMF are magnetic resonance imaging (MRI), hyperthermia cancer treatments, and diathermy in muscle relaxation.

The exposure levels for all EMFs must be limited to prevent adverse health effects on our bodies. A number of national and international organizations have issued guidelines for limiting exposures for the general public and occupational staff (e.g. ICNIRP [1] and IEEE C95.1 [2]). The process can be vaguely compared to, for example, limiting exposure to bacteria in the food industry or managing the toxicity of tap water.

For medical applications, risk-benefit considerations may lead to relaxed (or non-existent) limits when supervised by a medical doctor. MRI manufacturers generally comply with the product standard IEC 60601-2-3 [3] that has the aim to internationally establish basic safety requirements for MRI equipment to provide protection for patients, and which has significantly relaxed exposure limits compared to the general public (factor > 30 in SAR). The rationale for this relaxation lies primarily in the risk-benefit considerations for the patient. The potentially high diagnostic benefit justifies higher short-term exposures, compared to the omnipresent EMFs from end-user lifestyle gadgets.

The assessment of actual exposure levels and patterns is generally referred to as "dosimetry", the accurate estimation of doses, especially in radiation. With respect to my studies, the dosimetric assessment is a matter of characterizing the local and global energy deposition in the human body, as well as estimating the subsequent temperature elevations.

1.2 Electromagnetic Spectrum

The electromagnetic spectrum describes the different appearances of EMF. Although all of them are subject to the same principal mechanisms (i.e., the Maxwell equations [4]), there are considerable differences in the way they interact with us. An overview that distinguishes natural from human-made EMF is shown in Figure 1.1. The main and undisputed EMF effects on living matter can be categorized according to frequency: < 1 MHz: induced currents cause nerve stimulations; 1 MHz – 1 THz: induced currents cause tissue heating; 1 THz – 1 PHz: photochemical effects; and > 1PHz: chemical ionization that can lead to, e.g., DNA damage. There is, however, some overlapping between these categories. RF ablation, e.g., is strongly heating the tissue at ≈ 400 kHz without causing nerve stimulation.

While the focus for MR exposures is on limiting tissue heating, there is some concern regarding non-thermal effects of EMF of power lines and wireless communication. As discussed in Part II of this thesis, there is indication for currently unknown non-thermal effect mechanisms for pulsed radiofrequency (RF) EMF fields.

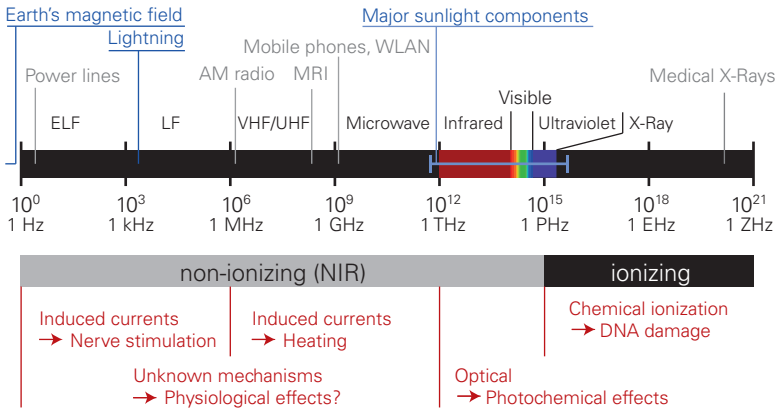

Figure 1.1: The electromagnetic spectrum with selected natural and artificial sources, and physiological effects.

1.3 Outline of the Thesis

This thesis is divided into two major parts: Part I: exposure assessments in MRI environments, where thermal effects are the primary concern, and Part II: human EMF provocation studies, including the development of adequate equipment for research on non-thermal effects.

Background and motivation are given separately for Parts I & II, due to the intrinsically different objectives. A general introduction and the epilogue tie the two parts together.

- Chapter 1: Introduction to exposure electromagnetic fields (EMF), their applications and interaction with the human body, and an outline of this thesis.

Exposure assessments in MR environments (Part I):

- Chapter 2: Motivation, objectives, and background in MR safety, including an introduction to MR physics, utilized

EMF entities, typical exposure patterns, simulation techniques, human thermoregulation, and current safety standards.

- Chapter 3: Incident field assessments for classification of selected MRI scanners in terms of RF incident fields. Appropriate measurement equipment, phantoms, and procedures are presented, as well as the results of the field distributions and peak magnitudes.
- Chapter 4: Local exposure enhancements for a broad range of anatomical human models in various imaging positions within an 1.5 T MRI scanner.
- Chapter 5: Correlation of exposure levels with various large-scale anatomical properties of several human models and imaging positions.
- Chapter 6: Thermal dose and tissue damage evaluations for different MRI scan durations, including detailed discussion of human thermoregulation and a human skin temperature validation measurement.
- Chapter 7: Outlook and challenges for future developments in MRI safety standards.

Exposure assessments for human EMF provocation studies (Part II):

- Chapter 8: Background and summary of human RF provocation studies.
- Chapter 9: Description of a novel flexible human EMF exposure system for innovative research on bioeffects.
- Chapter 10: Evaluation of the effect of EEG electrodes on the exposure pattern.
- Chapter 11: Human sleep study: Effect of EMF on sleep-dependent performance improvement.
- Chapter 12: Outlook and challenges in EMF sleep research

Epilogue (Part III):

- Chapter 13: Conclusions and outlook in human EMF exposure.

Part I

Radiofrequency Exposure and Safety Issues in Magnetic Resonance Imaging

Chapter 2

Background in MRI Safety

2.1 Motivation and Objectives

In medical technology within a clinical environment, multiple groups — patients, hospital, medical doctors and staff, manufacturers, and regulatory bodies — have each their own special interests and demands. One common interest is the safety of the medical application. My studies aim to push further the development of safety guidelines and RF exposure limitation regimes for emerging MRI technologies.

Objectives are, therefore:

- assessing the electromagnetic RF exposure within the MRI scanner
- isolating most important factors in energy absorption
- accurate modeling of thermal simulations including human thermoregulation
- assessing thermal dose and putting it into context with damage threshold limits

2.2 Magnet Resonance Imaging (MRI)

The nuclear magnetic resonance (NMR) phenomenon was discovered in 1946 by Felix Bloch and Edward M. Purcell [5]. A set of atomic nuclei have nuclear spin, which is influenced by the molecular structure. Thus, specific material properties can be deduced from the nuclear spins. Their spatial allocation allows the imaging variant of magnet resonance imaging (MRI). Since 1972, MRI has gained broad attention as a fascinating non-invasive approach for imaging anatomical structures, spectral determination of biological substances, and elucidation of physiological processes.

In a static magnetic field $B0$, the nuclear spins have energy E_m; when normalized to $E_m = 0$ at $B0 = 0$,

$$E_m = -\mu_z B0 = -m\gamma\hbar\, B0 \tag{2.1}$$

with μ_z being the z-component of the magnetic moment, m the magnetic quantum number, γ the gyromagnetic ratio, and $\hbar$ the reduced Planck constant.

By adding the energy ΔE between two quantum levels, the magnetic moments can be flipped (spin nutation), while the energy must come from an alternating field to satisfy the resonance condition for the frequency ω_o.

$$\Delta E = \hbar\omega_0 \tag{2.2}$$

By inserting Eqn. 2.1 into Eqn. 2.2, with $\Delta E = E_m$ and $m = -1$, the Larmor frequency ω_0 can be derived

$$2\pi f_0 = \omega_0 = \gamma B0 \tag{2.3}$$

which results in the typical value of $f_0 = 64$ MHz at $B0 = 1.5\,\mathrm{T}$ for the hydrogen nucleus, which has a gyromagnetic ratio of $\gamma = 2\pi\cdot$ 42.6 MHz/T.

Thus, when applying an alternating magnetic field with the Larmor (resonance) frequency, energy is absorbed by the nuclear spins

and reradiated during the relaxation. This forms the basic principle of MR imaging, which thus needs three electromagnetic entities for the desired operation:

- B0: Static magnetic field: for alignment of the spins. –
  Clinically established scanners have field strengths of 1.5 T or 3 T, with development towards 7 T, 9.4 T and beyond.

- G: Gradient fields: for applying spatially and temporally different effective magnetic fields. –
  Switching magnetic fields with frequency components up to ca. 100 kHz.

- B1: Radiofrequency (RF) field: for the spin nutation at the Larmor resonance frequency. –
  Circularly polarized RF fields with frequencies of, e.g., 64 or 128 MHz, depending on the magnetic flux density.

Static fields can induce vertigo, nausea, and a metallic taste in the mouth [3], but are surprisingly well tolerated by living matter. High switching rates of the gradient fields induce peripheral nerve stimulation, which must be limited [3]. This thesis focuses on the RF exposures from the B1 field, which may lead to considerable thermal load, as derived in Chapter 6.

2.3 The B1 field in MRI

The B1 RF field is responsible for the nutation of the nuclear spins at their resonance frequency. It should be, thus, circularly polarized, normal to the static magnetic field, and be largely homogeneous around the field of view (FOV). Traditionally, this excitation is provided by a birdcage coil (Figure 2.1) or TEM volume resonator. There are also alternative approaches, such as the waveguide modes of traveling waves [6].

As only the rotational component of B1 contributes to the spin nutation, the B1 (total field) can be decomposed into two transverse circularly polarized components $B1^+$, $B1^-$ and the z-component $B1_z$ as in Eqn. 2.4, where $B1$ is the total magnetic field, a_x, a_y, and

a_z are the coordinate system unity vectors (see Figure 2.1 for their orientations).

$$\begin{aligned} B1^+ &= \frac{1}{2}(B1(r) \cdot a_x + jB1(r) \cdot a_y) \\ B1^- &= \frac{1}{2}(B1(r) \cdot a_x - jB1(r) \cdot a_y)^* \\ B1_z &= B1(r) \cdot a_z \end{aligned} \tag{2.4}$$

$B1^+$, the right-hand circularly polarized component (rotating clockwise) with respect to $B0$, is solely responsible for the nutation of spins from the Z-direction towards the X-Y-plane. The longer the $B1^+$ RF pulse is applied, the larger the so-called 'flip angle' of spin nutation. The $B1^-$ and $B1_z$ fields are parasitic, i.e., they increase the energy absorption in the patient but do not contribute to imaging. For example, application of a linearly polarized B1 field results in $B1^+$ and $B1^-$ of equal magnitude, which is 3 dB, a factor of 2 in power, less effective, i.e., resulting in a factor of 2 lower signal to noise ratio (SNR) for a given input power. In efficient coil designs, the $B1^+$ significantly exceeds $B1^-$ and $B1_z$, at least for the FOV (Figure 2.1).

Please note that, as defined above, $B1^+$, $B1^-$ are complex scalar fields. The magnitude of $B1^+$ is most important for imaging, as it defines the flip angle. For depicting the $B1$-field, the scalar field $B1_{rms}$ is used.

2.4 RF Exposure in MR

In most cases, the limiting factor for applied B1 field levels is the energy absorption of the body, as explained below in Chapter 2.5. The major pathway of energy absorption is via induced RF eddy-currents by the time-varying B1 field. A typical absorption pattern can be seen in Chapter 5, Figure 5.2. These currents typically get higher with radial distance from the body center. At low field strengths, B1 behaves quasi-statically, with small phase delays throughout the body (around 45° at 1.5 T, 64 MHz). At 3 T and above, the shorter wavelength (roughly 30 cm at 128 MHz inside average human tissues) causes significant phase delays at the center of the body ($> 90°$). The

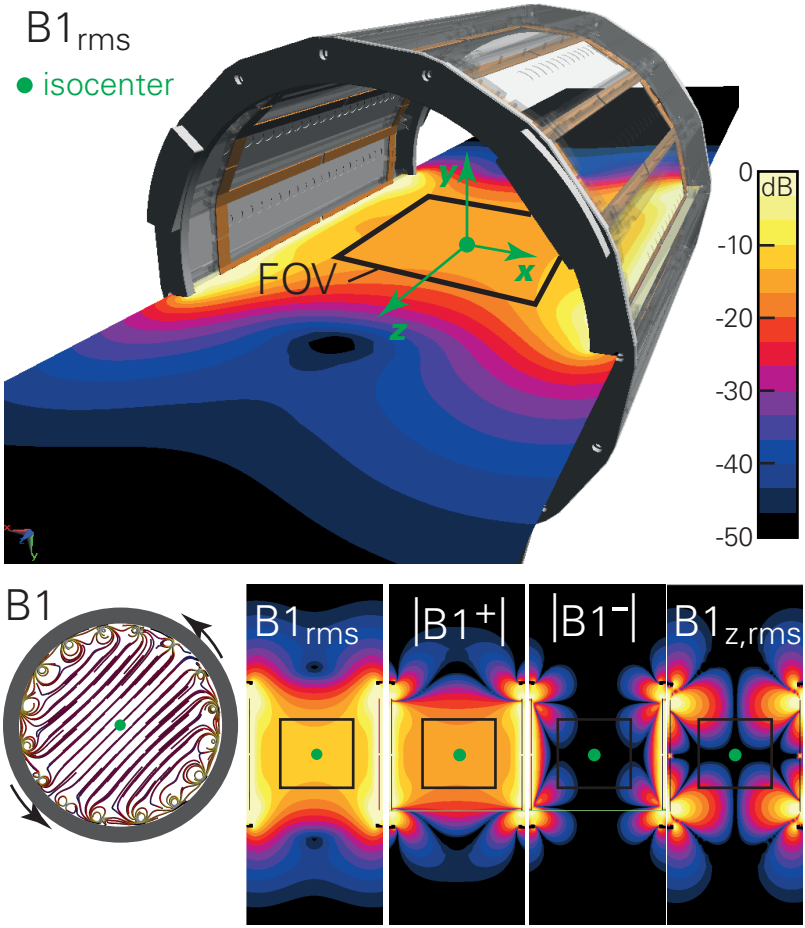

Figure 2.1: Typical birdcage resonator with B1 field and its homogeneity at the center (FOV). The B1 field can be decomposed into $B1^+$, $B1^-$ and $B1_z$. $B1^+$ is responsible for the spin nutation and should thus be the component with the highest magnitude and uniformity.

subsequent induction of eddy-currents renders a far more complex absorption distribution in the human body.

To a lesser extent, local energy absorption is also influenced by stray E-fields close to the birdcage structure. While the induced eddy-currents have similar patterns for most MRI scanners, the absorption of the stray E-fields are highly birdcage-design specific and depend on the proximity of the patient to the birdcage.

The pivotal parameter for quantizing the deposited energy and for safety guidelines is the spatial specific absorption rate (SAR), which is a metric for power absorption per mass entity with the unit W/kg. Multiple averaging schemes are defined to accurately characterize different exposure scenarios. The whole body averaged SAR (wbSAR) equals the total power administered to the patient divided by the patient mass. It serves as a surrogate for systemic thermal load — triggering whole body thermoregulation — but also as a warrant for localized exposure in body coils, which is not limited separately, see Chapter 2.5. The normal basal metabolic rate in humans is ca. 1.5 W/kg but can easily reach 6 W/kg at high activity levels. MRI exposures typically don't exceed levels of about to 3.5 W/kg wbSAR and should, thus, be tolerated under normal circumstances, in terms of overall heat dissipation capabilities.

Head and extremity imaging is better characterized by the head averaged SAR (headSAR) and partial body SAR (pbSAR). Both values estimate the averaged SAR of only the actually exposed part of the body.

Finally, for the quantification of localized exposures, spatial SAR is averaged over any 10 g of continuous tissues (sSAR10g), and the highest value found (i.e., the "hotspot") represents the peak spatial SAR (psSAR10g). This metric was originally intended as a surrogate for local thermal load, but it also eliminates possible small-scale and stair-casing errors from electromagnetic simulations. However, due to the large tissue and perfusion inhomogeneity of the human body, there is very limited correlation between psSAR and thermal load, especially with local thermoregulation. The exact averaging techniques are defined in the IEEE standard [7]. A visualization of the different distributions is depicted in Figure 2.2.

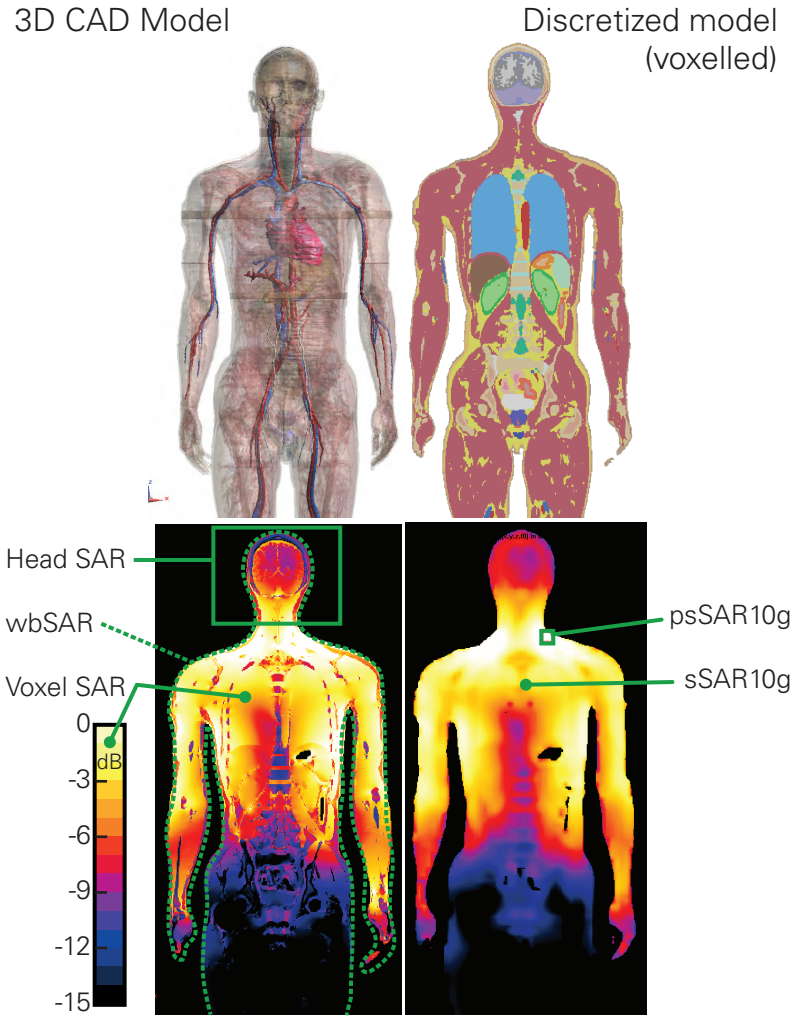

Figure 2.2: Anatomical model Duke as a 3D model, as well as in discretized slice view. The different SAR averaging schemes are illustrated on an exposure pattern originating from an 1.5 T birdcage in the heart imaging position (slice field view).

2.5 Limiting RF Exposure, IEC Standard

To prevent excessive heating, the maximum RF exposure must be managed. The discussion about safe MRI exposure levels began directly invention of the technique in the 1970s [8]. In the late 1980s, the limitations were relaxed significantly when FDA reclassified MRI scanners from class III to class II devices [9], driven by studies such as [10]. The governing temperature limits were set to 38°C in the head, 39°C in the trunk, and 40°C in the extremities. Via the IEC60601-2-33 product standard [3], energy absorption limits were derived from the thermal limits. This limitation regime has remained largely unchanged until today.

A comparison of two important current safety guidelines is given in Table 2.1. Mobile phones, e.g., generally have to comply with the ICNIRP [1] limit for the general public, since most countries have adopted their limits directly from ICNIRP. In medical applications, risk-benefit considerations often lead to less conservative limits. MRI manufacturers generally comply with the IEC 60601-2-33 [3]. There are three Operating Modes (OM) defined, reflecting the different risk-benefit considerations: (A) Normal , (B) First Level Controlled, and (C) Second Level Controlled. For (B), medical supervision is needed, while (C) requires the explicit authorization of the local investigational review board.

	ICNIRP [1] general public	IEC [3] First Level OM	Typical MR Exposure
wbSAR	0.08 W/kg	4 W/kg	< 3.7 W/kg
headSAR	(no limit)	3.2 W/kg	< 2.4 W/kg
psSAR10g	2 W/kg	(no limit)[1]	< 80[2] W/kg

Table 2.1: Overview of current safety guidelines compared to typical and MR exposures

[1] no limit specified for body coils, 20–40 W/kg for local transmit arrays.
[2] up to > 150 W/kg can be reached in body coils.

Potential non-thermal effects are not considered for the RF exposures, as the potential risk is considered small compared to the diagnostic benefits. For example, the high RF-pulsing in MR may be sufficient for the thermoelastic effect of microwave hearing [11], but the relative weighted sound pressure level from the gradient coils is typically in the range of 110 dB(A) [12], exceeding any microwave hearing levels by far.

Whole-body average SAR values were introduced to limit the systemic thermal stress. When putting more energy into the body than it can dissipate by thermoregulation, i.e., perspiration and respiration, this will eventually and ultimately discharge into systemic thermal breakdown with resulting elevation of body core temperature. Values above 39°C are considered problematic, therefore, scanning of patients with elevated core temperatures, i.e., fever, is limited and prohibited above 39.5°C [3] .

The wbSAR of a patient can be assessed by measuring the power delivered to the coil, minus the reflected power and losses (resulting in the total absorbed power in the patient), and dividing it by the patient mass. As this wbSAR limitation in body coils has been considered safe for decades, no limitations for localized SAR have been introduced [3]. Chapter 4 demonstrates that psSAR10g values of up to 80 W/kg can be found, even when in full compliance with the First Level Controlled OM, and up to > 200 W/kg when forming RF loops as shown later in Figure 4.6, which exceeds the ICNIRP limits for the general public by factors of 40 and 100, respectively.

2.6 Modeling of the Incident B1 Field

In my studies, we mainly used birdcage resonators for generating the B1 field. Birdcages have excellent homogeneity at the center of their circular structures, as well as high efficiency due to their resonant design, thus allowing cost-effective implementation with small amplifiers. They can be divided into high-pass, low-pass and band-pass designs. While in reality they are usually fed by two RF ports (IQ feeding), simulations can be performed with current-sources in the legs, which enforces the desired birdcage mode directly. An overview is given in Figure 2.3. Details about design and tuning of birdcage

resonators can be found, e.g., in [13].

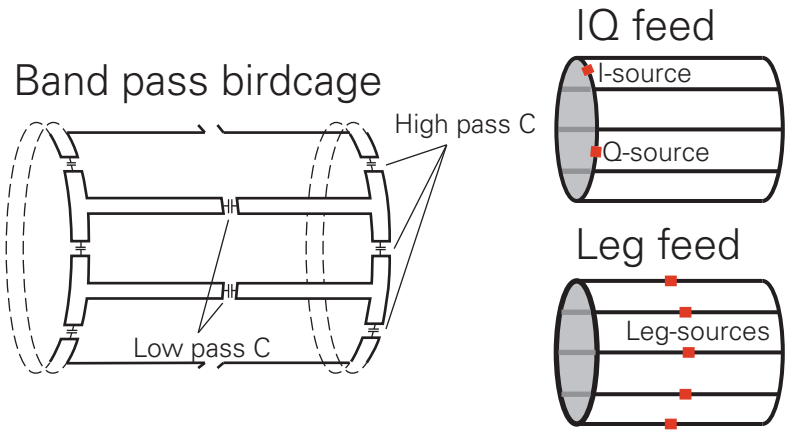

Figure 2.3: Schematic of a band-pass birdcage and visualization of different feeding structures: IQ-feed, typically with $\pi/2$ phase shift for quadrature excitation; leg-feed, which can directly enforce the desired birdcage mode.

The 1.5 T and below systems are usually operated in the circular polarized (CP) mode, also called quadrature feed. The I and Q feeds have identical amplitudes and a fixed phase shift of $\pi/2$. Due to the large wavelength at 64 MHz, the body has a small influence, and the field is mostly circularly polarized inside asymmetric biological tissues. At 3 T and above, the wavelength gets smaller — ca. 30 cm at 128 MHz inside average human tissues — and, thus, distorts the homogeneity due to the lossy tissues and axial asymmetry of the human body. To compensate for this effect, manufacturers use RF-shimming (see Chapter 2.7). Figure 2.4 illustrates the B1 field inside the empty and the patient-loaded birdcage. While an almost ideal CP field can be established in the empty birdcage ($B1^+$ is widely equal to B1, $B1^-$ is neglectable around the FOV), the presence of the lossy and asymmetric tissues decreases the circularity of B1 inside the body, which reduces $B1^+$ in certain regions.

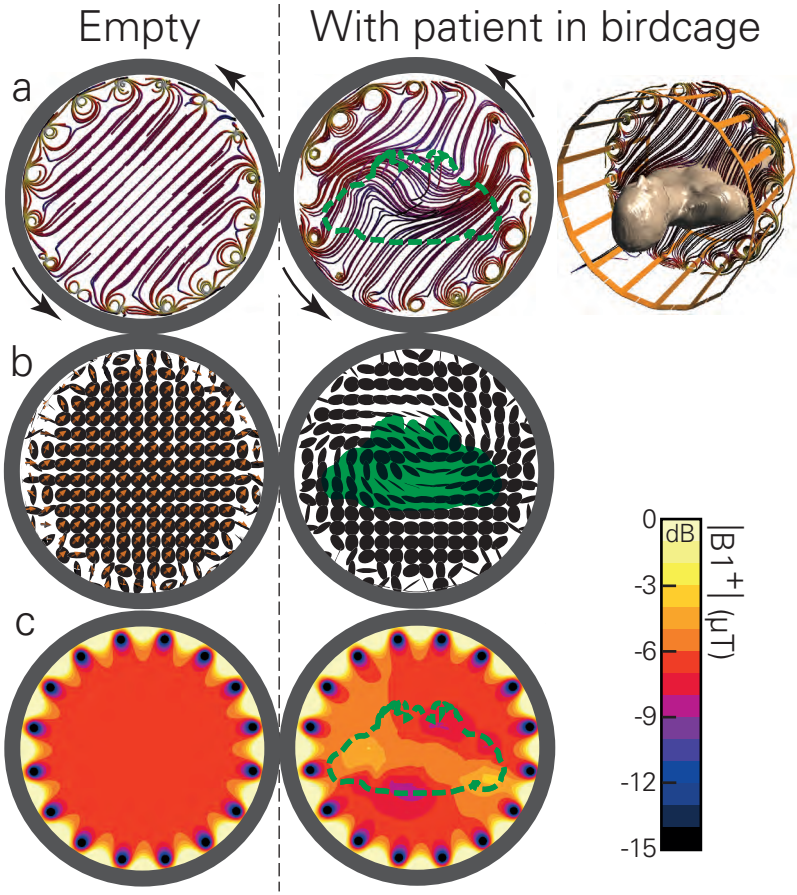

Figure 2.4: (a) Streamline and (b) vector field views (polarization ellipses in black) of the B1-field inside the birdcage resonator, and (c) $B1^+$ distribution with and without the presence of a patient. The presence of lossy tissues causes a phase delay of the B1-field via induced eddy currents.

On the simulation side, there are possibilities other than tuning on the IQ ports. A leg-feed birdcage enforces the circular mode, or a Huygens box approach applies the incident field by suppressing backscattering and the mismatch effects of the body. The latter has usually been applied within this thesis, as it applies identical incident fields to all models (children, adults, obese, etc.) and also dramatically reduces the simulation space.

2.7 RF Shimming and Multitransmit Coils

$B1^+$ homogeneity and efficiency can be significantly improved with alternative excitation schemes other than the standard CP mode. The amplitude and phase of I and Q are adjusted for better CP in the region of interest (ROI) inside the body. Depending on the imaging position, the ROI could be the arm or torso region of a patient. Generally, the ROI is always $\leq$ FOV. While some manufacturers may do this with predefined look-up tables for different patient sizes, others may have fixed shifts or perform optimizations on-the-fly. Obviously, the implemented procedures are trade secrets. Figure 2.5 illustrates the gain of RF shimming at 3 T optioned by adjusting the excitation from CP ($I = 1\angle 0°$, $Q = 1\angle 90°$) to a ROI-optimized excitation ($I = 1\angle 0°$, $Q = 0.35\angle 150°$). While the wbSAR remains identical, the $B1^+$ level and uniformity in the ROI can be substantially improved, e.g., mean $B1^+$ from 0.75 μT up to 1.2 μT and non-uniformity from 18% down to 12% SD.

Evolving MRI generations offer more than two (I/Q) ports, with individually adjustable amplitude and phases for all, e.g., 16, feed points. This technique is referred to as "parallel transmit" (pTx) or multitransmit. Different safety considerations are necessary for this approach, since the incident field pattern can change dramatically, and local energy absorption may be enhanced by a factor of up to more than ten due to constructive interference [14].

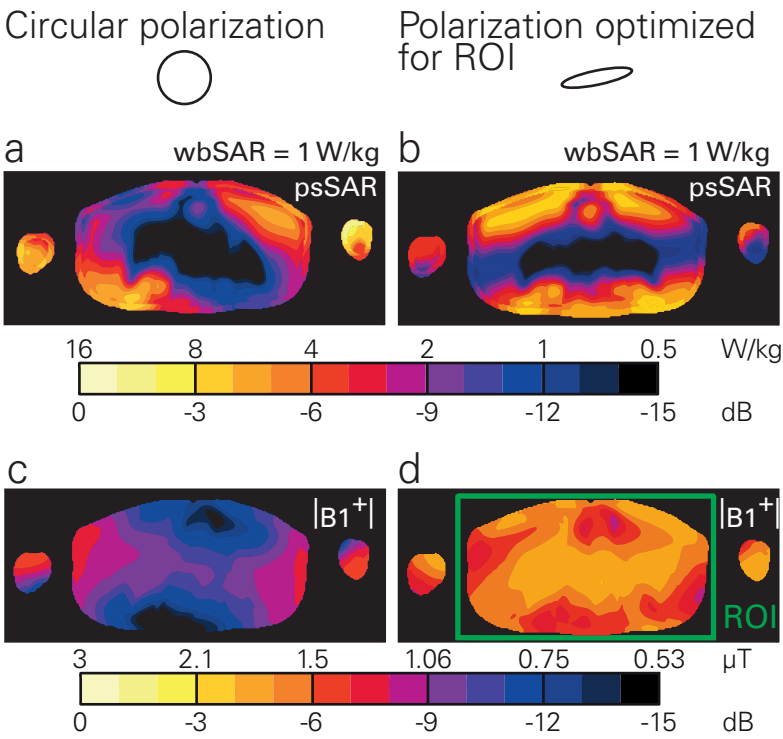

Figure 2.5: CP- and ROI-optimized excitations (applied polarization ellipses indicated) and their effects on psSAR (a,b) and $B1^+$ distribution (c,d) for a constant wbSAR = 1 W/kg. The $B1^+$ level and uniformity in the ROI (torso) can be substantially improved. The example case is for Duke inside a 3 T birdcage in pelvis imaging position.

2.8 RF Simulations with Human Anatomical Models

There are several simulation techniques in computational electromagnetics (CEM), each with their advantages and weaknesses. For the birdcage simulations, the method of moments (MOM) or the finite elements method (FEM) may be the best choice, as they can treat curved geometrical objects more accurately than other methods. However, when complex anatomical models or structures are involved (e.g., patient inside the birdcage), the simulation space can easily reach dimensions of 100 million voxels (three-dimensional pixels) or more, which is well handled by the finite-difference time-domain (FDTD) technique. Calculations can be parallelized on graphic processors (GPU), which shortens simulation time by factor > 100. However, as computers with large amounts of RAM become more and more available, anatomical models may also be simulated with FEM, which may be better suited for resonant structures.

In the studies included within this thesis, all simulations were performed on SEMCAD X (versions 13.4–14.8), an FDTD simulation platform jointly developed by SPEAG (Zurich, Switzerland) and the IT'IS Foundation.

To replicate realistic simulation scenarios, accurate 3-dimensional human anatomical models are needed, with correctly assigned tissues. Models with increasing resolution and quality have been developed in recent decades: the "visible human" developed in 1994 by the U.S. National Library of Medicine; the japanese female and male models Hanako and Taro developed at the National Institute for Communications Technology (NICT); and the Virtual Population [15], consisting of more than 10 models (children, adults, elderly, obese, pregnant), jointly developed by the FDA and the IT'IS Foundation. The assignment of dielectric properties to up to 90 different tissues and organs is according to literature values, as described in a comprehensive review [16] based on [17].

Chapters 4 and 5 are typical applications of EM simulation scenarios. The B1 field with and without an anatomical model is visualized in Figure 2.4.

2.9 Human Thermoregulation

The primary focus within these studies on thermoregulation is the down-regulation of temperature as a response to excessive heating in the MRI environment. We do not investigate thermoregulation due to low-temperature stimuli.

There are two major thermoregulation regimes relevant in MRI exposures.

- whole-body heating / systemic thermoregulation
- localized heating / local thermoregulation

The two regimes are analogous to the difference between suffering from heat-stroke (where no burn is visible) and burning a hand on a hot plate (where no heat-shock symptoms are expected). The first is easier to diagnose, as it can be estimated from elevated core temperature, increased heart rate, or extensive sweating and discomfort. The latter is more challenging and needs to be discussed thoroughly. Obviously, depending on the extent of the localized heating, the two regulation regimes may interact.

2.9.1 Whole-Body Thermoregulation

Experience from hyperthermia shows that very high wbSAR values (typically 6 – 10 W/kg) can be tolerated without systemic thermal breakdown, i.e., without core-temperature elevation above 38 – 39°C [18]. While there is an ongoing debate about the exact systemic thermoregulation mechanisms, the actual heat-loss pathways are clear. The most important factor may be behavioral thermoregulation, as we actually seek shade when we're hot in response to a conscious sensation of heat or pain. In MRI examinations, this would result in patient feedback to the operator. On the physiological side, there are the following mechanisms: (a) increased skin vasodilatation leads to higher cooling of the blood, (b) skin temperature can be lowered by sweating, (c) elevated breathing rate enhances heat loss in the pharynx, trachea, and lungs, and (d) increased heart rate for more rapid recuperation. Dehydration may impair whole-body thermoregulation. Monitoring and limiting body core temperature efficiently prevents

systemic breakdown or adverse effects from whole-body heating. This simple measurement can be performed with a single oral or rectal temperature probe.

2.9.2 Local Thermoregulation

Human response to local heating is far more challenging to assess. Also here, behavioral thermoregulation may be the most important response, e.g., the dedicated spinal reflexes to withdraw the hand from the hot plate. However, as the hotspots from MRI exposure may occur in tissues without thermal sensation, these mechanisms may be considerably constrained. Muscle, for example, does not cause a conscious thermal sensation between 8 and 48°C, and pain sensation is significant only at or above 48°C, which was determined by application of a hot isotonic saline intramuscular injection [19]. The main physiological tissue response to local heating is increased blood perfusion [20], which enhances cooling in the affected region. Response times are on the order of several minutes, and local blood flow can be upregulated by more than an order of magnitude [21]. Other mechanisms are far less relevant for extensive local heating (> 20 W/kg local SAR). Increased sweating and airflow leads to lower surface temperatures, but does not significantly affect structures with more than about 10 mm distance to the body surface, as blood temperature is maintained via the whole-body thermoregulation.

This leaves the local blood perfusion increase as the primary mechanism for local thermoregulation. The actual effect-magnitude, however, is subject to many complex interactions and dependencies: (a) there are potentially large inter-subject variations; (b) the physical extent of the heat administration influences the amount of blood available according to the blood-compartment model; (c) blood is subsequently redistributed [22], and (d) thermal memories introduce a dependency on the temperature history of the tissue, which may also lead to an enhanced thermal resilience.

As discussed in Chapter 6, we mainly followed the work of Laakso et al. [21] with up to a factor of 32 increase in local bloodflow in skin and a factor of 15 in other tissues.

2.10 Thermal Simulations

The electromagnetic simulations and their RF energy absorption distribution (SAR) can be used as input for thermal simulations. There are two major approaches — absolute temperature and temperature increase simulations — with two major solving strategies: transient time-domain and steady-state solvers.

The Pennes bioheat equation (PBE, Eqn. 2.5) is well established:

$$\begin{aligned} \rho c \frac{\partial T}{\partial t} &= \nabla \cdot (\kappa(\vec{r}) \nabla T(\vec{r}, t)) + g(\vec{(r)}, t) \\ g(\vec{r}, t) &= \rho Q + \rho S - \rho_b c_b \rho \omega (T - T_b) \end{aligned} \tag{2.5}$$

where T is the temperature at location $\vec{r}$ and time t, c the specific heat capacity, κ the thermal conductivity, ρ the density, ω the perfusion rate, Q the metabolic heat generation rate and S the spatial specific absorption rate (SAR). The index b indicates a property of blood. The PBE performs well for the given exposure scenarios, given a relatively stable core temperature. However, it neglects certain aspects such as anisotropic heat-flux or varying blood temperatures along the vessel.

Thermal tissue properties are assigned with literature values, e.g. from [16], and contain high uncertainty and inter-subject variability. The major tissue response to temperatures significantly above 37°C (psSAR10g exposures above 20 W/kg) is increased bloodflow [20, 21]. Thermal simulation results are presented in Chapter 6.

2.11 Thermal Dose (CEM43) and Damage Thresholds

Temperature alone is a poor surrogate for thermal stress on tissues. In fact, appropriate integration of temperatures over time is much closer related to the actual thermal tissue damage observed. Intuitively, it is clear that holding your hand in 60°C water for 1 second will cause you less pain than leaving it there for several minutes. The most prominent investigation on the corresponding correlations has been conducted by Sapareto et al. [23], in which a mathematical

translation of time-temperature combinations to cumulative equivalent minutes at 43°C (CEM43) is presented. Estimation of the effective equivalent thermal stress is achieved via the integration of a temperature-weighted function over time:

$$CEM43(t) = \int_{t_0}^{t_{final}} R^{(43-T(t)} dt \tag{2.6}$$

where t_0 signifies the beginning of the heating period and t_{final} its end. $T(t)$ is the temperature of the tissue of interest at time t, and R is a constant equal to 0.5 for $T(t) > 43$°C, 0.25 for $39° < T(t) < 43$°C, and $R = 0$ for $T(t) < 39$°C.

For example, exposing skin tissue for 240 min to 43°C (CEM43 = 240 min) causes symptoms equivalent to those caused by 960 min (16 h) at 42°C, 1 min at 51°C, or 0.1 s at 60°C. Different tissues have different resiliencies to thermal load. Skin may tolerate up to CEM43 = 240 min (as in the example above), more sensitive structures (e.g., the blood-brain barrier) show significant adverse effects already at CEM43 = 2 min. From the skin example above, we can see that burns may result from touching objects hotter than 60°C, as the reaction time of withdrawing your hand is longer than the skin can tolerate at that temperature. The application of the CEM43 dose evaluation can be found in Chapter 6.

From literature values, thermal damage threshold values for various tissues can be derived and divided into minor and significant adverse changes. The endpoints for estimating damage usually are based on (1) histopathology, i.e., microscopic examination of tissue samples, (2) gross appearance, and (3) physiological function. The comprehensive reviews of Dewhirst and Yarmolenko [24, 25] give excellent overviews on the tissues' thermal resilience. Damage thresholds for severe effects can be categorized as follows (excerpt from [24]):

CEM43 = 2–20 min	blood brain barrier (BBB), brain, bone
CEM43 = 20–40 min	small intestine, mammary gland
CEM43 = 40–80 min	muscle, cornea, lens, nerve, retina
CEM43 = > 80 min	skin, fat, esophagus, prostate, rectum

In MRI exposures at 1.5 T and 3 T, the peak temperature usually

occurs within muscle, skin, fat, or bone tissues. To facilitate the evaluations, we propose having a CEM43 threshold limit of CEM43 = 15 min for these four tissues, and CEM43 = 2 min for all others. The 15 min limit was chosen, as this is the threshold for bone, which is the lowest in this group. Similar, BBB has the lowest threshold (CEM43 = 2 min) in all other tissues.

2.12 Validation Methods

Simulation results are susceptible to many biases and cumulative errors. A rigorous uncertainty budget is generated in all our studies to estimate the accuracy of our evaluations. However, a reality check in the form of *in vivo* and human validations is indispensable. Unfortunately, access to local temperatures in humans is challenging. Thus, we pursued validations on different levels of abstraction.

Phantom Validation. The simulation results can be benchmarked against dosimetric measurements in phantoms. This has been performed for both EM and thermal experiments, e.g., in [26].

***In Vivo* Validation.** Two project partners have performed validation measurements in swine. The Charié Hospital in Berlin found alarmingly high local temperatures (up to 50°C) when exposing the pigs to 4 W/kg wbSAR for 60 min, which, in essence, cooked part of the muscle tissue. A group in Minnesota [27] found comparable results. As the same 4 W/kg wbSAR level is allowed in clinical practice, pigs may have significantly lower thermoregulation abilities compared to humans, or their thermoregulation may be influenced by the anesthetics. However, it is questionable how many patients really are exposed to 4 W/kg for 60 min, as discussed in Chapter 2.13.

Human Validation. Invasive measurements in humans are challenging. The EM simulation can be partially validated via B1+ scanner measurements. As this CP component of B1 is responsible for spin nutation, the relative distribution or B1+ can be estimated with dedicated scan sequences [28]. Skin temperatures can be measured near estimated hotspots for validation of transient temperatures, as described in Chapter 6. Internal temperatures, however, remain widely unvalidated with this method. The most promising technique for future validation concepts is MRI thermometry, in which the proton

resonance frequency shift (PRFS) [29] is used to assess the internal temperature distribution non–invasively. While, so far, the measurement uncertainty on the order of 1°C in living subjects may be too high for validation purposes, future developments could allow this.

2.13 Safety Standard and History of Safe Use (HoSU)

At first sight, standard quadrature driven coils operated according to the product standard [3] are deemed safe, based on their remarkable history of safe use (HoSU), with incidents on the ppm scale [30]. Despite very high localized RF exposure, introduction of more conservative limits are not called for. However, there are indications that the allowance in the defined operating modes was very rarely fully exploited. While wbSAR values of up to 4 W/kg are allowed [3], the actual wbSAR rarely exceeds 2 – 3 W/kg due to the (1) manufacturer's safety margin and (2) frequent interruption between the scan sequences. The allowed maximum SAR-dose of 240 W·min/kg (4 W/kg for 60min) is believed to rarely ($< 0.1\%$) exceed about 150 W·min/kg. This data originates from personal communication with MR manufacturers and cannot be cited due to trade secrets. But it may lead to the conclusion that the HoSU only proves the safe use of actually applied exposure levels, rather than of the currently allowed exposure level. A revision of IEC 60601-2-33 [3] is, therefore, recommended.

The challenge for future revisions of the safety guidelines, however, will be related to emerging new technologies, e.g., multitransmit coils, that cannot rely on this HoSU and need more sophisticated safety assessments. An important step in this progress is presented within this thesis, by reproducing the HoSU. The developed accurate EM and thermal modeling methodologies can be adapted to novel exposure scenarios. An outlook is given in Chapter 7.

Chapter 3

Incident Field Measurements and Classification of MRI Field Generating Units

3.1 Objectives

Within this classification report, the B1 incident field distributions from seven of the most common MRI scanners have been assessed, allowing for a representative characterization of the RF components. The key parameters for the incident B1 fields include the volume of B1, i.e., (a) geometry of the body-coil, (b) B1 field distribution, and (c) the orientation of the polarization of scanners from a specific manufacturer.

3.2 Selected MR Systems

There are only a few full system MRI suppliers worldwide: Siemens, GE, Phillips, Toshiba, Hitachi, and a few smaller ones such as Isol.

Siemens, Philips and GE have a market share of about 80%. The distribution of the installed scanners as of 2007 was approximately as follows: <0.5 T (open): 20%; 1.5 T: 66%; 3 T: 12%; a few units of 4 T, and about twenty 7 T scanners. Fewer than 3% are in the class 0.5 – 1.0 T [31].

As this classification focuses on measurements of 1.5 T and 3 T closed-bore systems only, seven MRI scanners with cylindrical bores have been identified, measured, and integrated in this report (see Tables 3.1 and 3.2). The selection was based on (1) following publications such as [32], (2) personal communications with radiologists and company representatives, (3) relevance to the market, and (4) differences in body coil (length, diameter).

Manufacturer Scanner	Philips Achieva	Siemens Avanto	Siemens Espree	GE TwinSpeed
Type	1.5 T	1.5 T	1.5 T	1.5 T
Software	2.5.1.0	SyngoB15	SyngoB15	14.0_M5
RF system	Freewave	TIM	TIM76x32	HDx
Frequency	63.9	63.6	63.6	63.86
Peak power (kW)	25	15	22.4	16
Peak B1 (μT)	27	30	23	25
Location	USZ	Uni Basel	Uni Basel	KiSpi

Table 3.1: Selected 1.5 T MRI-scanners with nominal key parameters.

Manufacturer Scanner	Philips Achieva	Siemens Verio	GE TwinSpeed
Type	3 T	3 T	3 T
Software	2.5.1.0	SyngoB15	14.0_M5
RF system	Freewave	TIM120x32	HDx
Frequency	127.73	123.2	127.73
Peak power (kW)	25	35	35
Peak B1 (μT)	13.5	23	25
Location	Uni Basel	Uni Basel	KiSpi

Table 3.2: Selected 3 T MRI-scanners, with nominal key parameters.

3.3 Methods

3.3.1 RF Measurement Protocol

The field distribution of the B1 incident field has been assessed according to the measurement protocol in Table 3.3. Measurements of one scanner took roughly 3 hours (not including preparations), and was, therefore, usually performed at night at the different hospital sites. The term "boresight" refers to the symmetry axis through the bore in the Z-direction, with the isocenter being the symmetry point of the bore.

	Activity	**Sequences**	**Location**
1	Identify isocenter	Survey sequence	Isocenter
2	Field distribution	Test sequence	Boresight
3	Field distribution	Test sequence	Other positions
4	Body coil search	Test sequence	Trial and error
5	Time domain measurement	Test sequence	Fixed position

1. The isocenter was identified with a liquid-filled phantom that included a "marker" region without liquid. The position has been adjusted until the overview scan displayed the marker at the isocenter.
2. E-Field and H-field measurements were conducted in 50 mm steps along the boresight.
3. The probe positioner (Figure 3.1) was used to measure non-boresight positions of the measurement grid
4. We searched for the field enhancements around the end-ring and loading capacitors, to assess the birdcage geometry.
5. The time domain signal of the actual test sequence is measured to post-calibrate the RMS probes.

Table 3.3: Measurement sequence

3.3.2 Measurement Phantoms, Jigs and Grid

Figure 3.1 shows the measurement grid within the MRI machines. The ΔZ grid is based on 100 mm Z-axis increments. The crosses represent the E- and H-field probe positions. On the boresight, the spacing was reduced to 50 mm. The total number of envisioned points to be

recorded was 62. In addition, a scan of the bore surface was performed to investigate the structure of the body coil. Measurements were performed only to the front of the iso-center and out to 700 mm from the iso-center, assessing one octant of the bore. The adjustment of the grid was done on on-site. The measurement probes were supported with a custom probe positioner as shown in Figure 3.1. There is a support base with adjustable legs and two different sized rotatable probe holders designed to cover the range of required locations.

The measurement software is set up to accept as input a matrix defining the X and Y coordinates of the measurement point and then to measure and step in the Z-direction as requested by an optical trigger. The software then records the probe values in the required format for appropriate post processing. The collected data allows contours to be plotted in sufficient detail to assess the consistency of the measurements.

3.3.3 Measurement Equipment

RF measurements were performed with a standalone data acquisition system called EASY4MRI (Speag, Zurich, Switzerland), which has been optimized for operation in MRI environments. The equipment can be seen in Figure 3.2, and the specifications are listed in Table 3.4. The electromagnetic immunity of the EASY4MRI measurement system was evaluated in 1.5 T and 3 T MRI machines [32]. The results are shown in Table 3.5.

3.3.4 RF Test Sequence and Probe Calibration

The measurements of the RF fields were performed with a simple test sequence, which allowed the RMS field probes to properly compensate for the crest factor; the use of a complex clinical sequence might lead to results with high uncertainties. A sequence similar to our proposed waveform (Fig. 3.3) could be implemented on all scanners. A manufacturer representative (application engineer) was in some cases called in to program the machine for our test purpose. The actual waveforms of the test sequences can be seen in Figures 3.4 and 3.6. The probes were calibrated post-hoc at 64/128 MHz in a TEM cell in air, where the H-fields are normal to the E-fields and transversal to

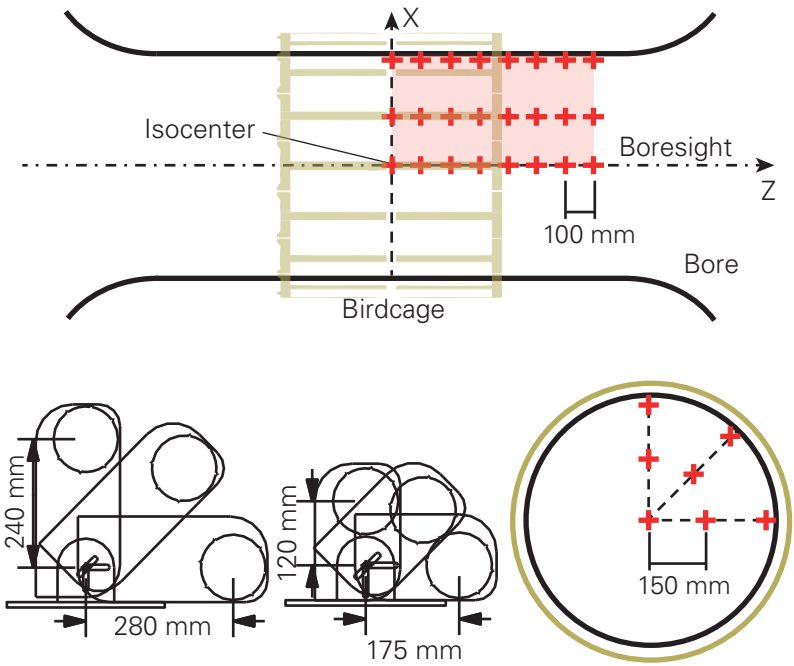

Figure 3.1: Measurement grid and probe positioners. One octant is measured, and symmetry is assumed.

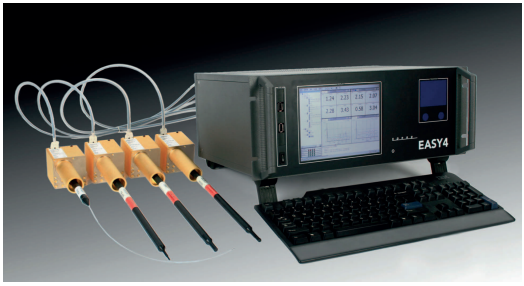

Figure 3.2: EASY4MRI system with four probes and DAE4MRI.

E-field probe:	**SPEAG ER3DV6**
Frequency range	10 – 6000 MHz
Dynamic range	1 – 1000 V/m
Spatial resolution	< 7 mm
Directivity error	< ±0.3 dB
H-field probe:	**SPEAG H3DV7**
Frequency range	40 – 3000 MHz
Dynamic range	0.01 – 10 A/m
Spatial resolution	< 4 mm
Directivity error	< ±0.2 dB
Data Acquisition Electronics	**SPEAG DAE4MRI**
Input range	−100 – 300 mV
Power	Lithium polymer battery
Output	Optical
Noise	<7 µV
Sampling rate	128 µs
Data Logger / Field Monitor	**SPEAG EASY4MRI**
DAE4MRI inputs	4× optical
DAE power output	4×
Interfaces:	ETHERNET, USB
Modes	Monitoring, data recording
Sampling rate	10 ms to hours
Loop Detector	**Omnisec, pn 7405-902**
Detector Diode	Sn 208
Size	Diameter approx. 30 mm
Oscilloscope	HS3 Handyscope

Table 3.4: Measurement equipment specifications

Type	**Data Acquisition Electronics DAEMRI**	**H-Field H3DV7**	**E-Field ER3DV6**
Acceleration	< 0.1 g/T	0.01 g/T	<0.01 g/T
Noise, laboratory conditions)	< 7 µV	<10 mA/m	<1 V/m
Noise, 1.5 T static	< 10 µV	<10 mA/m	<1.2 V/m
Noise, 3 T static	< 10 µV	<10 mA/m	<1.2 V/m
Noise, 1.5 T static + gradient	< 10 µV	<10 mA/m	<1.2 V/m
Noise, 3 T static + gradient	< 20 µV	<17 mA/m	<1.7 V/m
Noise, 1.5 T static + gradient + RF	< 40 µV	n.a.	n.a.
Noise, 3 T static + gradient + RF	< 40 µV	n.a.	n.a.

Table 3.5: EASY4MRI MRI-EMI results

the direction of propagation. The H-field can be calculated from the E-field with the aid of the wave impedance of free space.

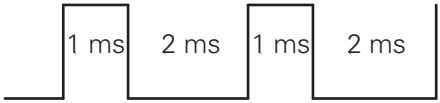

Figure 3.3: Proposed RF pulse test sequence

3.3.5 Data Evaluation

All measured data were post-processed in Matlab (MathWorks, Natick, US) and normalized to a $B1_{rms}$ value of 1 µT at the isocenter. A comparison is made to the simulation values of the RF birdcage test systems MITS 1.5 and MITS 3 (ZMT, Zurich, Switzerland). Simulations were performed with SEMCAD X (SPEAG, Zurich, Switzerland). Because of the high axial symmetry, plotting of the X-Z-plane (X,Z $>$ 0, Fig. 3.1) is considered sufficient to represent the entire field.

3.4 Results

Results are shown in Figures 3.4 – 3.7. The B1-field distribution as well as the stray E-fields have the same fundamental pattern for both, real MRI scanners and the MITS test systems. Variations originate from the length of the birdcage and the bore diameter (dimensions are indicated on the graphs). The GE Twinspeed 3 T system exhibits a different pattern especially in the B-field. The coil resonator type and number of rungs could not be estimated free of doubt. Wide-bore systems as the measured Siemens Espree and Verio have much higher stray E-fields around the birdcage end-ring.

3.5 Conclusions

While the essential field distribution is comparable, the between-scanner variations in the B1 field levels are considerably large. Especially the stray E-fields around the end-rings of the birdcages can get very strong in wide-bore systems. While for bore diameters $\leq$ 600 mm the maximally measured E-field RMS values remain below 400 V/m (normalized to 1 μT at isocenter), the accessible magnitude can get up to 1000 V/m in wide-bore systems.

The B0 static magnetic field of Siemens and GE scanners are in opposite direction compared to the Philips magnet. Therefore, the circular polarization of B1 has the opposite rotation direction for Philips, when accessing the magnet from the front.

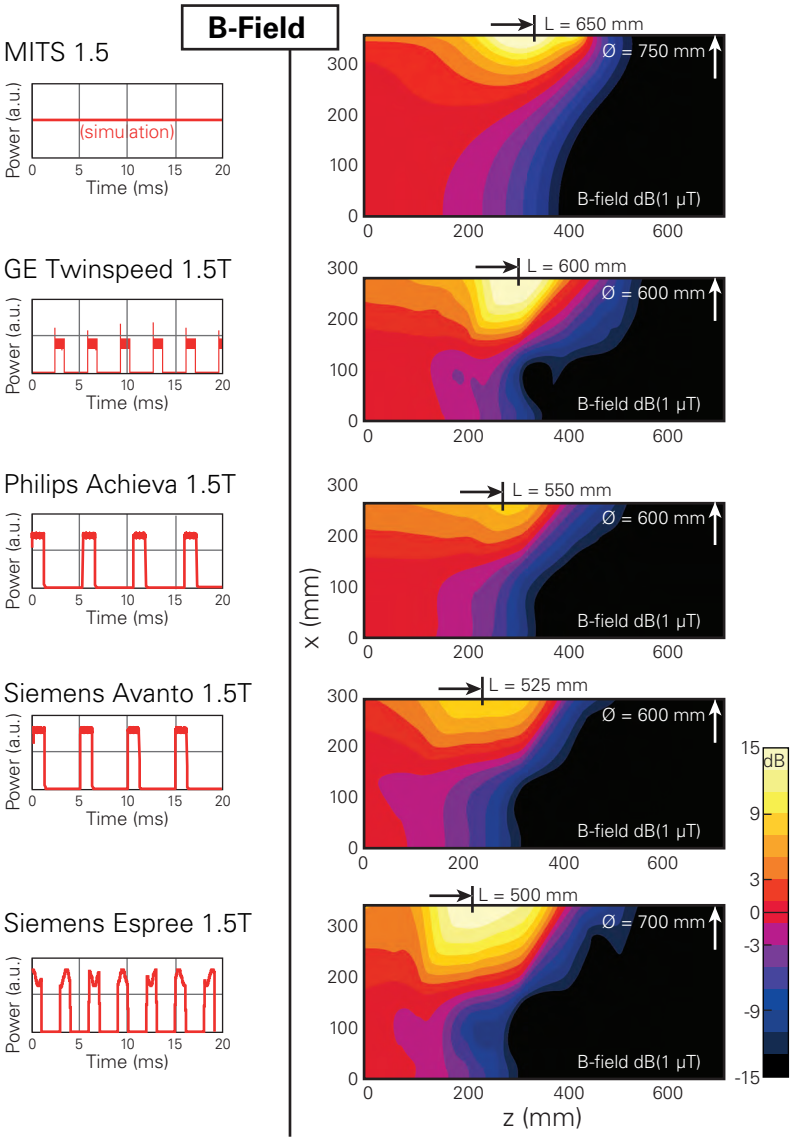

Figure 3.4: B1-field distributions of the MITS test system and the assessed 1.5 T scanners, and the applied test sequences

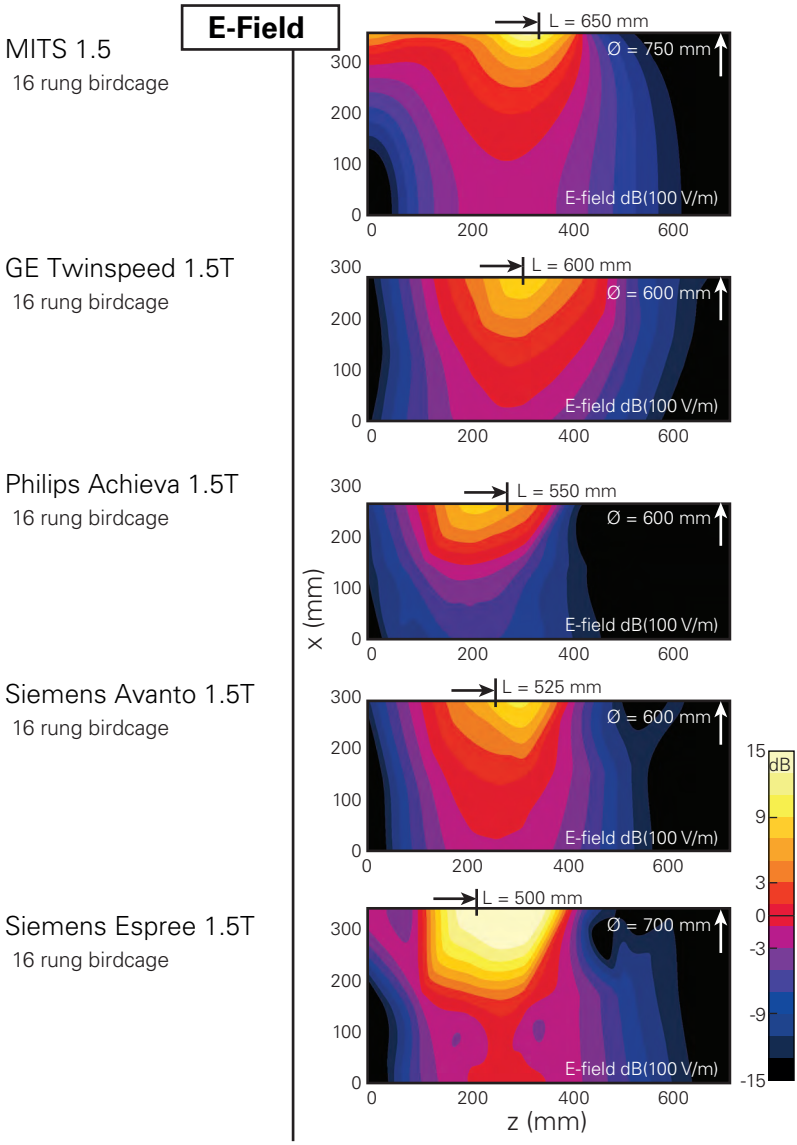

Figure 3.5: Corresponding stray E-field distributions at 1.5 T

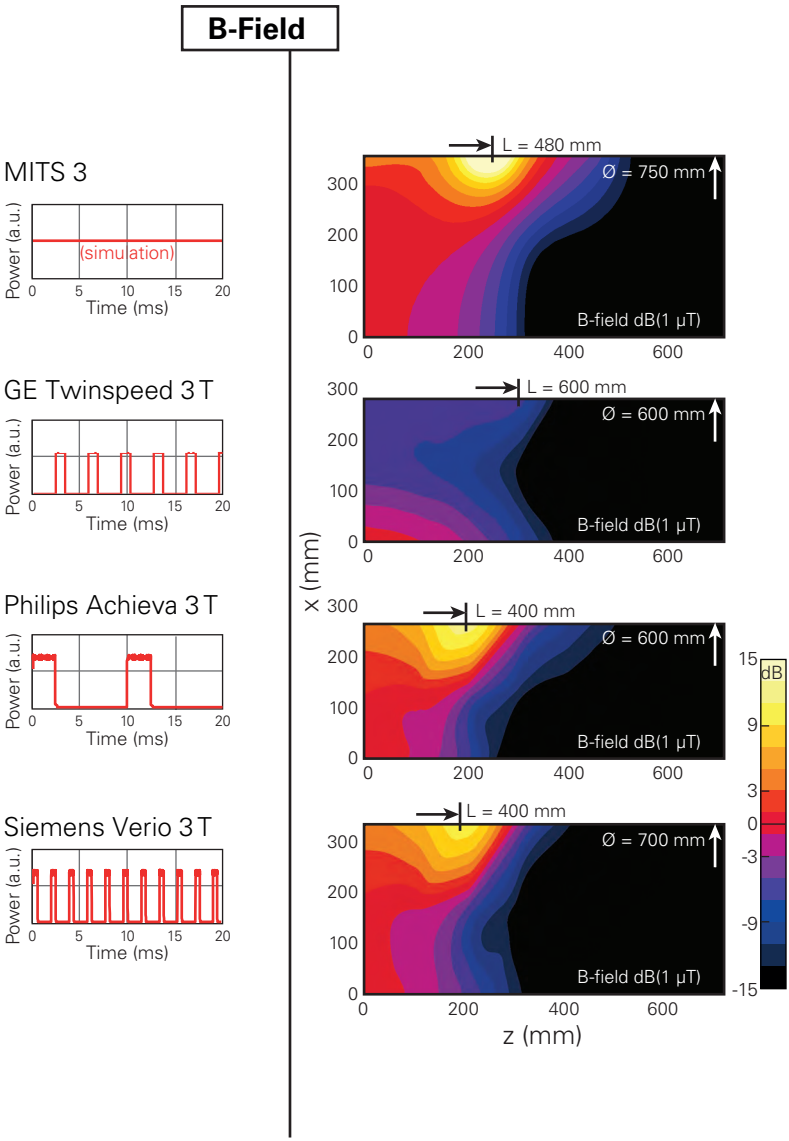

Figure 3.6: B1-field distributions of the MITS test system and the assessed 3 T scanners, and the applied test sequences

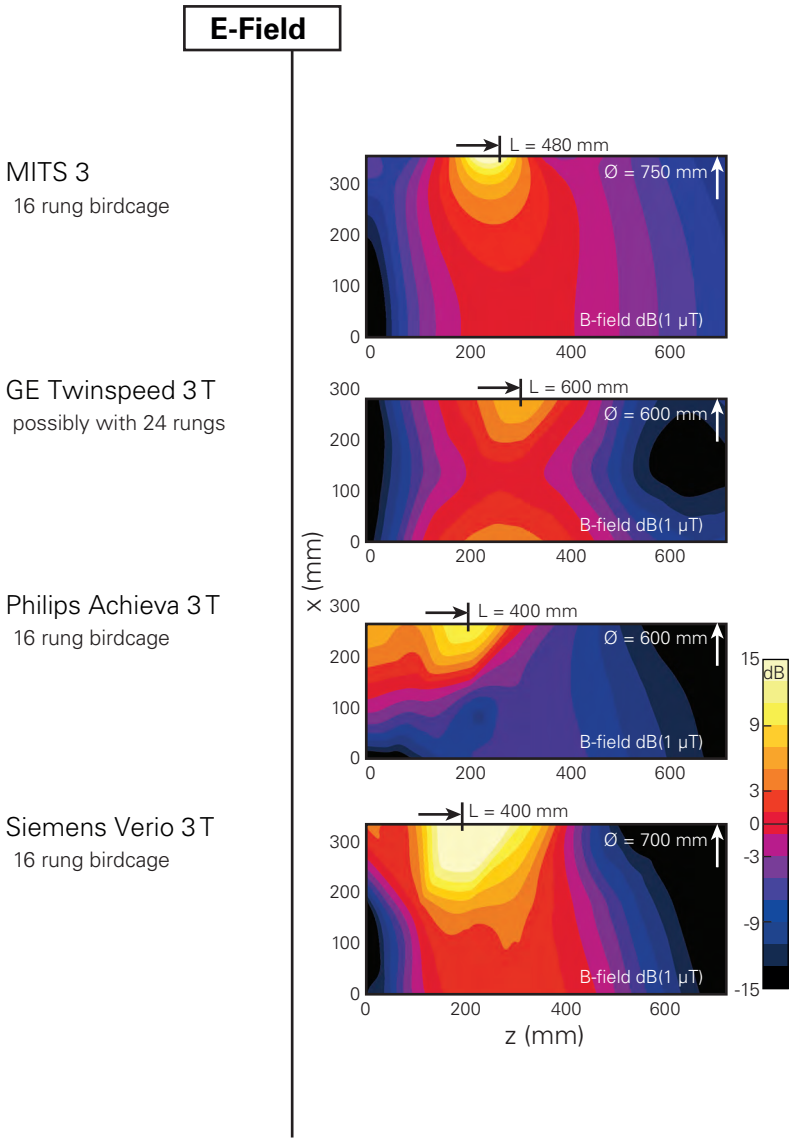

Figure 3.7: Corresponding stray E-field distributions at 3 T

Chapter 4

Local SAR Enhancements in Anatomically Correct Children and Adult Models as a Function of Position within 1.5 T MR body coil

4.1 Abstract

[1]Usage of magnetic resonance imaging (MRI) is continuously increasing due to its excellent soft-tissue contrast and improving diagnostic values. MRI also has the advantage that it operates without ionizing radiation. The main safety concerns are torque, acceleration by

[1]This Chapter has been published in [33].

the static field, nerve stimulation by the gradient fields, and tissue heating by the radio-frequency (RF) fields. This paper investigates if children and fetuses are at higher risks than adults when the current RF regulations are applied. We analyzed and compared local absorption hotspots, i.e., the peak spatial specific absorption rate averaged over any 10 g (psSAR10g) for five adults, three children of ages 5, 11 and 14 years, and 1 pregnant female (36 weeks' gestation) in 10 different Z-positions (head to calves). In the First Level Controlled Operating Mode (4 W/kg whole-body averaged exposure), the psSAR10g values found for adults were as large as 60 W/kg in the trunk and 104 W/kg in the extremities. The corresponding values for children were 43 and 58 W/kg, respectively, and 14 W/kg for the unborn child. Modeling of worst case anatomical RF loops can substantially increase the psSAR10g values, i.e., by factor >> 2.

The results suggest that local exposure for children and fetuses is smaller than for adults (15–75%), i.e., no special considerations for children and the unborn child are needed regarding psSAR10g due to RF. However, the local thermal load of the unborn may be significantly increased due to the high exposure average (up to 4 W/kg) of the non-perfused amniotic fluid.

4.2 Introduction

Magnetic resonance imaging (MRI) has established itself as a routine technique in medical diagnostics. The absence of ionizing radiation, the excellent soft-tissue contrast and flexibility are the major advantages of MR systems compared to computer tomography (CT). The potential patient risks due to torque and acceleration of ferromagnetic objects by the static field, nerve stimulation by the gradient fields, and local and whole-body tissue heating by induced eddy currents from the radio-frequency (RF) fields must be carefully managed, the guidelines of which are defined in [3]. With respect to RF safety, this standard defines three Operating Modes (OM): (A) Normal, (B) First Level Controlled, and (C) Second Level Controlled. For (B), risk-benefit considerations and additional medical supervision are needed, while (C) requires the explicit authorization of the local investigational review board. Within this study, the children

and adult models are exposed to the First Level Controlled OM and the pregnant woman to NORMAL OM, representing clinical relevant worst-case RF exposures. RF exposure is usually expressed in terms of the specific absorption rate (SAR), with the principal underlying mechanism of induced eddy currents by the time varying B1 field, which is typically circularly polarized and perpendicular to the Z-axis. Therefore, the highest SAR values are usually found in peripheral areas as eddy currents increase with radial distance.

The OMs are defined by limiting whole-body, partial-body and head SAR (wbSAR, pbSAR, hdSAR). The standard does not limit local hotspots or peak spatial SAR averaged over any 10 g of tissue (psSAR10g). Limits for psSAR10g have not been defined for volume coils, i.e., it is implicitly assumed that hazardous local hotspots are prevented if the large body averaged SAR limits are satisfied [34]. This study presents numerically derived SAR enhancements using 9 different anatomically correct human models in 10 different Z-positions within a generic 1.5 T MR body coil.

The psSAR10g values depend on:

- large anatomical features: height, weight, shoulder length, forming of current loops
- subjects' position: x, y, z, relative to the body coil
- subjects' posture: standard (lying on back), prone, sideways
- detailed anatomical features: dielectric contrasts, body constraints
- birdcage geometry and field pattern.

These dependencies are best addressed by numerical investigations with anatomically correct models. The largest obvious differences between children and adults are the dimensions of the large anatomical features.

4.3 Methods

4.3.1 Simulation Configuration

In order to investigate the major impact parameters of anatomy and position on local SAR enhancements, nine different anatomical models were used for numerical evaluations in ten different Z-axis positions each (Fig. 4.1). The children Billie, Louis, and Roberta, and the adults Duke, Fats, Ella, and pregnant Ella are part of the Virtual Population [35] (www.itis.ethz.com/vip). They have a resolution of less than $0.9\times0.9\times2$ mm^3 and consist of more than 69 different organs and tissues, which have been reconstructed as triangular surface meshes. The Japanese Female Hanako and Japanese Male Taro were developed at the National Institute for Communications Technology (NICT). An overview of the models can be found in Table 4.1 and Figure 4.2).

Name	Sex	Age [years]	Height [m]	Weight [kg]	BMI[1] [kg/m^2]	BSA[1] [m^2]	No. of tissues
Billie	f	11	11.47	35.4	16.5	1.20	74
Duke	m	34	1.78	76.2	24.3	1.87	73
Ella	f	26	1.63	59.1	22.2	1.64	73
Preg. Ella (36 weeks)[2]	f	26	1.59	64.7	25.8	1.69	90
Fetus	f	0	0.50	3.0	12.0	0.20	26
Fats	m	37	1.82	120.2	36.4	2.46	76

Table 4.1: Overview of the anatomical models used for simulations.

The dielectric tissue properties have been assigned according to literature values [17] that have recently been updated [16]). In terms of dielectric properties, the placenta is assumed to correspond to muscle and the amniotic fluid to cerebrospinal fluid, as suggested in [37]. Recent measurements could not be extrapolated to the 1.5 T specific larmor frequency, but seem to support this assumption [38]. All digestive lumina are filled with air, unlike in comparable studies [39] which used the properties of muscle or surrounding tissues. The difference in MR

[1] Body mass index and body surface area [36].

[2] Pregnant Ella has different height and weight than Ella, due to segmentation changes.

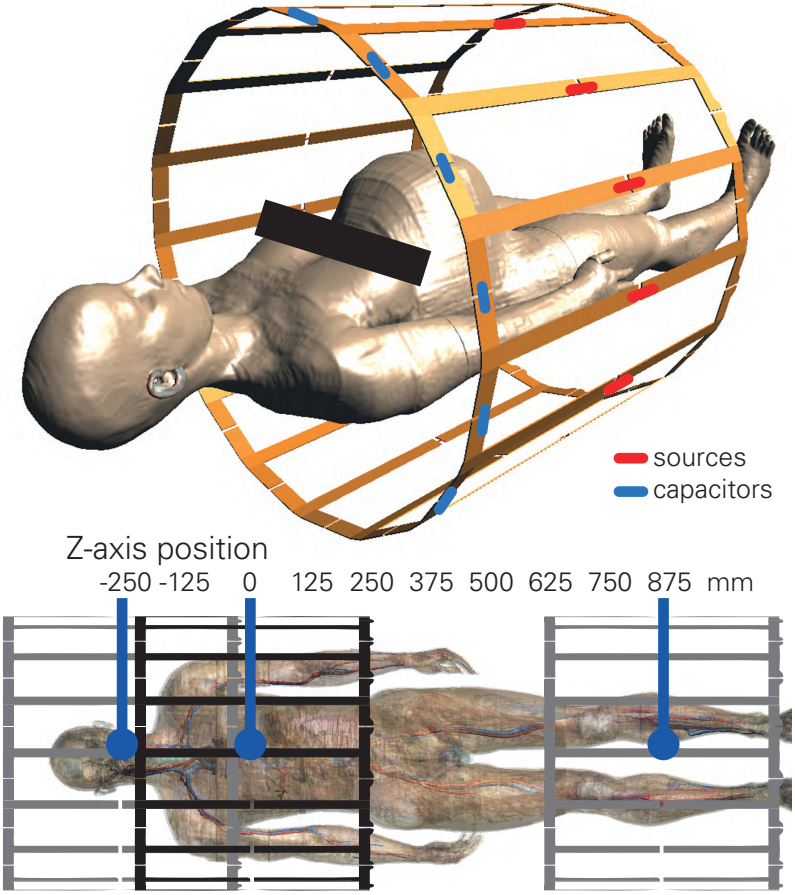

Figure 4.1: Top: generic birdcage body coil model with pregnant Ella. Bottom: positioning of anatomical models (graphic shows shifting of birdcage, assuming a fixed model position). Z=0 corresponds to the heart at the isocenter.

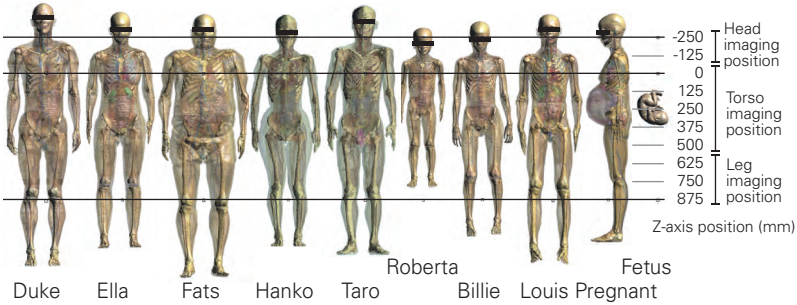

Figure 4.2: Anatomical models used for numerical evaluations, all with identical scaling and landmark position indication.

applications in terms of regional psSAR10g and wbSAR is marginal (<3%) as high- SAR regions always occur in peripheral areas. A generic 1.5 T birdcage model was used (16 rungs, 750 mm diameter, 650 mm length), with 16 phase-adjusted current sources in the rungs and 63.3 pF end-ring capacitors for symmetrical quadrature feed at 64 MHz. The models were placed in 10 shifted Z-positions (ΔZ=125 mm, values between Z=250 mm to Z=875 mm, with Z=0 mm corresponding to the heart at the isocenter, see Fig. 4.1). In the X and Y direction, the center of the heart was kept on the Z-axis. The evaluation of left-circular (B1+) and right-circular (B1−field orientations mainly revealed regional psSAR10g differences in the left/right arm regions, but remained below 15% otherwise. Results are therefore restrained to B1+ only. Anatomical RF loops were inhibited by ensuring a minimum of 2cm isolation between hands and hip, and between the inner thighs.

4.3.2 Electromagnetic Simulation

Numerical evaluation and dosimetry was conducted with SEMCAD X, V14.2 (SPEAG, Zurich, Switzerland). Due to the large number of simulations, a Huygens Box approach was applied [40]. The incident field was obtained for an empty birdcage with a grid optimized for the RF elements (minimum voxel size 0.4 mm). The result was used as input

for the Huygens Box simulations with the anatomical model and a uniform grid resolution of 2 mm (x,y,z). The effect of the backscattering on the coil system was neglected to enable comparison of the exposure of adults and children for the same incident field. For the approx. 50 million voxels of the entire simulation space, the calculation time was around 1 h per simulation on a hardware accelerated cluster (SPEAG, Zurich, Switzerland).

4.3.3 Data Evaluation

Results were extracted for

- whole-body SAR (wbSAR)
- partial-body SAR (pbSAR), including exposed patient mass according to (IEC, 2010)
- head SAR (hdSAR)
- regional peak spatial SAR averaged over 10g (psSAR10g) within five different body regions: left arm, right arm, head, trunk, both legs. For the pregnant model, the fetus and amniotic fluid were also processed as two additional body regions.
- average SAR (avSAR) of the amniotic fluid for the pregnant model

The region masks for the five body regions (seven when including the fetus and amniotic fluid) were applied to determine the distribution of the spatial SAR averaged over 10 g (sSAR10 g) with in the body, e.g., the psSAR10g of the fetus also included values from the surrounding tissues or amniotic fluid for the averaging algorithm.

The psSAR10g values were normalized to the desired MR OM, usually First Level Controlled according to [3], where the relevant guideline limits are wbSAR: 4 W/kg; hdSAR: 3.2 W/kg; and pbSAR: 4–10 W/kg. The Normal OM was applied for the pregnant model: hdSAR: 3.2 W/kg, wbSAR: 2 W/kg, pbSAR 2–10 W/kg. Estimation of the pbSAR is calculated as the average SAR of the exposed patient mass. The effective volume of the generic body coil is estimated to be within ±360 mm from the isocenter, following the procedure described in the standard [3].

4.4 Results

For a fixed $B1_{rms}$ field of 1 μT at the isocenter, wbSAR values up to 0.18 W/kg were obtained (children: 0.13 W/kg), hdSAR values up to 0.14 W/kg (children: 0.10 W/kg), and psSAR10g up to 3.2 W/kg (children 1.5 W/kg). The highest local SAR values were found in the arms for Z-positions with the abdomen in the isocenter (Z= +250 mm) (see Fig. 4.3).

On average, children reach 65% of the wbSAR but only 50% of the psSAR10g of the adult values. Thus, when normalizing to the wbSAR for the corresponding OM, the children's average psSAR10g still remains below the adult values.

Normalized to the First Level Controlled OM, this results in psSAR10g values of up to 104 W/kg for adults, 58 W/kg for children, and 14 W/kg in the fetus, where the exposure of the mother is limited by the regulations to the Normal OM.

There are no local SAR hotspots inside the skull or brain. Peak values tend to be around body hollows (axle, crotch), hard dielectric contrasts and body constrictions (e.g. knee joint, wrist).

Figure 4.3) illustrates the SAR normalization procedures for the model Ella. Four exposure scenarios were derived for statistical comparison: (1) regional psSAR10g values of the head are considered for head imaging positions; (2) in torso imaging positions, mainly the trunk and arms are exposed, and the arms have the highest regional psSAR10g values; (3) the legs are mainly exposed in the corresponding leg imaging positions; (4) the trunk is never at maximum exposure, but is significantly exposed in all positions. The first 3 exposure scenarios correspond well with the 3 different limitation procedures (wbSAR, hdSAR, pbSAR). Figure 4.4) shows exposure values of the pregnant model, including the fetus and amniotic fluid. The high average SAR (avSAR) of the non- perfused amniotic fluid may lead to an increased thermal load and indirect heating of the fetus. Exposure values are summarized in Table 2 and Figure 4.5).

Modeling of anatomical worst case RF loops show potential increases in psSAR10g of factor >>2. Figure 4.6 illustrates typical arm loops for Duke (arms turned off sideways, hands touch hip) and Billie (only hand-hip touching), demonstrating psSAR10g enhancements of factor 3 and 2.7 respectively.

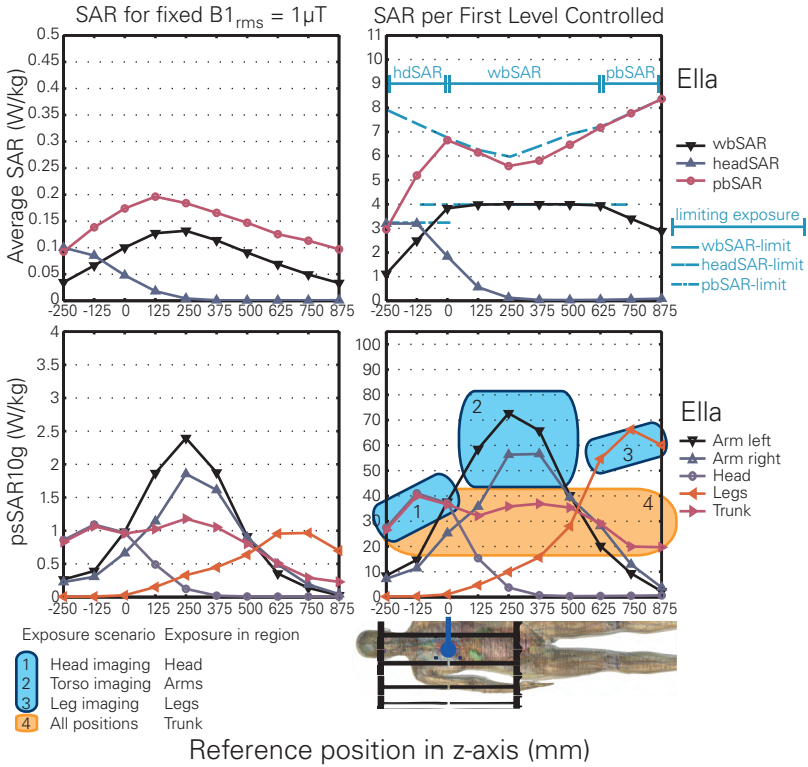

Figure 4.3: Exposure normalization illustrated for Ella. Left: values for a fixed $B1_{rms}$ = 1 mT field; right: normalized to First Level controlled OM, where head-averaged SAR (hdSAR), whole-body averaged SAR (wbSAR) and partial-body SAR (pbSAR) are limiting the exposure in different landmark positions. Top: averaged SAR values; bottom: corresponding local SAR values (psSAR10g).

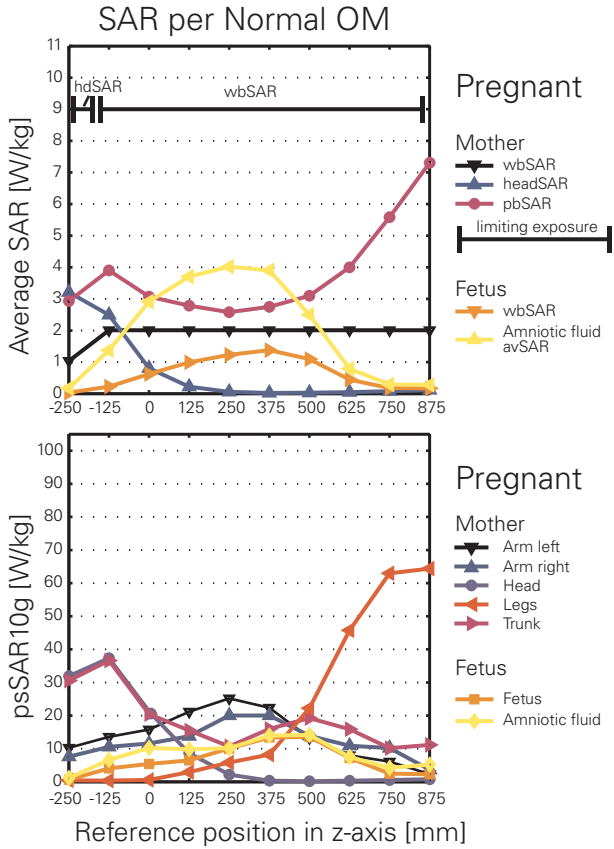

Figure 4.4: Eposure values of the pregnant model (mother and fetus) for NORMAL OM as function of landmark position. Top: whole-body (wbSAR), partial-body (pbSAR) and head SAR (hdSAR) values, bottom: peak spatial SAR values averaged over any 10 g of tissues (psSAR10g). In NORMAL OM the pbSAR does not reach a limiting function.

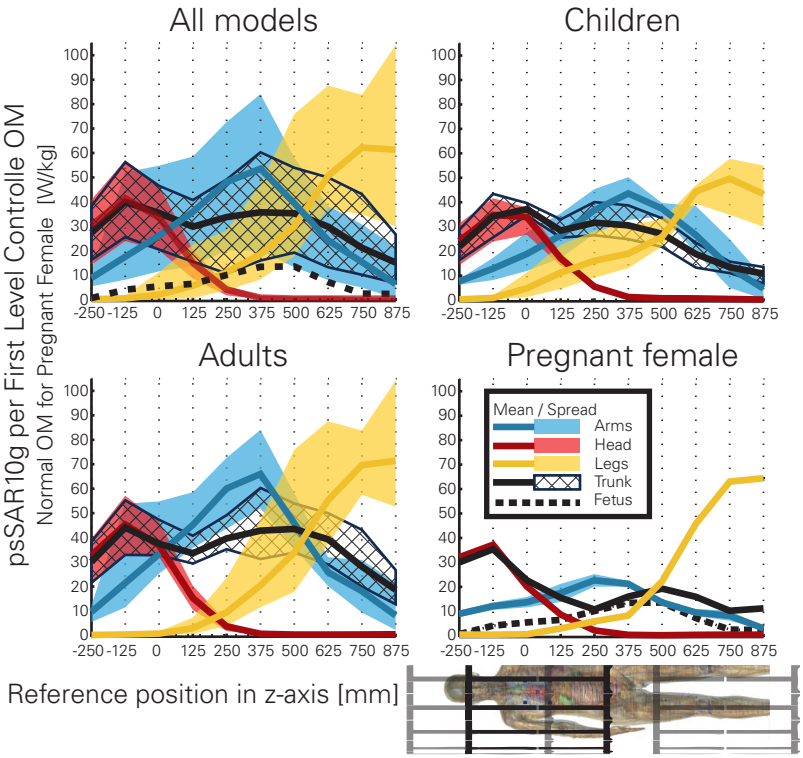

Figure 4.5: Maximum local psSAR10g as function of landmark position for different model subsets. Mean value (solid line) and min/max spread are shown. Children: Billie, Louis, Roberta. Adults: Ella, Duke, Hanako, Taro Fats.

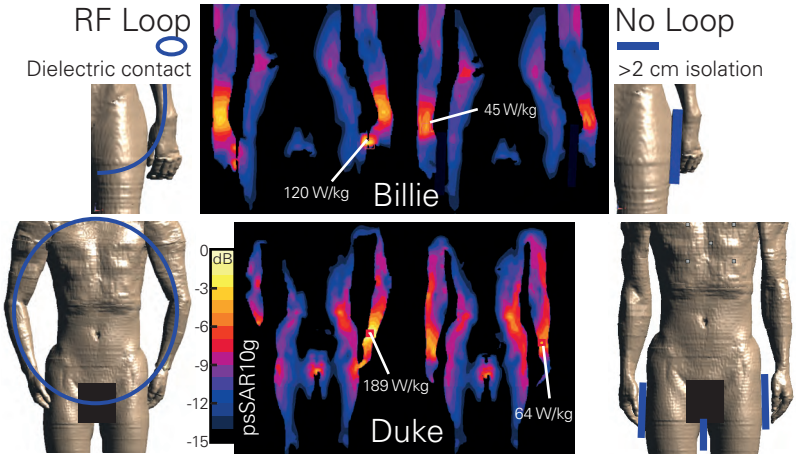

Figure 4.6: Illustration of SAR enhancement for Billie and Duke, with and without anatomical RF loop. All normalized to First Level Controlled OM , same position and slice.

4.5 Uncertainty Analysis

The numerical uncertainty analysis was performed with Duke, following the concept of NIST TN1297 [41]. The analysis included errors from (a) convergence, (b) model discretization, and (c) dielectric tissue properties. The combined RSS uncertainty remains below 11%, which is in agreement with the non-thermal uncertainty parameters of [39].

4.6 Discussion and Conclusion

In the First Level Controlled OM [3], the psSAR10g in adults may exceed 100 W/kg (potentially much higher when considering loops). Additional studies are necessary to evaluate the thermal load for extensive scanning time. In comparison, the local SAR hotspots in children of normal weight are weaker than in adults. Therefore, we conclude that no special safety considerations are needed for children.

The maximum exposure of the fetus with the mother at NORMAL OM is 13.6 W/kg psSAR10g, which is higher than the 9.2 W/kg estimated in [37] and the 3.1 W/kg in [42]. This is explained by our model being in a later gestational stage (36 weeks) and by the fact that the 10 g averaging cube was allowed to include neighboring tissues (e.g., amniotic fluid) in determining the psSAR10g of the fetus. The rational for the latter is that these tissues are thermally relevant. Values for the amniotic fluid are very similar (avSAR 4 W/kg, psSAR10g 14.2 W/kg in this study versus 3.4 W/kg and 12 W/kg in [42]. However, even though the fetus has no elevated psSAR10g, the effect of the high average SAR in the surrounding amniotic fluid must be care- fully evaluated in thermal considerations.

Chapter 5

Whole–Body and Local RF absorption in Human Models as a Function of Anatomy and Position within 1.5T MR Body Coil

5.1 Abstract

[1] **Purpose:** Radiofrequency (RF) energy deposition in magnetic resonance imaging (MRI) must be limited to prevent excessive heating of the patient. Correlations of RF absorption with large-scale anatomical features (e.g. height) are investigated in this paper.

Theory and Methods: The specific absorption rate (SAR), as the pivotal parameter for quantifying absorbed RF, increases with the radial dimension of the patient and therefore with the large-scale

[1] This Chapter has been published in [43].

anatomical properties. The absorbed energy in six human models has been modeled in different Z-positions (head to knees) within a 1.5T bodycoil.

Results: For a fixed B1+ incident field, the wbSAR can be up to 2.5 times higher (local SAR up to 7 times) in obese adult models compared to children. If the exposure is normalized to 4 W/kg whole-body SAR, the local SAR can well exceed the limits for local transmit coils and shows inter-subject variations of up to a factor of three.

Conclusion: The correlations between anatomy and induced local SAR are weak for normalized exposure, but strong for a fixed B1+ field, suggesting that anatomical properties could be utilized for fast SAR predictions. This study demonstrates that a representative virtual human population is indispensable for the investigation of local SAR levels.

5.2 Introduction

Magnetic resonance imaging (MRI) has become a routine technique in medical diagnostics. It is often superior to other imaging techniques, such as computer tomography (CT), due to its excellent soft-tissue contrast and its applicability in MR spectroscopy to non-invasively identify metabolic changes. MRI is deemed safe if the potential hazards, such as mechanical forces (static magnetic fields), nerve stimulation (gradient fields) and local and whole-body tissue heating by radiofrequency (RF) fields, are carefully managed. Tissue heating is controlled for volume coils by limiting the whole-body SAR (wbSAR), head SAR and partial-body SAR (pbSAR) as defined in the IEC product standard [3]. The limitation values for the two relevant operating modes (OM), (a) normal and (b) first level controlled, are given in Table 5.1.

Induced eddy currents are the primary RF absorption mechanism of the B1 magnetic field exposures with the human body, i.e., the highest energy deposition usually occurs in bodies with large tissue cross-sections. Therefore, large-scale anatomical properties may significantly influence the energy absorption levels. Recent studies have evaluated only a small number of anatomical models or positions, e.g., [34, 44], or they have not explored correlations to large-scale anatom-

ical properties [33]. The induced eddy currents depend mainly on the cross-section of the body and the field strength normal to the cross-section and are therefore largely independent of birdcage design and X-Y-position of the human within the birdcage. In general, the B1 field is rather homogenous in the field of view (FOV); it is larger near the metallic structure and decreases along the Z-axis. The formation of RF loops formed by the extremities may dramatically increase local SAR [33] and should thus be avoided.

The secondary RF absorption mechanism is the capacitive coupling of stray E-fields, predominantly close to the matching capacitors. The stray E-fields expose the tissues in close proximity to the rungs and endrings, and strongly depend on the actual coil design (e.g. capacities in the rungs, distance of the shield). The size of the body has no direct influence on the stray E-field absorption pattern.

The actual exposure is a superposition of B1-induced eddy current absorption and the localized stray E-field exposure. The effects of the stray E-fields are limited to the arm regions for typical (centered) postures, and therefore have a minor influence on trunk exposure and wbSAR. As stray E-fields are very design specific and a generalization is not possible, within this study, we focused on the B1-induced eddy current related exposure. Three children and three adult models were exposed (a) to a fixed incident B1+-field of $1\mu T$ in the center of the empty birdcage, and (b) to an RF excitation level normalized to the maximum allowed average output power according to the first level controlled OM. Simulations were performed for 10 different Z-positions (head to knees) within a generic 1.5 Tesla MR body-coil at 64 MHz. The following physical large-scale anatomical properties (Table 5.1). are put into context with the numerically derived SAR values:

- Unidimensional: body height, shoulder length
- Bidimensional: body surface area (BSA), frontal projection area (FPA), RF exposed FPA (eFPA)
- Volumetric: body weight
- Shape related: body mass index (BMI).

The goal of this study is to evaluate the influence of large-scale anatomical properties on the whole-body averaged and local SAR. The aim is to clarify whether data about the coarse body size and shape is helpful for estimating the RF energy deposition during MR exposure.

	Normal OM (W/kg)	First Level Controlled OM (W/kg)
Body coils		
wbSAR	2	4
Head SAR	3.2	3.2
pbSAR[1]	2–10	4–10
psSAR10g	Not Limited	Not limited
Local transmit coils		
psSAR10g head and trunk	10	20 (can reach > 60 W/kg in body coils)
psSAR10g extremities	20	40 (can reach > 100 W/kg in body coils)

Table 5.1: SAR limitations as defined in [3] for body coils and local transmit coils.

5.3 Methods

The evaluation was based on six anatomical human models (see Figure 5.1 and Table 5.2). The children Billie, Louis, and Roberta, and the adults Duke, Fats, and Ella are components of the Virtual Population [35] (www.itis.ethz.com/vip). All models were positioned in a standard posture, i.e., lying on the back with the heart centered on the boresight axis. Their minimal distance to the birdcage varied from 34 mm for Fats to 183 mm for Roberta (Table 5.2). To evaluate the effect of rung proximity, Roberta was additionally simulated with a laterally shifted position, such that her proximity to the birdcage was identical to that of Fats. RF loops formed by the extremities were

[1] partial-body SAR scales dynamically with the ratio r = exposed patient mass/total patient mass; Normal Mode: SARpartial-body = (10 – 8 · r) W/kg; First Level Mode: SARpartial-body = (10 – 6 · r) W/kg.

suppressed by ensuring a minimal distance of 20 mm between hand and hip, and between the inner thighs (recommended practice by the manufacturers).

Simulation scenarios were identical to Murbach et al. [33], in which simulations for 10 different landmark positions ($\Delta Z = 125$ mm, head to knees) within a generic 1.5T birdcage model were evaluated. Most simulations were performed in a long birdcage (large B1 volume): 64 MHz, high-pass, leg feed, 16 rungs with 16 current sources, 750 mm diameter, 650 mm length, shield 40 mm radial distance to birdcage, 63 pF capacities in the endrings, B1 circularly polarized (CP) and rotating clockwise when looking in Z-direction. The second one was a short birdcage of 400mm length while the other dimensions are identical to the first coil with rung capacities of 88 pF. The applied Huygens box approach [33] ensured identical birdcage current distributions for all models and positions. The birdcages were tuned to the resonance frequency using a broadband quadrature excitation with two ports in one endring. Thus, the applied incident fields correspond to an ideal CP current distribution. Altered current distributions due to loadings were not evaluated in this study as they depend on the design and implementation.

	AP1	AP2	AP3	AP4	AP5	AP6	AP7	Position
Model (y-f/m)	weight [kg]	height [m]	BMI [kg/m^2]	BSA [m^2]	shoulder len. [m]	FPA [m^2]	eFPA [m^2]	min. dist. to coil [m]
Roberta (5f)	17.9	1.09	14.9	0.73	0.29	0.22	0.11-0.17	0.183
Billie (11f)	35.4	1.47	16.5	1.2	0.36	0.37	0.12-0.24	0.145
Louis (14m)	51.9	1.69	18.2	1.53	0.41	0.47	0.14-0.28	0.096
Ella (26f)	59.1	1.63	22.2	1.61	0.43	0.5	0.14-0.30	0.104
Duke (34m)	76.2	1.77	24.3	1.87	0.5	0.55	0.14-0.33	0.078
Fats (37m)	120.2	1.82	36.4	2.44	0.51	0.71	0.18-0.45	0.034

Table 5.2: Anatomical Models and Large-Scale Properties AP1–AP7 Used for Simulations. AP7 scales dynamically with the model-position. The minimum distance to the coil depends on the lateral dimensions of the heart-centered models.

The dielectric tissue properties were assigned according to the comprehensive literature review of Hasgall (www.itis.ethz.ch/database), the recommended dielectric properties of which are largely identical to those proposed by Gabriel et al. [17]. Details about the electromag-

netic (EM) simulations have been reported earlier [33]. All simulations were performed with SEMCAD X Version 14.8, the simulation platform developed in-house jointly with SPEAG (Zurich, Switzerland) and commercialized by the latter, with a uniform and isotropic grid resolution of 2 mm. The data evaluation was based on wbSAR, head SAR, pbSAR (these values are necessary for normalization to the operating mode), and peak spatial SAR averaged over any 10 g of tissue (psSAR10g) for local peak SAR [7]. Simulations were performed with the fixed birdcage current distribution resulting in an incident B1+ of 1 μT at the isocenter (B1 more than 40 dB lower than B1+). With the presence of the anatomical models, the induced eddy currents alter B1 (Total field = incident field + scattered field). Normalization to the maximum allowance in the first level controlled OM was performed according to the standard [3].

For SAR comparison across the models, landmark positions were defined relative to the models' torso-heights (0% corresponding to the shoulder, 100% to the groin, Figure 5.1), since the basic anatomical torso dimensions are essential for constraining the induced eddy current patterns (Figure 5.2). Therefore, SAR values were interpolated (piecewise cubic) from the original spacing in the actual simulations (ΔZ = 125 mm) and assigned to a 10% relative torso-height grid, which corresponds to an interpolated ΔZ between 44 mm (Roberta) and 79 mm (Fats) for the different models. The heart position was between 20% and 30%. Shoulder and groin positions were identical across the models (i.e., 0% and 100%).

The investigated large-scale anatomical properties (AP1–7) used for deriving the correlations can be found in Table 5.2, together with the actual values for the anatomical models and their minimum distance to the birdcage. The FPA (frontal projection area of the X-Z-plane, Figure 5.1) was selected, as it represents the largest projection of the human body, and therefore allows high induced eddy currents. The eFPA corresponded to the projection area within the active region of the birdcage coil (±360 mm in Z-direction from the isocenter) and depended on the actual model position.

A non-linear correlation between large-scale anatomical properties and SAR is expected with several transition zones between different correlation-mechanisms (e.g., from small models almost entirely inside the birdcage towards models or positions with large portions out-

side the B1 field). The correlation function should also depend on the nature of the large-scale anatomical property; the unidimensional (height, shoulder length), bidimensional (BSA, FPA, eFPA), volumetric (weight) and shape related (BMI) anatomical properties have different influences on SAR. Overall, the usage of simple linear regression lines showed the most consistent correlations, expressing the fitted SAR $\hat{S}_m$ for model m as a function of its large-scale anatomical property (AP_m) as

$$\hat{S}_m = f(AP_m) = a \cdot AP_m + b \tag{5.1}$$

with the slope of the regression line a and the offset b. An ideal linear correlation would result in a zero-offset, since there can be no SAR without some tissue. However, this correlation model serves well as a local linear approximation of the actual non-linear relation, as introducing more complex functions ($\propto AP_m^2$ or $\propto AP_m^{3/2}$) did not improve the predictions. For evaluating the correlation between the large-scale anatomical properties (AP1–7) and SAR, the coefficient of determination r^2 is introduced as

$$r^2 = 1 - \frac{\sum_m (S_m - \hat{S}_m)^2}{\sum_m (S_m - \bar{S})^2} \tag{5.2}$$

where $\hat{S}_m$ is defined in Equation 5.1, S_m is the actual SAR (either wbSAR or psSAR10g) of the model m and $\bar{S}$ is the average SAR over all 6 models.

5.4 Results

Figure 5.3 shows SAR values for all models and the corresponding coefficients of determination (r^2). In most cases, Roberta had the lowest exposure values and Fats the highest. As reported earlier [33], the psSAR10g in the first level controlled OM can reach values well above the current restrictions for surface coils (20 W/kg in the torso and 40 W/kg in the extremities, Table 5.1). The values for Fats can exceed 60 W/kg (torso) and 80 W/kg (arms), while the predicted > 100 W/kg in the legs would require an average power fed to the coil that is beyond the capacity of RF amplifiers in today's scanners.

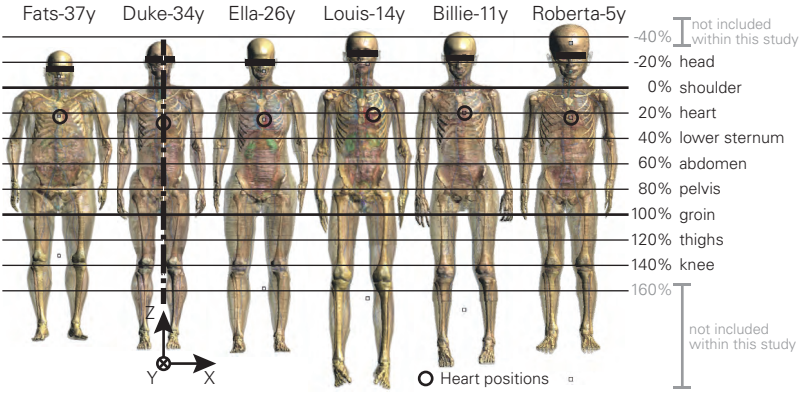

Figure 5.1: The six anatomical models (size is normalized to torso-height) used in electromagnetic simulations and their landmark positions. Electromagnetic simulations were conducted with the original size.

Generally, the best correlation values were found for BSA, shoulder length and (exposed) frontal projection area. For a fixed B1+ field, the wbSAR values differed by up to a factor of 2.5 between the models, and good correlation with the anatomy in torso positions (landmark 0–80%, $r^2 < 0.8$, Figure 5.3b) was achieved. The psSAR10g reached a 7-fold increase for large models with good correlations, except for the groin imaging positions (80–100%, $r^2 < 0.8$, Figure 5.3b).

When normalizing to first level controlled OM (i.e., in most cases, to wbSAR = 4 W/kg) psSAR10g varied by a factor of 3, indicating variations in the relative distribution of the induced fields due to (a) different relative extents of the B1 field and (b) small-scale anatomy. These variations, however, cannot be reliably predicted based on large-scale anatomical properties (generally $r^2 < 0.8$, Figure 5.3c), although there clearly is some relationship. Figure 5.4 shows four selected example correlations, plotting psSAR10g in all models against the large-scale anatomical property of the body surface area (BSA). Good linearity was achieved for a fixed B1+ field and for certain landmarks (e.g., the depicted 20% landmark shows better cor-

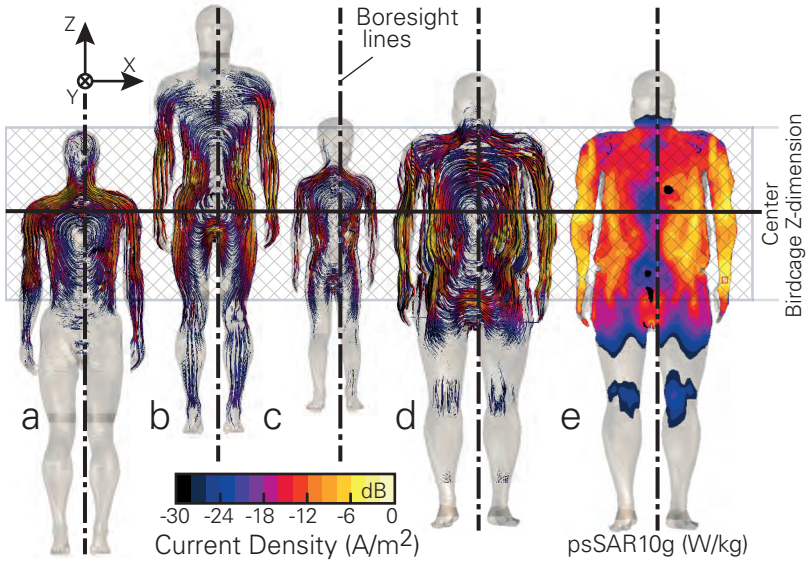

Figure 5.2: a–d: Streamline views of the simulated induced eddy current densities (phase of B1 with the highest rate of change in Y-direction is shown, resulting in maximum current induction). The shaded area indicates the birdcage dimension in Z-direction. a: Duke (20% landmark) with the highest densities at the shoulders, esp. constricted near the neck. b: (80% landmark) constriction at the groin with resulting high densities. c+d: Roberta and Fats (40% landmark). The torso dimensions mainly restrain the typical eddy-current patterns. e: psSAR10g slice view of Fats, actual peak in wrist. Models are exposed to (a–d) an incident B1+ of 1 μT at isocenter in the empty birdcage, 0 dB corresponds to 100 A/m^2, and (e) maximum allowance in first level OM, 0 dB corresponds to 80 W/kg.

relation than the 90% landmark). The r^2 value was significantly lower for OM normalized exposure (Fig. 4b).

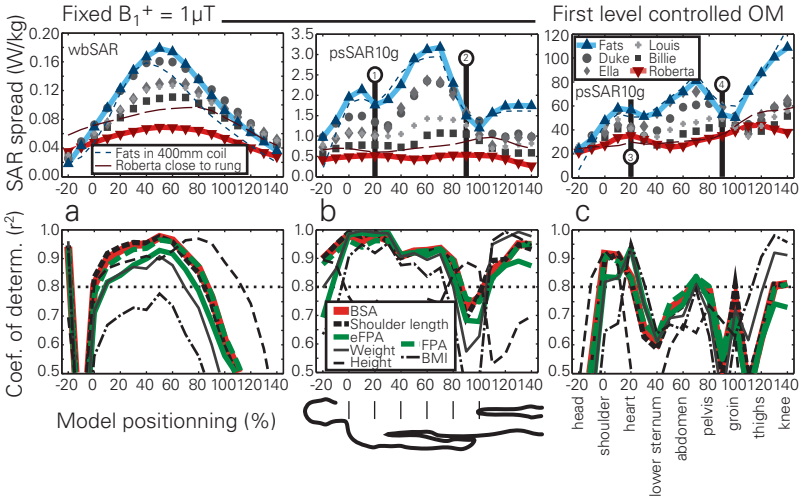

Figure 5.3: a: wbSAR and (b+c) psSAR10g variation between the six different human models, and corresponding coefficients of determination between SAR and the large-scale anatomical properties. Normalization to a fixed B1+ (a+b) and to first level OM (c). Lower r^2 values are found for OM-normalized psSAR10g, and for BMI, weight and height (except for leg positions). Indicated correlations for two landmark positions of interest (20% and 90%) (circles 1–4) are illustrated in Figure 5.4. For comparison, SAR values are shown for Roberta close to rung (identical distance to the birdcage as Fats) and Fats in a shorter (400 mm) coil.

5.5 Numerical Uncertainty

The uncertainty of our results, i.e., wbSAR, psSAR10g and subsequently r^2, was determined based on the modeling parameter uncertainties from the underlying electromagnetic simulation, following the

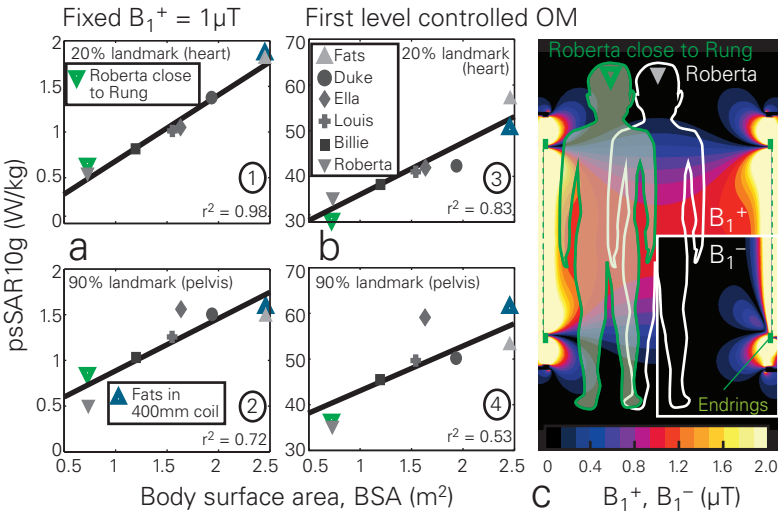

Figure 5.4: psSAR10g for the different human models as a function of the body surface area (BSA). Graphs are shown for a fixed B1+ field (a) and normalized to First Level Controlled OM (b), and for two landmark positions of interest (20% and 90%). The coefficient of determination is indicated, and corresponding data values from each plot are shown in Figure 5.3 (circles 1–4). c: Roberta in standard positioning within the birdcage incident field (B1+ $= 1\ \mu T$ at isocenter, 90% landmark), and laterally shifted to the same endring distance as Fats.

concept of NIST TN1297 [41]. The combined uncertainty (RSS) was estimated to be 0.41 dB (∼9%) for wbSAR and 0.52 dB (∼12%) for psSAR10g, both in agreement with Bakker et al. [39], i.e., 10.6 and 11.7% (see Table 5.3). The uncertainty for the calculated r^2-values is non-linear (Equation 5.2). Approximated values are estimated for what is likely to cause the highest error deviations ($-u_i$ for Fats and Roberta, and $+u_i$ for the other models between).

Parameter	Range	u_i	
EM Simulation		wbSAR	psSAR10g
Convergence	Simulation length: +100%	0.03 dB	0.03 dB
Model discretization	Voxel size: 1.5, 3 mm	0.01 dB	0.26 dB
Dielectric parameter	$\sigma : \pm$ 10% (all tissues)	0.10 dB	0.15 dB
Dielectric parameter	$\varepsilon : \pm$ 10% (all tissues)	0.07 dB	0.09 dB
Dielectric contrast	$\sigma : \pm$ 10% (single tissue[1])	0.08 dB	0.17 dB
Dielectric contrast	$\varepsilon : \pm$ 10% (single tissue[1])	0.04 dB	0.04 dB
Density	$\rho : \pm$ 10%	0.26 dB	0.26 dB
Segmentation errors	Quality of models [39]	0.28 dB	0.28 dB
SAR uncertainty, RSS		**0.41 dB (∼ 9%)**	**0.51 dB (∼ 12%)**
r^2 **uncertainty**	$r^2 > 0.95$	< 0.13 dB	(< 3%)
	$r^2 \leq 0.95$	< 0.31 dB	(<7%)

Table 5.3: Standard uncertainty values are standard deviations (k = 1) in the assumed log-normal probability distribution. Because they are uncorrelated, they can be combined by root-sum-square (RSS) procedures.

5.6 Discussion

For comparing SAR across different models, their relative positions within the birdcage were normalized to achieve similar exposure conditions. Using actual Z-positions or normalization to overall model height caused large differences (100–300 mm) in the relative location of the shoulder and groin due to differences in size and relative sizes, e.g., leg-to-body ratio. As the trunk dimensions significantly influence

[1] muscle, skin, and fat evaluated

the induced eddy current pattern (Figure 5.2), the best landmark normalization in terms of SAR correlation is achieved for normalization to torso dimensions. The residual non-correlation between the models consequently originates from (a) the remaining differences in the exposure scenario (relative extent of the homogeneous B1 field, proximity to birdcage) and (b) the differences in small-scale anatomical properties of the models. Future studies could further investigate the underlying mechanisms.

Except for leg positions, weight, height and BMI tend to have lower r^2 values, and show a low coherence in all positions (large differences for different landmark positions), i.e., the relative distribution of induced fields is poorly correlated with these parameters. BSA, shoulder length and (exposed) frontal projection area show very similar correlations, with generally less than 10% deviation from each other. The wbSAR values (Figure 5.3a) show satisfying correlations with the large-scale anatomical properties for thorax positions (0–80% landmarks). For very remote landmarks (e.g. –20%), the relation is inversed due to the large unexposed parts, while transition zones (–15 to 0%, > 80%) do not allow wbSAR predictions based on large-scale anatomical properties.

As psSAR10g values for a fixed B1+ field (Figure 5.3b) do not depend on non-exposed masses, correlations are generally good, with $r^2 > 0.8$ for most positions. For lower abdomen imaging (80–100%), small-scale anatomical variations around the groin, wrists, and hands are predominant, thus reducing the r2 values for large-scale anatomical properties. When normalizing to the first level controlled OM (Figure 5.3c), differences in psSAR10g across the models are reduced by approximately two. Correlations generally decrease below $r^2 = 0.8$, resulting in uncertain direct psSAR10g predictions.

For psSAR10g limitation regimes, B1+ levels in combination with patient anatomy information may thus be a better safety predictor than wbSAR, i.e., maximum allowed averaged input power could be derived based on the patient's position and large-scale anatomical properties. A combination of wbSAR, B1+ levels, anatomy and position may yield a more reliable safety management for psSAR10g. In addition to direct influences from anatomy on SAR, the formation of anatomical RF loops (e.g., hand/hip or knee/knee touching) increase the psSAR10g values by a factor $\gg$2 with unchanged B1 and wbSAR

levels [33]. Thus, the stated correlations are valid only when strictly inhibiting RF loops caused by physical contact of extremities.

To investigate effects of asymmetric positions, the Roberta model has been shifted though the Z-axis positions with identical lateral distance to the birdcage as Fats (34 mm instead of 183 mm). This results in a smaller average distance between the birdcage and the trunk, and higher incident B1 fields due to the characteristic field distribution of the birdcage (see Figure 5.4c). As indicated in Figure 5.3a, wbSAR shows a constant increase in all positions. The psSAR10g for a fixed B1+ (Figure 5.3b) is almost identical at the 20% landmark (where the arm is between the two endrings), and elevated when the arm is in close proximity to the endring. The simulations with Fats within a much shorter (400 mm) birdcage revealed small deviations compared to the long birdcage (650 mm) in terms of psSAR10g ($< 10\%$ in most landmarks), while wbSAR values are smaller, as expected, due to the smaller extent of the B1 field (Figure 5.3). Even when including these two variations (lateral shift and shorter birdcage), correlations with $r^2 > 0.8$ can be found in centered torso positions (20–60%) for wbSAR, and in most torso positions (0–80%) for psSAR10g.

5.7 Conclusion

Local SAR levels in the normal and first level controlled OM may exceed the limits for local transmit coils by more than a factor of three. For a fixed incident B1+ field, psSAR10g values can be estimated from large-scale anatomical properties. When normalizing to the operating modes, this prediction is no longer reliable, leaving small-scale anatomy and local body shapes as the relevant parameters for exposure differences between the human models. The variation in psSAR10g, however, still shows a factor of approximately three.

Our study results suggest that in the future, anatomical properties could be utilized for fast local SAR predictions. For this, a representative population of anatomically correct human models is indispensable to accurately estimate safe local SAR levels and to estimate the actual SAR correlations.

5.8 Acknowledgements

This study was supported by the EUREKA (E!4144) and CTI (9193.1) project MRI+.

Chapter 6

Thermal Damage Tissue Models Analyzed for Different Whole-Body SAR and Scan Duration for Standard MR Body Coils

6.1 Abstract

[1]**Purpose:** This paper investigates the safety of radiofrequency (RF) induced local thermal hotspots within a 1.5T bodycoil by assessing the transient local peak temperatures as a function of exposure level and local thermoregulation in four anatomical human models in different Z-positions.

Methods: To quantize the effective thermal stress of the tissues, the thermal dose model CEM43 (cumulative equivalent minutes at

[1]This Chapter has been published in [45].

43°C) was employed, allowing the prediction of thermal tissue damage risk and the identification of potentially hazardous MR scan-scenarios. The numerical results were validated by B1+- and skin temperature measurements.

Results: At continuous 4 W/kg whole-body exposure, peak tissue temperatures of up to 42.8°C were computed for the thermoregulated model (60°C in non-regulated case). When applying CEM43 damage thresholds of 15 min (muscle, skin, fat, bone) and 2 min (other), possible tissue damage cannot be excluded after 25 min for the thermoregulated model (4 min in non-regulated).

Conclusion: The results are found to be consistent with the history of safe use in MR scanning, but not with current safety guidelines. For future safety concepts, we suggest to use thermal dose models instead of temperatures or SAR. Special safety concerns for patients with impaired thermoregulation (e.g., the elderly, diabetics) should be addressed.

6.2 Introduction

Magnetic resonance imaging (MRI) has established itself as a routine technique in medical diagnostics. The absence of ionizing radiation and the excellent soft-tissue contrast are major advantages of MR systems compared to computer tomography (CT). Guidelines have been developed [3] to avoid potential patient risks due to (a) mechanical torque of metallic implants and acceleration of ferromagnetic objects, both by the static field, (b) nerve stimulation by the gradient fields, and (c) local tissue and whole-body heating by the radiofrequency (RF) fields. The history of safe use [30] indicates that quadrature-driven volume or body coils – as applied until today – are safe, when operated according to the guidelines.

In this paper, we analyze the locally induced temperature rise as a function of scantime for different whole-body specific absorption rates (wbSAR) and different imaging positions. The estimated transient temperature increases are then translated into effective thermal load, applying the thermal dose model of cumulative equivalent minutes at 43°C (CEM43) [23]. From literature values for maximum tolerable CEM43-doses [25], maximum allowed scantimes before potential tissue

damage occurs can be derived.

The CEM43 dose model expresses the thermal load on living tissues by estimating the equivalent induced thermal stress in minutes at 43°C. For example, exposing skin tissue for 16 min to 43°C (CEM43 = 16 min) causes equivalent symptoms as 64 min at 42°C, or 1 min at 47°C. Different tissues have different resiliences to thermal load. While skin may tolerate more than CEM43 = 40 min, more sensitive structures (e.g., blood brain barrier) show significant adverse effects already at CEM43 = 2 min.

In the current standard, absolute peak tissue temperatures are the governing limits, with maximum local tissue temperature of 40°C in the first level controlled operating mode (OM) according to [3]. It is also stated that higher temperatures are accepted for specific tissues if no unacceptable risk for the patient occurs. However, there are no guidelines on how to control these limits. Only the wbSAR and partial-body SAR (pbSAR) limits are provided, and these correlate poorly with localized exposure (e.g. peak spatial SAR averaged over any 10 g of tissue, psSAR10g) [33], and even less so with the local temperature increase, as shown in this study.

Assuming temperature independent dielectric parameters as a first approximation, the SAR distribution can be determined and translated to the induced temporal temperature distribution via a thermal simulation. Key parameters that determine local temperature increases are: (a) the electromagnetic exposure level; (b) the spatial distribution of SAR, specific heat capacity, thermal conductivity, metabolic heat generation, and transient blood perfusion of the tissue; and (c) the thermal boundary conditions (convection, sweating, etc.).

RF induced temperature increases and local hotspots due to MR exposures were analyzed using anatomical models, e.g., in [34, 46, 42]. The strong temperature dependence of perfusion has been considered [34, 21], but without employing a transient thermal dose model (CEM43). Various thermoregulatory effects exist, such as whole-body thermoregulation [47], redistribution of blood between body compartments and tissues [22] and local thermoregulation [48]. The latter is particularly important with regard to local hotspots resulting from MRI-induced heating [21].

Local SAR correlates poorly with temperature increase, even with temperature independent perfusion values, because of the vast tis-

sue parameter inhomogeneities in the human body. Non-linear local thermoregulation yields even weaker correlations. As the temperature weighted time-integrals correlate best with tissue damage, safety guidelines should be based on thermal dose models rather than local SAR or wbSAR limits. We, therefore, investigated the CEM43 dose concept [25] to estimate potentially hazardous combinations of exposure levels and MR scan setup configurations.

The overall goal of this study was to propose a novel safety approach for MR RF exposures based on thermal dose models by:

- translating different MR RF exposure scenarios to transient temperature increases in realistic human models and various imaging positions
- determining the impact of local thermoregulation
- estimating cumulative equivalent minutes (CEM43) for different tissues in the transient heating process
- deriving maximum scan times before reaching tissue-specific thermal dose thresholds.
- identifying potential hazardous MR scan scenarios and comparing those with the history of safe use
- validating the simulation models with B1+ and skin-temperature measurements in one healthy subject

6.3 Methods

6.3.1 Anatomical Models and Simulation Scenario

Anatomical Models and Simulation Scenario The evaluation was based on four different anatomical human models: Fats (m, 37y, 1.81 m, 120 kg) representing an obese male; Duke (m, 34y, 1.78 m, 76 kg), an average sized adult male; Ella (f, 26y, 1.63 m, 59 kg) an anatomically smaller female model; and Billie (f, 11y, 1.45 m, 35.6 kg), a child. They were positioned in ten different Z-axis landmarks to identify the worst case exposure scenario. The selected models of the Virtual Population ([35], www.itis.ethz.com/vip) are based on image data with a

resolution better than $0.9 \times 0.9 \times 2$ mm^3, and consist of more than 69 different organs and tissues which have been reconstructed as triangular surface meshes allowing for flexible discretization. The models and their positioning are depicted in Fig. 1, together with the generic 1.5 T birdcage models. The first model is the conservative birdcage with respect to B1 excitation as defined in the ISO/TS10974 [49] (high-pass, leg feed, 16 rungs with 16 current sources, 750 mm diameter, 650 mm length, tuned to 64 MHz circular polarization). The second birdcage is 400 mm long representing a shorter, more realistic birdcage. The simulation scenarios are as described in [33].

6.3.2 Tissue Properties and Local Thermoregulation

The dielectric and basal thermal tissue properties (including the metabolic heat generation rate) were assigned according to the comprehensive literature review of Hasgall (www.itis.ethz.ch/database), the recommended dielectric properties of which are largely identical to those proposed in [17]. All digestive lumina were modeled as filled with air [33]. Thermal boundary conditions for systemic thermoregulation (sweating, breathing) are discussed later in the thermal simulation section.

Accurate modeling of the local thermoregulation in human is challenging, as many parameters have systemic thresholds and interactions (e.g. sweating onset; increases in blood perfusion, metabolic rates, and cardiac output), which are also dependent on the extent of heat administration. Delayed temporal responses, thermal memories, and large inter-subject variations further complicate predictions. For local hotspots above 20 W/kg psSAR10g, thermoregulated local perfusion is the most important parameter for RF induced temperature increase [21], and is also the major tissue response to hyperthermia [50]. Experimental assessments in humans are rare and usually date back some decades. They generally show perfusion saturation above 43–45°C, but state different onset temperatures (34–42°C) and also have some differences in basal perfusion values.

Entire forearm perfusion in 5 subjects showed an exponential 10-fold increase between 34 and 45°C [51] and an overall 10-fold increase in 6 subjects at an elevated core temperature of 38°C [20]. The forearm

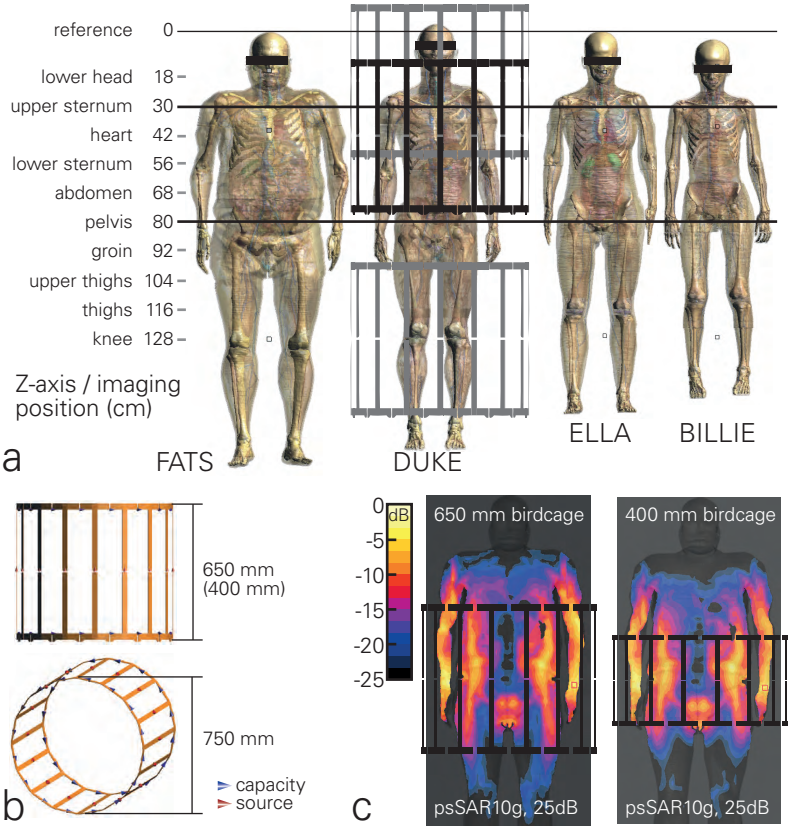

Figure 6.1: a: The four anatomical models used in electromagnetic and thermal simulations and their positioning within the 1.5T birdcage (assuming fixed model position and movement of the birdcage). Imaging positions are indicated. b: 16-rung birdcage, 650 mm length used in general for the simulations, 400 mm for comparison. c: Illustrative SAR distribution for Fats in pelvis imaging position within the two birdcages.

skin blood flow is reported to increase about 15-fold between 37 and 45°C (16). Thermoregulated muscle blood flow in the thighs of more than 20 subjects has been assessed by measuring the Xe133 washout by X-ray (19), estimating a very steep 16-fold increase. Perfusion in fat is estimated to reach a 10-fold increase at 45°C to match an experimental study in 5 subjects (20). Clinical hyperthermia studies estimate even higher thermoregulation capabilities, with a 42-fold increase in skin and 17-fold increase in muscle, to match their numerous experimental results (> 3000 clinical hyperthermia treatments) (21). Most of the recent modeling studies may have underestimated thermoregulation by applying increase factors up to 4 only (summarized in [21]), while Laakso et al. [21] argues for a 32-fold (skin) and 15-fold (other tissues) perfusion increase, which starts directly at basal temperature.

Based on this data, we widely followed the suggested model of Laakso et al. [21], with two differences: (a) we applied thermoregulation to skin, muscle and fat only, as literature values are more abundant and peak temperatures exclusively occur within these three tissues; and (b) the increase depends on absolute temperatures (not on the local temperature increase), because our validation measurements in human skin did not support the assumption of significant perfusion increase below 37°C. Thus, compared to Laakso, our thermoregulation model is less aggressive for tissues with basal temperatures below 37°C (mainly skin) and does not include other tissues. It models an exponentially temperature dependent increase factor of 32 for skin (from 37 to 45°C), and a factor of 15 for muscle and fat (from 37 to 43.3°C). The blood flow can be expressed as (similar to [21])

$$\begin{aligned} B(T) &= B_0 \cdot L_b(t) \\ L_b(T) &= 1, \qquad T < 37°C \\ L_b(T) &= 2^{\frac{T-37}{\Delta B}}, \qquad T \geq 37°C \\ max(L_b) &= 32(skin), 15(muscle, fat) \end{aligned} \tag{6.1}$$

where $B(T)$ is the perfusion rate at temperature T, $L_b(T)$ the local temperature dependent multiplier, B_0 is the basal perfusion at or below 37°C, and ΔB (the local vasodilation parameter) = 1.6 to match the desired temperature dependent perfusion increase. The

thermoregulated perfusion model is visualized in Figure 6.2. For all considerations, fat also includes subcutaneous adipose tissue (SAT).

Data analysis was performed for:

- constant (basal) perfusion (modeling a completely dysfunctional thermoregulation)
- muscle, skin, and fat thermoregulated (fully functional/normal)

Although thermoregulatory processes show typical response times in the order of 10 min, instantaneous regulation was implemented. This may result in a perfusion overestimation, especially within the first 10 min of heating (before full physiological response). Cardiac output increase is included in the local perfusion increase model. The impact of sweating, room temperature, and breathing is discussed in the next section. No other temperature related effects were considered, e.g., (a) change of electromagnetic energy absorption-distribution due to thermoregulation dependent dielectric parameter, (b) increased perfusion in tissues other than muscle, skin, and fat due to the higher cardiac output, (c) stealing effect (11), or (d) behavioral thermoregulation, where the patient may tend to change posture when feeling excess heat.

6.3.3 Electromagnetic and Thermal Simulation

Details of the electromagnetic (EM) simulations can be found in [33]. All simulations were performed using the finite difference time domain (FDTD) method with a uniform and isotropic grid resolution of 2 mm. The SAR distributions were used as input for the thermal simulations, which were conducted with SEMCAD X, V14.8 (jointly developed with SPEAG, Zurich, Switzerland), based on the extended Pennes Bioheat equation (PBE, Eqn. 6.2):

$$\begin{aligned} \rho c \frac{\partial T}{\partial t} &= \nabla \cdot (k(\vec{r}) \nabla T(\vec{r}, t)) + g(\vec{(r)}, t) \\ g(\vec{r}, t) &= \rho Q + \rho S - \rho_b c_b \rho B (T - T_b) \end{aligned} \tag{6.2}$$

where T is the temperature at location $\vec{r}$ and time t, c the specific heat capacity, k the thermal conductivity, ρ the density, B the perfusion

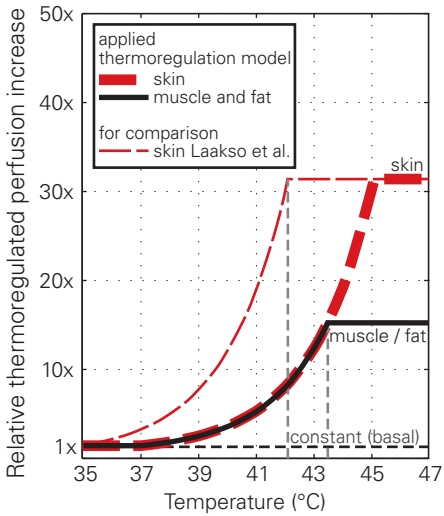

Figure 6.2: Applied temperature-dependent local blood perfusion model for skin, muscle and fat. The Laakso model starts regulating at basal temperature already (around 35°C for skin), while the applied model in this study depends on absolute temperatures. The absolute bloodflow is 106–3392 ml/min/kg for skin, 39–585 ml/min/kg for muscle and 33–495 ml/min/kg in fat.

rate, Q the metabolic heat generation rate and S the spatial specific absorption rate (SAR). The index b indicates a property of blood.

The body-core-temperature was assumed to be fixed with a basal metabolic temperature (T_b) of 37°C, as its elevation is very small compared to local temperature increases [21]. This was confirmed in the thermal validation measurement within this study, where 20 min with 3.6 W/kg wbSAR only induced a rectal core temperature rise of < 0.3 K (compared to local skin temperature increases of almost 5 K), and is also in agreement with observations from hyperthermia [18], where core temperature is usually not exceeding 38°C, even for wbSAR values of up to 10 W/kg. However, small core temperature rises may still have a non-neglectable influence on thermal dose.

A Dirichlet thermal boundary condition was defined at major blood vessels and a convection dependent boundary condition at the interface to external and internal air (h = 6 and 10 W/m2/K, respectively, $T_{Air} = 25$°C), which corresponds to normal breathing and normal clothing with little airflow [52]. Air temperatures of up to 25°C are allowed by the standard without reducing the exposure level [3]. Accurate modeling of the boundary condition is challenging, as part of the patient is lying on a soft table. However, while the boundary to air plays the major role for overall systemic heat dissipation, it has only marginal influence on the local internal peak temperatures. And, as the core temperature was fixed in this study, these boundary conditions had no influence on systemic heat dissipation in the simulations. To confirm these assumptions, the worst-case exposure scenario with Fats was simulated with very aggressive air cooling (60 W/m2/K convection coefficient, additional 600 W/m2 constant heat flux from sweating, and $T_{Air} = 18$°C), corresponding to heavy sweating, fast airflow and increased breathing rate [53]. While the superficial 10 mm tissue layers showed significant temperature decreases (skin surface average from about 35 to 31°C), the extremity hotspots in the wrist and the inner hotspot near the pelvic bone were not influenced. In reality (non-apriori-fixed core temperature), the sweating rate is adjusted to help maintaining a stable core temperature.

The applied PBE model (Eqn. 6.2) does not consider certain aspects, such as the variation of local blood temperature, the discreteness of vasculature and mass transport within vessels or the varying body-core-temperature. A time step of 2.6 s was chosen to maintain

numerical stability in the 2 mm thermal simulation grid (CFL condition for stability). Conformal corrections were used to correct the overestimation of surface heat flux (staircasing effect) in the voxelled FDTD model [54]. As the thermoregulated perfusion models create non-linear temperature increases, values could not be scaled with SAR (i.e. the thermoregulated model requires an individual simulation for each SAR exposure level). The explicit time-domain solver was configured with a lead-time of 30 min (without heating) to reach the baseline steady-state temperature distribution before heating with the maximum allowed exposure level of the first level controlled operating mode (OM) according to [3]. The transient heating reached steady-state after about 20 min for the thermoregulated and 60 min for the constant perfusion model, which is in agreement with time scale observations from, for example, hyperthermia [55]. The modeled instantaneous thermoregulation underestimates the transient temperatures during the heating phase, and overestimates temperatures in the cooling phase, whereas it has marginal influence on steady-state temperatures and reaching time. The cooling phase was not included in the thermal dose evaluations, as peak temperatures drop rapidly after switching off the RF exposure, such that thermal dose (CEM43) does not increase significantly anymore.

6.3.4 Data Evaluation

The electromagnetic exposures were normalized to the maximal limit for the first level controlled OM, i.e. wbSAR: 4 W/kg; head SAR: 3.2 W/kg; and pbSAR: 4–10 W/kg [3]. The local peak temperature (pT) was evaluated for a single voxel, and averaged in volumes of 1 cm^3 (125 voxels) and 10 cm^3 (1250 voxels); thermal dose evaluations were conducted with pT, i.e., exceeding the thermal damage threshold for one tissue-voxel was considered as the limitation. The pTs of all landmark positions (at steady-state) were separately evaluated for tissues with the greatest temperature increases (muscle, skin, fat) and within four body regions (head, trunk, arms, and legs). For the position with the highest relevant steady-state temperature (Fats, pelvis centered), the temperature histogram was extracted for different tissues, and the transient temperature profiles were evaluated and translated to thermal dose (CEM43) for Fats and Duke. Based on tis-

sue damage thresholds, maximum scantimes were derived for the two different blood perfusion models, basal (constant) and thermoregulated perfusion.

6.3.5 Thermal Doses (CEM43) and Damage Threshold Levels

Thermal doses were derived by integrating a temperature-weighted function over time. The most prominent dose model [23] uses cumulative equivalent minutes at 43°C (CEM43) to accumulate temperatures above 39°C and calculates dose-equivalent minutes at 43°C as follows:

$$CEM43(t) = \int_{t_0}^{t_{final}} R^{(43-T(t)} dt \tag{6.3}$$

where t_0 signifies the beginning and t_{final} the end of the heating period. T(t) is the temperature of the tissue of interest at time t, and R is a constant equal to 0.5 for $T(t) > 43$°C, 0.25 for $39° < T(t) < 43$°C, and $R = 0$ for $T(t) < 39$°C. For the tissues primarily heated during MR exposures, the reported thermal thresholds for significant tissue damage were found above 41 CEM43 for muscle, fat and skin, and around CEM43 = 15 min for bone [25, 24]. In more sensitive structures, e.g., the blood brain barrier in the central nervous system (CNS), significant adverse effects were observed at CEM43 = 2 min. Therefore, the following tissue specific CEM43 thresholds have been applied to derive maximum scantimes before running into potential tissue damage:

(A) CEM43 = 15 min, limit for muscle, fat, skin and bone tissue
(B) CEM43 = 2 min, limit for all other tissues

In our study, we utilized pT (single voxel) for $T(t)$. While thermal tissue damage in a few cubic millimeters may be of minor importance for the overall health of a patient, it should still be considered significant, as it could for example cause the loss of neurons when pT occurs at according locations [24].

6.3.6 Experimental Validation

In a first step, the electromagnetic simulations were validated. The simulated B1+ field map of Duke (head imaging position) was compared with an MR scanner B1+ measurement of the actual person the Duke model is based on. The B1+ flip-angle measurement scan was performed in a Philips Achieva 3T, resulting in the absolute B1+ distribution in the head [6]. The simulation was conducted with a generic birdcage with dimensions similar to that of the Philips scanner (16-rung birdcage, 400 mm length). Field levels of the simulation were matched to the experiment by applying the same B1 field around the head as measured with an H-field probe (H3DV7, SPEAG), calibrated for the applied RF sequence.

In a second step, thermal validation measurements were performed within the 64 MHz body coil of the MITS1.5 system (ZMT, Zurich, Switzerland), providing excellent control and ease of access. The physical birdcage geometry was identical to that of the generic model used for all simulations. The upper sternum of another volunteer (32y, male, healthy, 1.88 m) was positioned at the isocenter as the simulations identified anatomically well-defined hotspot positions at the shoulder in this imaging position. A circularly polarized RF field was applied, yielding B1+ values of 3.0 μT and 6.0 μT (assessed with H-field probes, H3DV7, SPEAG), exposing the volunteer with 0.9 W/kg and 3.6 W/kg wbSAR (two consecutive experiments with 60 min recovery time in between). The exposure level was derived from the birdcage power budget and verified by simulations given that Duke and the volunteer have similar anatomical dimensions: height 1.79 vs. 1.88 m; bmi 23.1 vs. 23.7 kg/m2; shoulder length 50 vs. 48 cm; age 34 vs. 32 years. Three highly accurate high-resistance temperature probes (T1V3Lab, SPEAG) were placed at estimated temperature hotspot regions on both shoulders (T1 and T2; see Results section) and in the rectum (T3). Placement uncertainty was about 20 mm. T1 (left shoulder) was thermally isolated with medical compresses, reducing the temperature gradient near the body surface.

The same scenario was simulated with Duke. The convection coefficients on the ambient-air to skin boundary around T1 and T2 were adjusted slightly in order to yield similar initial skin temperatures as in the measurement. Values for T1 (isolated) and T2 (non-isolated)

convection coefficients were 10 and 15 W/m2/K, respectively, compared to 6 W/ m2/K in other simulations, and the background air temperature was 24°C. The thermoregulated perfusion model was applied. For comparison, the variations of the temperature profiles of 400 surface skin voxels (10 × 20 × 2, two surface layers) around the hotspot regions were evaluated. This corresponds to a skin area of 20 mm × 40 mm × 4 mm (about 3.5 g of skin, 2 mm voxel size), accounting for the probe placement uncertainty.

6.4 Results

Figure 6.3 shows the local peak temperatures for Duke and Fats in different landmark positions, normalized to first level controlled OM. The highest relevant temperatures are found in the pelvis imaging position (Z = 80 cm), with values up to 42.8°C for a non-impaired temperature-dependent perfusion model and 60°C for dysfunctional thermoregulation. In leg imaging positions (Z = 104–128 cm), very high B1+ fields are theoretically allowed by the standard ($> 7\ \mu T$) before reaching the partial-body SAR limit, yielding high temperatures. However, none of the MR manufacturers is currently using such high fields in this landmark region, which does not imply that they may not consider this in future systems. The pelvis imaging position is therefore considered the relevant worst-case heating scenario. The upper sternum imaging position was chosen for validation measurements. Ella and Duke show comparable psSAR10g values, but Ella has lower peak temperatures, as the psSAR10g in Ella is located in tissues with higher perfusion. Billie generally has lower values for psSAR10g and temperature (results of Ella and Billie are not depicted).

The short birdcage (Figure 6.3) shows small deviations in SAR and temperature (latter not depicted). Highly exposed regions have very similar absorption patterns (Figure 6.1). The psSAR10g values differ by less than 20% in Fats, peak Temperatures by less than 1 K (constant perfusion) and 0.4 K (thermoregulated). Due to the more localized exposure of the short birdcage, the partial-body SAR limit is reached earlier, such that 4 W/kg wbSAR can only be applied in centered torso positions.

Thermal hotspots occur exclusively in muscle, fat, and skin. The

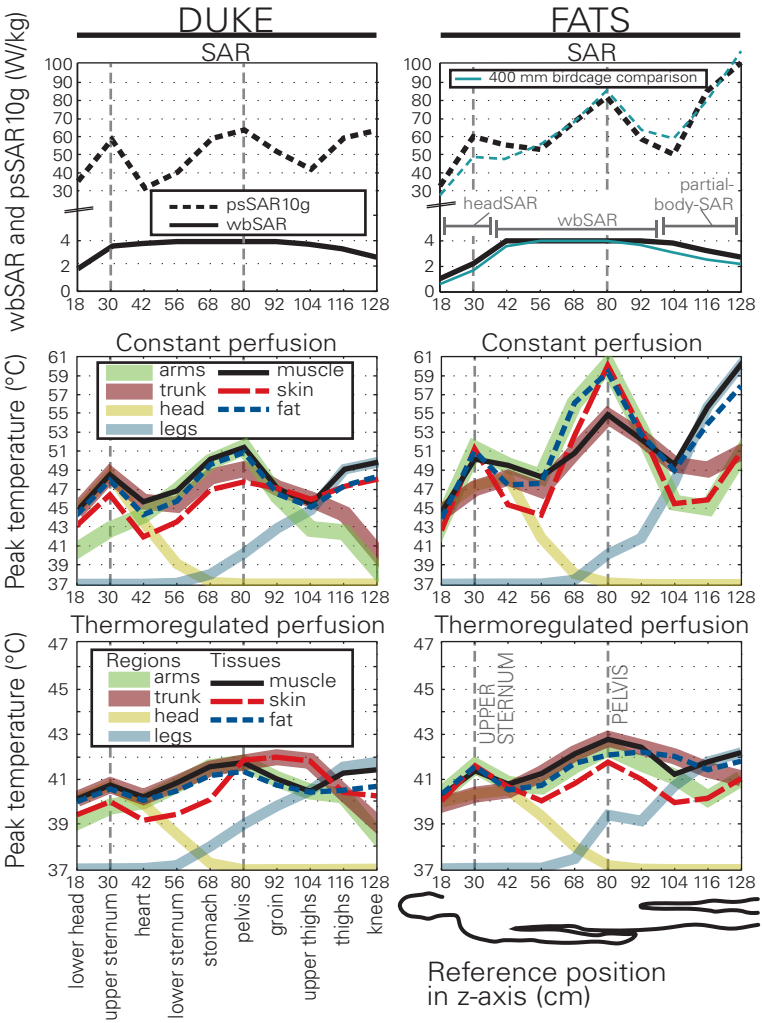

Figure 6.3: psSAR10g, wbSAR, and steady-state peak temperatures (pT) as a function of landmark position for Duke and Fats and for different perfusion models. All exposures are normalized to first level controlled OM (the three different SAR limiting regimes are indicated). SAR values of the shorter 400 mm birdcage are shown for Fats for comparison. Evaluated tissue temperatures are plotted for four body regions and three tissues. Ella and Billie generally show lower temperature values (not depicted).

temperature distribution at steady-state across different tissues and regions of interest for the worst-case position in Fats (pelvis imaging position) is shown in Figure 6.4 . Although bones have lower SAR values, they show high temperature increases because of their low perfusion and proximity to strongly heated tissues. The CNS (including the spinal cord) and all other tissues have significantly lower peak temperatures.

Figure 6.5a illustrates the heating process in the time-domain and the pT of different tissues for the pelvis imaging position of Fats. These transient peak temperatures are accumulated (CEM43) for heating with different wbSAR levels, and the wbSAR is plotted against the scantime of reaching the tissue damage threshold limits (Figure 6.5bc). When applying tissue specific thresholds for Fats (Figure 6.5b), muscle tissue first reaches its damage threshold (CEM43 = 15 min) after 25 min continuous exposure with 4 W/kg wbSAR in the thermoregulated case (indicated with red circles), indicating that muscle would be the most vulnerable tissue according to this approach. At constant perfusion, the threshold limit is reached first by skin tissues, after 4 min. In Duke (Figure 6.5c), the threshold values are reached after 55 min for the thermoregulated model (after 10 min in the non-regulated case). Values for the other models are summarized in Table 6.1. Curves of the thermoregulated model were interpolated, as their non-linear temperature increases cannot be scaled with wbSAR.

The B1+ field distribution derived from the simulation shows good qualitative correspondence to the relative MR flip-angle measurements (Figure 6.6). A statistical comparison, however, is challenging because of the errors due to the coarse measurement grid and various small-scale anatomical structures. In the visualized extraction lines, the B1+ field deviation is less than the combined expanded (k = 2) uncertainty of 2 dB (∼24%, field amplitude).

The thermal validation measurements and the corresponding simulations are within the combined expanded (k = 2) uncertainty of 3.2 dB (∼22%), thus supporting the assumption of high temperature induced perfusion changes, especially when comparing the performance of the thermoregulated model against the constant model (Figure 6.7). The thermoregulation model according to Laakso would underestimate the peak temperatures in our measurement, as the thermoreg-

ulation in skin would start at the basal temperature already. The temperature profiles of the 400 skin voxels were characterized by their mean value, and 65% confidence interval (SD, k=1). The deviation of T2 in Figure 6.7b exceeded one SD, which may result from differences in (a) positioning and (b) posture of the volunteer, (c) baseline perfusion in the low-dose experiment, (d) boundary conditions, and (e) anatomical structure. Figure 6.7c shows the delayed thermoregulatory perfusion change, where the measured temperature suddenly stops increasing after 10 min (it even slightly decreases). The perfusion in the first 10 min is overestimated in the simulation because of the implemented immediate thermoregulation model.

Pelvis	**First level OM** (4 W/kg)			**Realistic OM**[1] (3 W/kg)	**Normal OM** (2 W/kg)	
Model	Regulated	Constant	psSAR10g	Regulated	Regulated	Constant
Fats-120kg	25 min	4 min	81 W/kg	56 min	140 min	9 min
Duke-76kg	55 min	10 min	62 W/kg	170 min	402 min	26 min
Ella-59kg	106 min	11 min	65 W/kg	233 min	> 600 min	28 min
Billie-35kg	290 min	16 min	46 W/kg	560 min	> 600 min	62 min

Table 6.1: Allowed Scantimes and Corresponding psSAR10g Values for Reaching Tissue Specific CEM43 Thresholds

6.5 Numerical Uncertainty

The numerical and measurement uncertainty analysis (Table 6.2) was based on the concept of NIST TN1297 [41]. The thermoregulated temperature increase model and maximum scantime derivation is highly non-linear. The corresponding uncertainty assessment was performed only for the worst-case positioning (pelvis) with the Fats model, and cannot be used for other positions, models, or exposure levels. The influence on our obtained results, i.e., peak temperature and derived maximum scantime, was determined based on the modeling parameter uncertainties from (a) the underlying electromagnetic simulation and (b) the thermal simulation (Table 6.2). The combined root

[1] 3 W/kg wbSAR is assumed to be a realistic maximum exposure in first level controlled OM (averaged over 1 hour), when considering the manufacturer's safety margin and frequent interruptions between sequences.

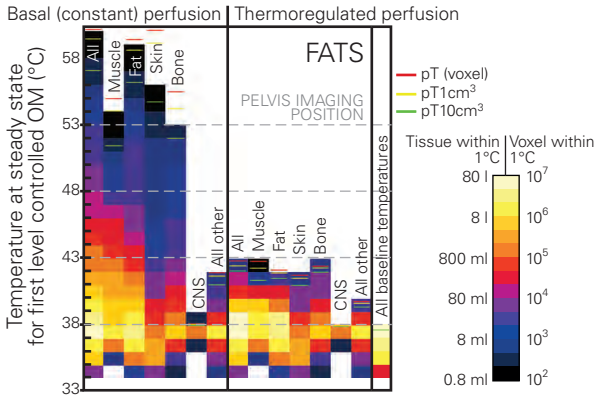

Figure 6.4: Histographic view of the temperature distribution across highly exposed and other tissues of interest for Fats in the pelvis landmark position, wbSAR=4 W/kg (first level controlled OM) and for constant as well as thermoregulated perfusion. Voxel peak temperature (pT), pT1cm^3 and pT10cm^3 are indicated. CNS includes the spinal cord. The baseline temperatures are shown as well (thermal equilibrium before heating onset).

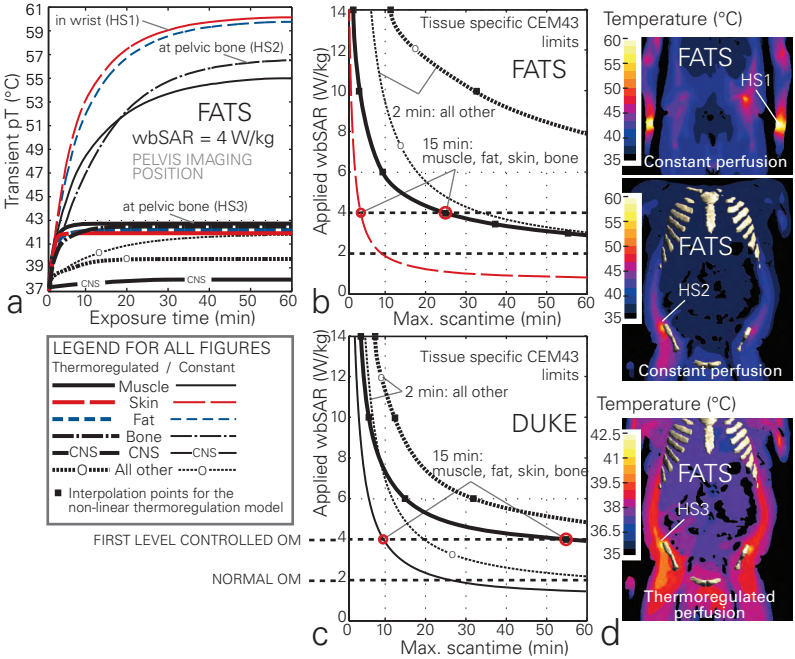

Figure 6.5: a: Transient peak temperature during MR exposure of Fats (all figures are in pelvis imaging position). b: Scan times for Fats to reach the tissue specific CEM43 limits in the context of applied wbSAR exposure levels (at 4 W/kg: muscle tissue first reaches its limit in the thermoregulated case, skin for the constant perfusion; indicated with red circles). c: Corresponding scantimes for Duke. d: temperature distribution in coronal slices showing the different hotspot (HS) locations in Fats (different scales for constant and thermoregulated perfusion).

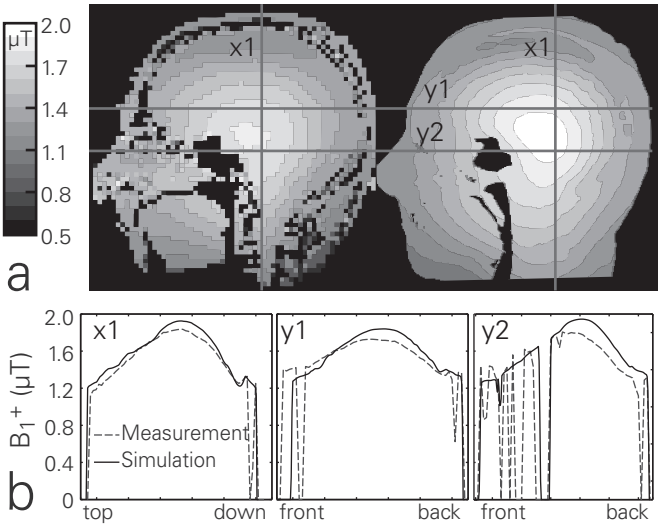

Figure 6.6: B1+ simulation and measurement of Duke and the actual person the Duke model is based on. a: Sagittal view of the simulated (left) and measured (right) B+ field (0.1 μT per contour) and b: three extraction lines (x1, y1, y2) are shown for comparison.

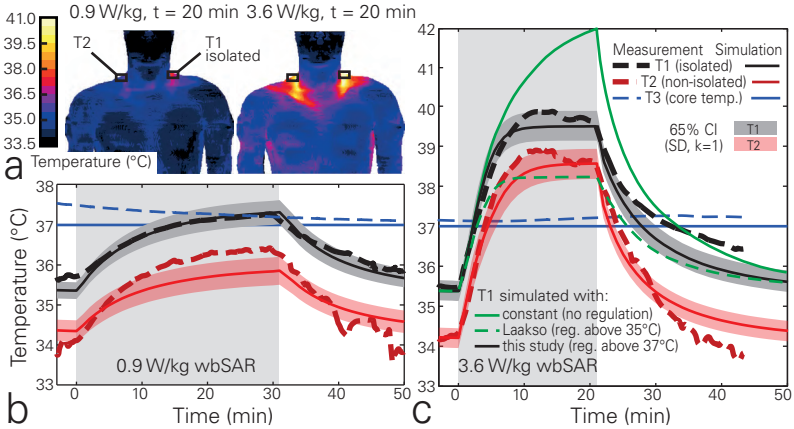

Figure 6.7: a: Numerical prediction of hotspot locations in Duke, b: low- and c: high-dose experiment showing skin surface temperature measurements near the predicted temperature hotspots on the shoulder (T1 thermally isolated, T2 non-isolated) and simulation of the same scenario using the thermoregulation model. The simulation curves are the mean of 400 surface skin voxels and their 65% confidence interval (CI). This estimates the probe placement uncertainty (20 mm) at the high temperature gradient around the hotspot. Core temperature remained stable during the experiments. Thermoregulation starts above 37°C, except for the Laakso model. Constant perfusion and the Laakso thermoregulation model show considerable deviation to our measurement results in skin.

sum squared uncertainty (RSS, single standard deviations, k = 1) is estimated to be 0.51 dB (∼12%) for the local SAR enhancement (psSAR10g normalized to wbSAR) and 1.28 dB (∼30%) for peak temperature increase with constant perfusion (both in agreement with [39], i.e. 11% and 31%). The uncertainty for peak temperature increase in the thermoregulated case is lower (0.9 dB, ∼21%), as the modeled perfusion increase suppresses the variation (non-linear suppression). As the CEM43 dose accumulation increases by factor 4 with each additional degree Celsius above 39°C (factor 2 above 43°C, Equation 6.3), uncertainty for thermal dose is non-linear for both perfusion models. The derived maximum scantimes before reaching the dose limit have estimated uncertainty values of 1.2 dB (∼27%, constant perfusion) and 2.1dB (∼50%, thermoregulated). The measurement uncertainties for B1+ and temperature are 0.9 dB and 1.4 dB, respectively (see Table 6.2cd).

6.6 Discussion & Conclusion

Temperature-regulated perfusion significantly lowers the maximum temperature increase compared to static perfusion values. At the first level controlled OM, it is about a factor 3–4 (from 8–23 K down to 3–6 K) depending on the model and position (Figure 6.3). The thermoregulated perfusion is therefore the most influential parameter for local temperature increase and related damage for the given exposure scenarios. Other factors, such as sweating, airflow, or room temperature, result in altered skin temperatures but have little influence on local internal peak temperatures. Body core temperature is considered fixed at 37°C, which was confirmed by the validation measurement and experience in hyperthermia, and thus also has a minor influence on local temperatures. The peak temperature increases in hyperthermia are similar for comparable SAR levels, but a direct comparison is difficult due to the intrinsic difference of exposure, i.e., focused absorption versus B1+ homogeneity optimization.

In summary, the maximum scantimes of Table 6.1 (partially de-

[1] Relative local SAR uncertainty, as exposure is normalized to wbSAR.

[2] Highly non-linear model. Values only valid for this specific worst-case (Fats, pelvis position, first level OM)

Parameter	Range	u_i	
(a) EM Simulation		psSAR10g per wbSAR[1]	
Convergence	Sim. length: +100%	0.03 dB	
Model discretization	Voxel size: 0.5, 3 mm	0.26 dB	
Dielectric parameter	σ : ± 10% (all tissues)	0.05 dB	
Dielectric parameter	ε : ± 10% (all tissues)	0.17 dB	
Dielectric contrast	σ : ± 10% (single tissue)	0.09 dB	
Dielectric contrast	ε : ± 10% (single tissue)	0.08 dB	
Density contrast	ρ : ± 10% (single tissue)	0.26 dB	
Segmentation errors	Quality of models [39]	0.28 dB	
RSS: SAR uncertainty		**0.51 dB**	
		[−11%;+12%]	
(b) Thermal Simulation		pT, Thermoreg.	pT, Constant
Local SAR uncertainty	from (a)	0.40 dB[2]	0.40 dB
Convergence	Sin. length / timestep	0.04 dB[2]	0.05 dB
Model discretization	Voxel size: 0.5, 3 mm	0.19 dB[2]	0.26 dB
Thermal parameter	c : ± 10% (all tissues)	0.00 dB[2]	0.00 dB
Thermal parameter	k : ± 10% (all tissues)	0.05 dB[2]	0.26 dB
Thermal parameter	Q : ± 10% (single tissue)	0.08 dB[2]	0.02 dB
Blood heat capacity	$\rho_b \cdot c_b$: ± 10%	0.16 dB[2]	0.16 dB
Thermal boundary cond.	h : ± 50%	0.12 dB[2]	0.11 dB
Basal (constant) perf.	B_0 : ± 50%	0.26 dB[2]	1.14 dB
Perf. increase	L_b : ± 50%	0.70 dB[2]	n.a.
RSS: Peak temperature increase uncertainty		**0.90 dB[2]**	**1.28 dB**
actual estimated peak temperature		42.8°C	60°C
uncertainty interval in peak temperature		[41.7°; 44.1°]	[54.1°; 67.9°]
Corresponding max. scan time uncertainty		**2.1 dB[2]**	**1.2 dB[2]**
actual estimated value		25 min	4 min
uncertainty interval		[16; 41 min]	[3; 5.3 min]
(c) B1+ validation measurement			
Assessment of relative B1+ map [28]		0.6 dB	
B-field probe uncertainty for B1+ measurement		0.6 dB	
Age induced changes (6 years between model segmentation and B1+ mapping, from [39])		0.3 dB	
Head positioning in scanner		0.1 dB	RSS (a) + (c)
RSS: B1+ measurement uncertainty		**0.9 dB**	1.0 dB (k=1)
uncertainty interval in peak temperature		[−18; +22%]	2.0 dB (k=2)
(d) Temperature increase validation measurement			
(assessment for T1 at high dose experiment)			
Temperature probe uncertainty		< 0.1 dB	
Incidence B1 field assessment		0.6 dB	
Probe placement (20 mm)		1.0 dB	
Probe thermal contact		0.5 dB	
Volunteer positioning (100mm)		0.3 dB	
Differences between Duke and the actual volunteer		0.3 dB	
Thermal equilibration		0.5 dB	
RSS: B1+ measurement uncertainty		**1.4 dB**	RSS (b) + (d)
actual estimated temperature		39.5°C	1.6 dB (k=1)
uncertainty interval		[38.8°; 40.5°]	3.2 dB (k=2)

Table 6.2: Standard combined uncertainties for (a,b) the numerical evaluations (Fats in pelvis position), (c) the B1+ assessment, and (d) thermal measurements (Duke/volunteer in upper sternum position). Stated uncertainty values are standard deviations (k = 1) in the assumed log-normal probability distribution. Since they are uncorrelated, they can be combined by root-sum-square (RSS) procedures.

rived from Figure 6.5) have been estimated in the identified worst-case position (pelvis imaging) for the investigated models. The Fats model reaches the damage threshold limits first in all configurations. At first glance, the history of safe use of whole-body MR coils seems to contradict the presented thermal dose estimations as the current safety guidelines accept exposures in the first level controlled OM for 60 minutes [3]. However, actual clinical use shows that:

1. The IEC standard is very rarely fully exploited:
   (a) exposure is frequently interrupted (different sequences), leading to lower average SAR
   (b) the vast majority of scans is believed to be shorter than 30min
   (c) the manufacturers' safety margins lead to an effective wb-SAR of presumably about 2.7–3.7 W/kg instead of the allowed 4 W/kg.
2. As most patients are awake during MR scans, they may provide direct feedback on excessive heat sensations to the operator. However, some tissue may have limited heat sensation (e.g. muscle [19]).
3. The actual thermal tissue damage thresholds in human might actually be higher than the ones used for this study.
4. The peak temperature is reached in only a few cubic millimeters of tissue (pT). The average temperature of the hottest 1 g of tissue is 0.5–1.0°C lower in the thermoregulated case (pT1cm3, Fig. 4), which would corresponds to factor 2?4 longer acceptable scantimes. It remains unclear whether exceeding damage thresholds in less than 1g of tissue could be acceptable in some tissues.

Therefore, the results of this study may well correspond with the history of safe use. All investigated human models accept roughly one

hour exposure to a realistic average wbSAR of 3 W/kg (Table 6.1). On the other hand, the study also demonstrates that the guideline limit for local tissue temperatures (40°C, [3]) is exceeded in all positions for Fats and Duke in the first level controlled OM. Therefore, the current safety guidelines should be revised. A new concept could be based on the thermal dose model (CEM43) in conjunction with tissue-specific thresholds. Such an implementation may be challenging due to the complex thermal parameter space. Especially the high sensitivity of CEM43 below 43°C causes systematic problems, where a difference of only 1°C leads to factor of 4 change in allowed scantimes. Nevertheless, we believe that having a better surrogate for actual tissue damage with larger uncertainty may become more useful in the future than wbSAR and local SAR limitations which have very limited correlation to tissue temperature and tissue damage. More research on local thermoregulatory and tissue damage processes is therefore of high importance. The investigated dose model also allows considering transient temperatures and tissue sensitivity.

The presented results indicate that the greatest health risk from MR RF exposure can arise from a combination of (a) high exposure levels (i.e., first level controlled OM), (b) long scantimes, (c) anatomically large and obese patients, and (d) patients with disabled or partially dysfunctional perfusion abilities (e.g. the elderly, diabetics) or heat sensation (e.g., paraplegics, [56]). As patients with impaired or dysfunctional thermoregulation abilities might require special considerations, it is important to derive sound tissue damage thresholds and better thermoregulation modeling capabilities, based on accurate perfusion rates for the entire patient population.

In clinical practice, a different type of tissue damage mechanism is currently observed: High, very locally induced electric fields can lead to immediate burns. In many of these cases, the limbs or other body parts of the patients were in direct contact with RF coils or skin-to-skin contact points and loops were suspected to be responsible for these injuries [57]. Other investigations are needed to understand how to assess these burns due to high induced electric fields, where thermoregulation is absent due to their acute nature.

6.7 Acknowledgements

This study was supported by the EUREKA (E!4144) and CTI (9193.1) project MRI+.

Chapter 7

Outlook

7.1 Future Concepts for MRI Safety Standards

Regarding RF exposures, current MRI safety standards [3] are based mainly on whole-body SAR, head SAR and partial-body SAR. The local SAR (psSAR10g) is limited only for local transmit coils, but not for body coils. Limitations only rudimentarily include exposure time (via overall energy limit), and do not consider any transient heating processes. These guidelines aim to limit whole-body thermal stress and local temperatures to acceptable levels. The approach is opportunistic, as averaged SAR can be determined with high accuracy. However, recent studies have shown that the intended upper-bound temperatures may be exceeded, even when complying with the suggested operating modes [34, 45].

By analogy driving speed is currently limited by engine power rather than by speedometer. But speed is the source of danger in driving and engine power is a poor surrogate for speed as a means to limit danger. In initial acceleration, a larger motor may even be desirable, given that the speed limit will not be exceeded. Likewise, a surrogate for adverse health effects should be as close as possible to the actual damage mechanism – even when it comes with higher uncertainty intervals. Future safety concepts should thus be based

on thermal dose (e.g., CEM43) in conjunction with damage threshold limits, which is the most accurate proxy for tissue damage. This basic concept, which is elaborated in Chapter 6, would allow higher initial RF exposures and potentially shorten scan times for most patients, while simultaneously improving safety. The concept is visualized in Figure 7.1.

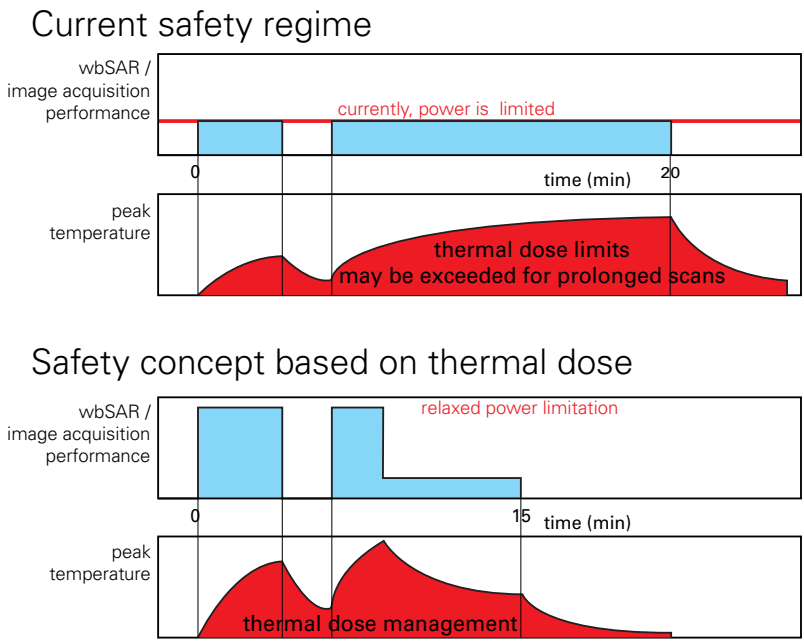

Figure 7.1: Schematic of the current safety regime (wbSAR limited), and a concept based on thermal dose management, which may allow higher performance.

7.2 Compliance with Thermal (Dose) Based Safety Standards.

In the current safety standard [3] as described in Chapter 2.5, coil power must be limited so as not to exceed certain (1) wbSAR, (2) headSAR, and (3) partial-body (pb)SAR levels. The wbSAR can be assessed straightforwardly via the overall power budget of the coil, divided by the patient mass. For headSAR and pbSAR, manufacturers must implement dedicated algorithms that estimate the respective exposures from patient anatomy (height, weight) and imaging position.

Additional (or alternative) steps are required to show compliance with a thermal-dose-based standard. Recent studies refined the thermal simulation model [46], included human thermoregulation [34], and investigated specifically vulnerable groups such as pregnant women [42, 58, 59] or patients with impaired thermoregulation [45]. However, there is great uncertainty associated with temperature increase and thermoregulation in humans. Additional studies in these fields are needed for a broad acceptance of a thermal-dose-based standard, by further reducing uncertainties and including inter-subject variations.

Practical implementation of a thermal-dose standard would require management of the exposure levels throughout the scan sequences and would also have to ensure that, e.g., the same patient is not scanned twice without taking thermal dose history into account.

Because of these theoretical and practical implications, many MRI safety experts do not yet feel comfortable with a transition from SAR-based limitation regimes to thermal-dose-based standards.

7.2.1 Pre-Scan Evaluation Methods

When evaluating the planned scan sequences for their exposure safety, the estimation of a transient "virtual peak temperature" (VPT) may lead to an appropriate thermal dose management. The VPT of the patient is estimated from the planned sequences with their corresponding SAR levels. Thermal dose as CEM43 is accumulated for the whole procedure, and the scan is stopped after a defined threshold limit is reached (Figure 7.2). The corresponding functions to estimate the

peak temperatures are determined by means of anatomical models, with the option to link the patient to a anatomically similar virtual model.

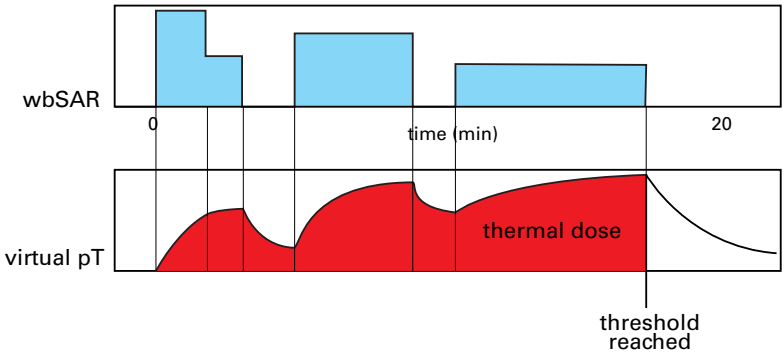

Figure 7.2: Schematic of the VPT estimation during a planned MRI scan.

7.2.2 On-The-Fly Estimations

To overcome the differences between the patient and the available anatomical models, one could perform simulations with the current patient's anatomy. By running a pre-scan, sufficient information is gathered for the segmentation, and the SAR simulations are performed together with the scan onset. This scenario is unlikely to be applied in near future, as accurate segmentation of a patient currently takes several months. EM and thermal simulations, on the other side, could be performed within a few minutes in the near future.

7.2.3 On-The-Fly Monitoring, MRI Thermometry

As an alternative to SAR and temperature simulations, online monitoring of the thermal dose could be achieved with MRI thermometry, which utilizes the proton resonance frequency shift (PRFS) [29] to assess absolute tissue temperatures directly via the scanner. The

quality and accuracy of MRI thermometry is increasing continuously. Uncertainties in the range of 1°C would already allow a beneficial monitoring of hotspot areas. A monitoring thermometry scan could be performed, e.g., every 6 min, and identified hotspot areas could be monitored even more frequently. There are still issues to resolve, as MRI thermometry has limited functionality in some tissues (e.g., fat), is susceptible to motion artifacts, and the hotspot may actually occur outside the current field of view (FOV) of the scanner.

7.3 Challenges in Parallel Transmit MRI

Emerging scanner technologies – such as parallel transmit (pTx) – increase the need for dedicated safety assessment in the new environment [14, 44, 60]. The current safety regimes in MRI are widely based on quadrature driven coils, with a remarkable history of safe use during the past 30 years. The application of the RF energy with fixed amplitudes and phase shifts, or only limited deviations as in RF shimming, leads to very defined absorption distributions within the patient's body, which always scales with the wbSAR exposure. Emerging scanner technology will be based on parallel transmit (pTx) coil designs with many degrees of freedom, as the amplitude and phase of each rung (in a birdcage) can be adjusted individually. pTx allows the B1+ field to be focused on a desired location within the body, and a wide range of novel applications are believed to be in development. In addition to static multiport RF shimming, where the same pulse shape — with different amplitudes and phases — is delivered to all ports, dynamic RF shimming excites each port with a different pulse shape. This allows an even more customized and time-varying B1+ distribution, while the parameter space for excitation schemes gets exuberant. This makes safety assessment challenging, as not all of the divergent excitations can be covered in the evaluations. A worst-case evaluation for the entire parameter space would presumably result in overly conservative restrictions. However, the effect of constructive interference of the parallel transmitting ports should not be underestimated [14].

7.4 Challenges in High Field MRI

The evolving field strengths of the static magnet (currently 9 T and beyond) lead to higher RF frequencies (ca. 42 MHz per Tesla; up to 500 MHz in high-field MRI). At the same time, dynamic techniques, such as RF shimming and pTx, are more benign, by minimizing $B1^+$ non-uniformity caused by the smaller wavelengths and subsequent phase delays inside the body. Besides the challenges in safety assessment of pTx systems (Chapter 7.3), the higher RF frequency shows less uniform exposures and has the potential to form more localized hotspots. The resulting SAR distributions must be assessed for undesired hotspots to be prevented [61].

Part II

Exposure Assessment in Human for Health Risk Research

Chapter 8

Background in Human RF Provocation Studies

8.1 Motivation and Objectives

There is increasing evidence that pulse-modulated radio frequency electromagnetic fields (RF-EMF), such as those emitted by mobile phones, can alter brain physiology [62, 63, 64, 65, 66, 67, 68, 69]. The reported effects include changes in EEG, regional cerebral blood flow (rCBF), sleep architecture, brain glucose metabolism, sleep-dependent performance improvement, and cognitive functions. However, conclusions about possible adverse effects on human health are premature, as the underlying mechanisms are as yet unknown. Additional studies are needed to define the critical field parameters, e.g., amplitude modulation or field distribution, to eventually identify a physiological interaction mechanism.

Besides epidemiological, *in vitro*, and *in vivo* studies, potential EMF effects need to be assessed in human provocation studies. Although this means that guideline limits generally cannot be exceeded, there is no alternative for assessing immediate effects on humans. Study endpoints range from head imaging modalities like positron emission tomography (PET) [69] and near infrared imaging (NIRI) [70], via sleep and wake electroencephalography (EEG), to cognitive

tasks, subjective well-being [71], and hormone production (e.g. melatonin) [72].

Objectives with respect to this thesis are to provide high-quality EMF exposure equipment and to investigate effects, e.g., RF related noises, that may compromise the blinded protocol or the non-thermal nature of the findings.

8.2 Mobile Phone Exposure

Nowadays, exposure to electromagnetic fields in the MHz region is omnipresent. Exposures to broadcasting services such as AM radio (around 1 MHz), FM radio (100 MHz), and television (50–950 MHz) have been around for decades. Mobile phone and data communication has grown exponentially in the last 20 years, with anticipated saturation within the next few years, as the number of mobile phone subscribers is approaching the size of the entire human population. The older generation GSM/DCS/2G phones (900 and 1800 MHz) are being replaced with UMTS/3G (1950 MHz), but phones retain backwards compatibility so far. For short-distance communication, the cordless landline phone (DECT, 1880 MHz), WLAN, and Bluetooth (2400 MHz) are predominant. Emerging technologies such as LTE operate multiple bands between 800 and 2600 MHz.

Since EMF power levels decrease dramatically with distance ($1/r^2$), the downlink communication — from the base station to the mobile device — generally results in very low exposure levels, with small variations during daytime. The opposite is the case for the uplink connection, where the mobile device emits in close proximity, but mainly when the services are actually being used. Figure 8.1 gives a qualitative overview on typical exposure levels and times and visualizes the resulting total absorbed energy (dose). Due to the poorly implemented power control, the highest exposure levels today originate from GSM/2G mobile phones, exceeding the typical mean output power of 3G/UMTS by about a factor of 100 [73]. When considering the dose, the DECT base station emits high levels as well, as the standard DECT protocol has no power control implemented, and the base station is located relatively nearby. The exposure level in MRI scanners can be hundred times higher than with GSM phones. Exposure

time, however, is very small when averaged over prolonged periods.

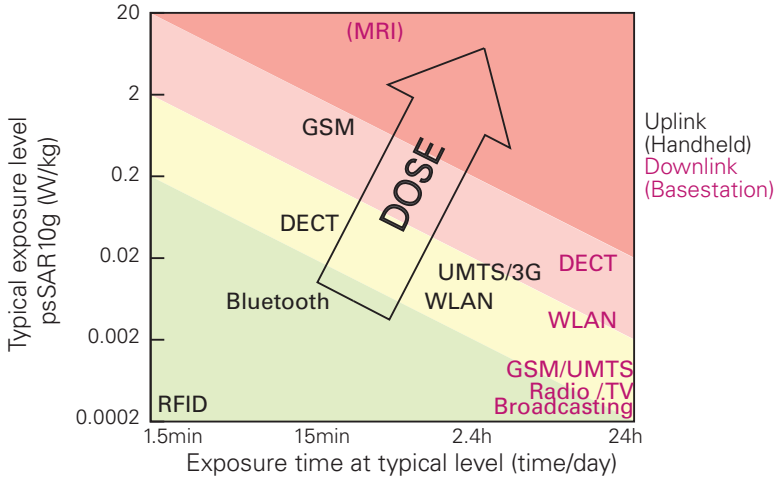

Figure 8.1: Qualitative illustration of exposure levels typically reached as a function of the corresponding exposure times. Exposure dose (total absorbed energy) is the product of exposure level and time. Dose is generally not limited. MRI is inserted for comparison; a typical scan lasts about 20 min.

Exposure of the general public is limited in terms of exposure level, but not in terms of exposure time and dose [1]. The ICNIRP guidelines, which are adopted as written by most countries, define an upper limit for the general public of 2 W/kg psSAR10g and 0.08 W/kg wbSAR (for explanation of the averaging algorithms see Chapter 2.4).

8.3 Non-Thermal Effects

Exposures in compliance with the ICNIRP guideline limit for the general public, i.e., < 2 W/kg psSAR10g, result in temperature increases below 0.3°C in the brain and 0.6°C in the whole head [74]. Possible effects of, e.g., mobile phone radiation are therefore referred to as "non-thermal", i.e., the actual temperature elevation is believed not

to be perceived and not to measurably influence cognitive functions. In contrast to MRI exposure, thermoregulation is not initiated and does not have any influence on the small temperature increase [21].

Nevertheless, the thermoplastic expansion of pulsed EMF fields may still be non-neglectable. For very high pulses, the well-established effect of microwave hearing [75] leads to a conscious perception of an acoustic signal, with an involved temperature ripple of less than 10^{-6} K. Potential perception of any kind of microwave hearing was usually suppressed in human studies by introducing an environmental background noise. Whether thermoplastic expansion could account for other non-acoustic perceptions is not known.

However, there is an increasingly large body of evidence for non-thermal effects of modulated EMF on the central nervous system (CNS) in humans, but still little is known about the underlying mechanism or whether these effects may cause adverse health consequences. The following sections contain a selection of results from recent sleep studies. The exposure system described in Chapter 9 has been designed to further investigate CNS responses in hypotheses-driven research. In most studies, electroencephalography (EEG) or positron emission tomography (PET) was used to detect effects on the CNS.

8.3.1 Effect on EEG Spectral Power

Borbely et al. [62] exposed 24 young males to an intermittent radiation schedule (900 MHz, GSM-modulation, 1 W/kg psSAR10g, 15-min ON / 15-min OFF) for an entire night's sleep episode. Besides some small effects on the amount of waking after sleep onset, they found an EEG spectral power increase in the non-rapid-eye-movement (REM) sleep period. The maximum rise occurred in the 10 – 11 Hz and 13.5 – 14 Hz bands (Figure 8.2).

A replication study [63] on these effects was performed in 2000, but with a new setup for unilateral exposure of the brain, the system precedent to the one described in Chapter 9. The main objective was to minimize the uncertainties regarding the head position during sleep in the former study. 16 subjects were exposed either in the left, the right, or neither of the hemispheres for 30 min prior to a 3-h daytime sleep episode (900 MHz, GSM-modulation, 1 W/kg psSAR10g). Again, a maximum rise in the spectral power in the 9.75 – 11.25 Hz

and 12.5 – 13.25 Hz band was found during the initial phase of sleep. The unilateral exposure during waking induced no hemispheric asymmetry of the EEG power during sleep (Figure 8.3).

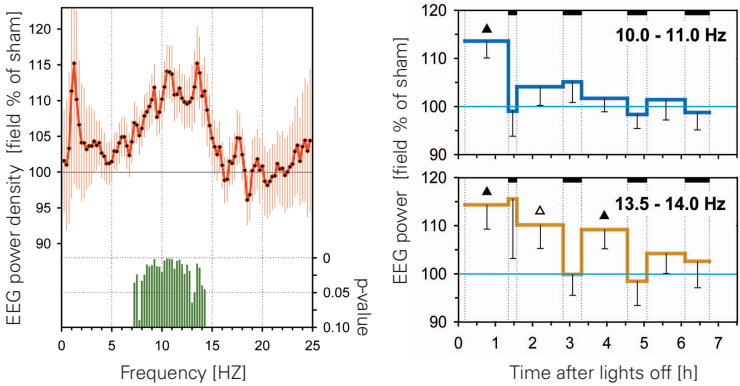

Figure 8.2: EMF exposure during sleep and enhanced spectral power of nonREM sleep EEG in the 7 – 14 HZ range during initial phase of sleep

To establish a dose-response relationship, the influence of EMF exposure was investigated by varying the signal intensity [64]. The head of 15 healthy male subjects was unilaterally exposed for 30 min prior to sleep (900 MHz, GSM-modulation, 0.2 and 5 W/kg psSAR10g). Sleep architecture was not affected by EMF exposure. Analysis of the sleep EEG revealed a dose-dependent increase of power in the spindle frequency range in non-REM sleep (Figure 8.4). This study is the first to reveal indications of a dose-response relationship due to EMF field intensity.

Similar effects were reported in a more recent study [65], also with 14 Hz modulation instead of the 217 Hz used with GSM signals. There is also indication that low-frequency magnetic field exposure may have comparable effects, and that a broader range of EEG frequencies may be affected [66]. Increased sensitivity in adolescents was not observed [67].

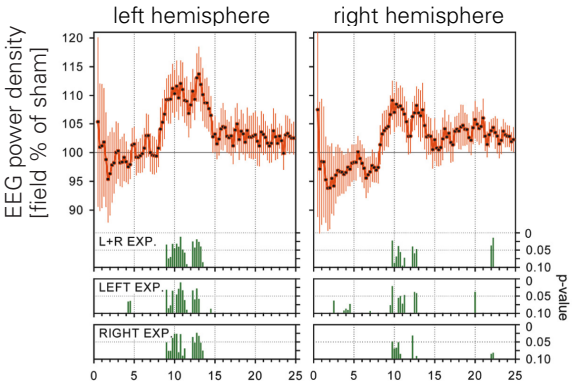

Figure 8.3: EMF exposure during waking prior to sleep affected spectral power of nonREM sleep EEG during the initial phase of sleep. Unihemispheric exposure did not result in hemispheric asymmetry.

8.3.2 Effect on Sleep-Dependent Performance Improvement

Another recent study [76] explores possible mechanisms of how radiofrequency electromagnetic fields (RF EMF) affect cortical activity during sleep and impact sleep-dependent performance changes. Sixteen male subjects were trained in a motor task to be used to assess changes in overnight performance improvement before exposure overnight to pulsed RF EMF. Each 500 ms RF EMF burst was comprised of 7×7.1 ms pulses, each with a peak spatial specific absorption rate averaged over 10 g (psSAR10g) of 10 W/kg, at a burst repetition rate of 0.25 – 0.8 Hz, resulting in an average whole-night psSAR10g of 0.15 W/kg. Electroencephalograms (EEG) were recorded in parallel during the entire sleep period. The slow-wave activity (SWA, 0.75 – 4.5 Hz) increased towards the end of the sleep period and also after the RF EMF bursts in event-related EEG spectral power and phase changes. Sleep-dependent performance improvement after overnight RF EMF exposure was significantly reduced (–20%, P = 0.03) compared to the sham overnight treatment. The changes in the time

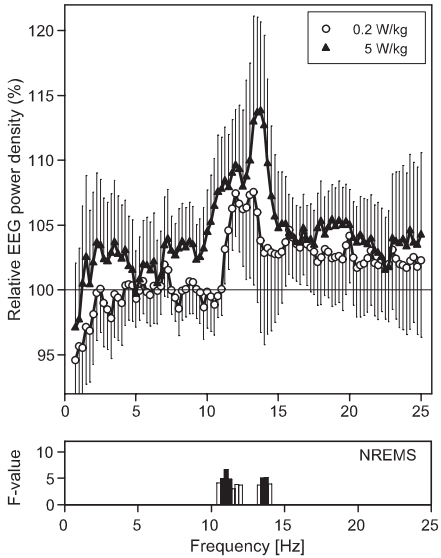

Figure 8.4: Dose-dependent effect of RF EMF exposure on EEG power spectra in non-REM sleep. Relative EEG power density spectra (100% = sham) are illustrated. Three conditions were applied: sham, 0.2 and 5 W/kg RF EMF exposure (10 g-averaged peak spatial SAR).

course of the SWA during overnight exposure may reflect an interaction of RF EMF with the renormalization of cortical excitability during sleep. Overnight exposure to pulsed RF EMF appears to negatively impact sleep-dependent performance improvement.

8.4 Hypothesized Interaction Mechanisms

Several experimental artifact confounders have been suspected to be responsible for observed effects. For example, the presence of the metallic EEG electrodes were believed to cause strongly enhanced induced fields due to the coupling of the incident fields with the elec-

trode assembly, or the subsequent temperature increase at the tip of the electrodes was speculated be responsible for the EEG spectral power enhancements. These confounding effects have been discussed in Chapter 10 and are believed unlikely to explain the observed effects.

As observation of a robust effect currently remains elusive, the proposed interaction mechanisms remain vague. Oscillatory brain activity caused by sensory perception of RF EMF, or non-synaptic or ephaptic coupling of cortical neurons have been suggested as potential mediators [76]. The nature of the findings generally seem to point towards a non-thermal effect [77].

Chapter 9

Flexible Human Exposure System for Hypothesis Driven EMF Research

9.1 Abstract

[1]A novel exposure system for double-blind human electromagnetic (EM) provocation studies has been developed that satisfies the precision, control of fields and potential artifacts, and provides the flexibility to investigate the response of hypotheses-driven EM field exposure schemes on brain function ranging from extremely low frequencies (ELF) to radio frequency (RF) fields. Among the many special features, it can provide the same exposure of the lateral cerebral cortex at two different RF frequencies (900 MHz and 2140 MHz), but with different exposure levels at subcortical structures, and in addition allows for uniform ELF magnetic field exposure of the brain. The RF modulation and the ELF signal are obtained by a freely programmable arbitrary signal generator allowing a wide range of worst-case exposure

[1]This Chapter has been published in [78].

scenarios to be simulated, including those caused by wireless devices. RF pulses with more than 60 W/kg peak spatial specific absorption rate averaged over 10 g tissue (psSAR10g) can be reached, allowing high peak-to-average ratios of >30 at the exposure limit of 2 W/kg psSAR10g. Assessed SAR efficiencies are 0.50 W/kg (900 MHz) and 0.39 W/kg (2140 MHz) per 1 W forward power. The ELF magnetic field exposure of the brain has a deviation from uniformity of 8% (standard deviation) and the achievable maximum amplitudes are 800 A/m at 50 Hz and 140 A/m at 1 kHz. A rigorous dosimetric assessment has been performed for various different brain tissues and structures.

9.2 Introduction

Previous research has shown that pulse-modulated radiofrequency (RF) electromagnetic fields (EMF) approximating the exposure from mobile phones affect the waking and sleep electroencephalogram (EEG) [79, 80, 81, 68, 82, 65] when applying 30 min EMF exposure prior to sleep and to waking EEG recording. Significant effects have been observed for pulse-modulated exposures below peak spatial specific absorption rates (psSAR) of 2 W/kg (whole head), where the brain and skin temperature increase is estimated to be about 0.14 K and 0.4 K and remains below 0.25 K and 0.6 K [83, 74, 84]. No effects were observed when continuous wave (CW) fields with identical psSAR values were applied [81, 82]. In addition, effects on regional cerebral bloodflow [81, 85] and more recently on brain glucose metabolism have been reported [69].

9.3 Objectives

The objective of this study is to develop an advanced exposure system to empower researchers to investigate a number of hypotheses derived from the above-mentioned body of experimental evidence. Specifically, this includes the hypotheses that biological responses to RF exposure depend on the modulation frequency or time-domain characteristics of the modulation, peak-to-average ratios (PAR), intermittency, exposed functional subregions of the central nervous system

(CNS) (e.g., cortex versus subcortical brain regions), and combined RF and extremely low frequency (ELF) magnetic field exposures. The developed system has to comply with the minimal requirements of reproducibility [86], while also providing additional detailed information of the applied worst-case exposure scenario, including evaluation of various functional subregions of the brain. A comparison to actual mobile phone exposure patterns can be found elsewhere [87].

9.4 Methods

The exposure system is based on planar patch antennas, which are used for the carrier frequencies of 900 MHz and 2140 MHz (SPA860/65/9/0/V and SPA2000/80/8/0/V, Huber+Suhner, Herisau, Switzerland), and fixed on low-reflecting, low-loss stands (wood) at a height of 130 cm from the floor. Either the 900 MHz or the 2140 MHz antenna is assembled inside a box of low dielectric material ($\varepsilon_r = 2.5$, $\sigma < 0.15$ mS/m), surrounded by Helmholtz-like coils for ELF exposure (Fig. 9.1). The subjects sit on a height adjustable seat with their head supported by styrofoam mounts such that the ear canal is situated horizontally at the center and vertically 42 mm below the center of the antenna patch. The distance between the antenna and the head is 110 mm (900 MHz) and 180 mm (2140 MHz).

The ELF exposure is realized using two Helmholtz-like coils on each side of the head. Although their rectangular shape (330 mm x 390 mm) and higher separation distance (257±20 mm depending on the subject's anatomy) is different from the original Helmholtz design, sufficient homogeneity of the magnetic field is achieved. The ear canal is 82 mm below the center line between the coils. Electric current through the dual winding (2 x 23 windings per coil) is either parallel or anti-parallel for ELF exposure and sham exposure, respectively. The coils are powered by a voltage controlled current source (VCCS, SPEAG, Zurich, Switzerland). The two separate installations for RF 900 MHz and RF 2140 MHz (both enhanced with ELF exposure) are not visually distinguishable as the antennas or coils are assembled within the low-loss enclosures (Fig 9.1). The signal for the RF modulation envelope and the ELF magnetic field is generated by an arbitrary function generator (Agilent 33220A, Agi-

lent Technologies, Santa Clara, CA), allowing any 14-bit, 50 MSa/s, 64 k-point waveform. An RF generator is used for modulations up to 50 kHz (R&S SML02, Rohde&Schwarz, Munich, Germany). The ELF current source allows frequency components up to 1.3 kHz, which is sufficient to simulate the main ELF components generated by the currents in mobile phones [88].

The whole system is computer controlled and monitored using a custom-made software package written in C++. The applied RF power is controlled via bi-directional couplers and calibrated Schottky diodes. A set of randomized exposure conditions can be defined to allow a fully double-blind protocol. Since exposure safety is especially important in human experimental test systems with high peak SAR values, forward and reflected power is continuously monitored, controlled and logged (10 s sampling). The system aborts immediately if the expected forward power is exceeded by more than 10%. A watch-dog safety hardware circuit prevents exposure in case of a software failure, and RF amplifiers operate 1 dB below their maximum output power. To inhibit any potential acoustic perception of vibration by the patch antenna driven with high peak-to-average power, a low brown noise (spectral density proportional to 1/f2) is added when necessary, using a loud speaker [65]. Type-A weighted average sound pressure levels are estimated to be <35dB without noise (below the threshold of the device) and 43±2 dB with applied brown noise at the position of the subject's head, assessed using the RO-1350A (Roline/ROTRONIK, IEC-651 standard, Bassersdorf, Switzerland) sound level meter.

Numerical dosimetry and optimization was conducted with the simulation platform jointly developed by the IT'IS Foundation and SPEAG (Zurich), and which has been commercialized by the latter (SEMCAD X, V13.4). The finite difference time domain (FDTD) solver was applied for the RF analysis in combination with the SEMCAD extension for the analysis of exposure levels at functional subregions of the brain (1105 regions in the Talairach-space) [89]. The reference and uncertainty analysis was performed with the 26-year-old female 'Ella' from the Virtual Family [35] (www.itis.ethz.ch/vip). The dielectric tissue properties have been assigned according to literature values [17] that have recently been updated [16]. The grid resolution had a minimal voxel size of 0.2 mm (x, y, z direction) in the patch

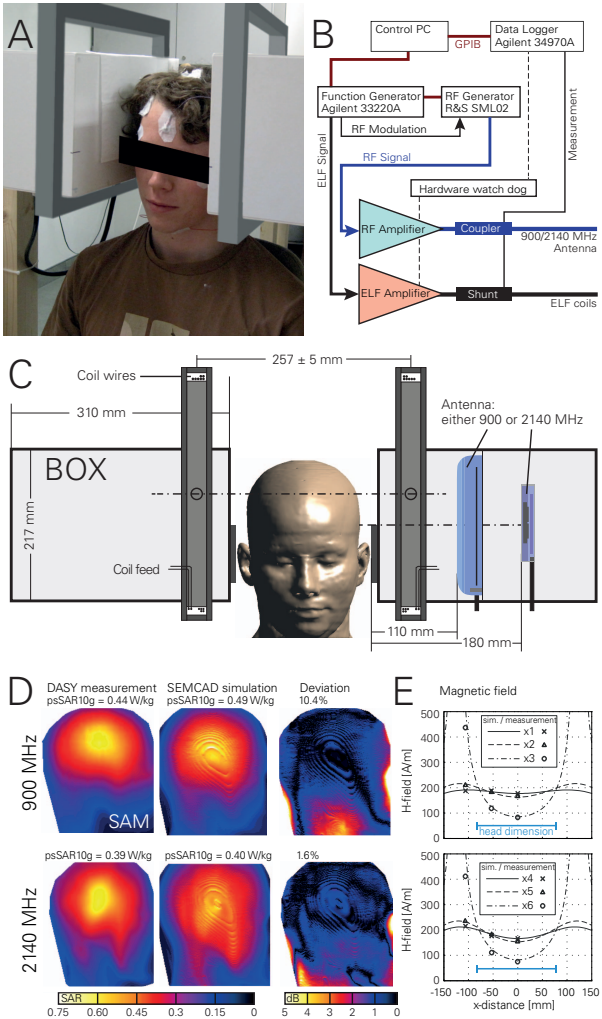

Figure 9.1: (A) Subject within the exposure system with attached Helmholtz-like coils. (B) Schematic of the exposure system hardware, and (C) of the boxed antenna enclosures with antenna positions (either the 900 MHz or the 2140 MHz antenna), coil housings and 'Ella' [35]. (D) SAM head surface SAR exposure comparison of measurement and simulation, as well as (E) the simulated and measured values of the ELF magnetic field (measurement positions x1-x6 indicated in Fig. 9.2).

antenna and a maximum size of 0.9 mm in the exposed tissues, leading to approx. 10 million voxels for the head and 60 million voxels for the entire simulation space. For numerical variability evaluations, two additional anatomical head models were used: the 34-year-old male adult 'Duke' (image resolution and segmentation characteristics correspond to 'Ella'; [35]), and the 40-year-old European female 'HR-EF1' with a coarser than state-of-the-art resolution of 1 mm in the ear region and 3 mm for the rest of the head. The latter was included for comparison with the precedent exposure system [90]. The magneto quasi static low frequency solver of SEMCAD X was applied to analyze the ELF magnetic field coil system, using a 2.5 mm grid resolution and low frequency current sources for the two coils.

9.5 Validation

Experimental validation was performed by comparing the RF exposure of the specific anthropomorphic mannequin (SAM, IEEE 1528-2003) in simulations with measurements obtained from the near field scanner DASY5/NEO (SPEAG), equipped with a calibrated dosimetric SAR probe (ET3DV6) and tissue simulating liquid (HSL-U10). The ELF magnetic field was validated using a Gaussmeter (FH49, Magnet-Physik, Germany) equipped with a 3 axis, temperature regulated magnetic field probe (HS-ZOA71-3208-05-T, probe diameter: 8 mm). The measured x-axes (x1-x6) are indicated in Figure 9.2.

9.6 Results

The dosimetric results of the RF system are summarized in Table 9.1. The configuration was optimized to achieve a similar exposure at the level of the lateral cerebral cortex with maximum exposure difference in the thalamus. This was obtained by selecting the two different carrier frequencies 900 and 2140 MHz and optimization for minimal differences between the average SAR induced in eight selected Talairach regions (grey matter within T1-T8, see Figure 9.2) by varying the distance of the patch antennas from the head. The results were distances of 110 mm and 180 mm for the 900 MHz and 2140 MHz an-

tenna, respectively, with a global psSAR10g ratio of 1.4 (e.g., values of 1 W/kg at 900 MHz and 1.4 W/kg at 2140 MHz). The corresponding psSAR10g efficiencies are 0.50 W/kg and 0.39 W/kg for 1 W forward power at the antenna feed point. The exposure of the different brain tissues and Talairach regions was characterized by the mean value, standard deviation, and psSAR1g. The experimental validation resulted in differences to the numerical prediction of 10.4% (900 MHz) and 1.6% (2140 MHz) that are well within the combined numerical and experimental uncertainty (see also Fig 9.1).

The ELF magnetic field over the volume of the brain has a standard deviation of 8%, except for the marginally exposed medulla oblongata (Fig. 9.2), and the achievable peak exposures are 800 A/m at 50 Hz and 140 A/m at 1 kHz. Sham exposure (anti-parallel currents) is >43 dB below the ELF exposure. The average deviation between ELF simulation and measurement remained below 7% (Fig. 9.1).

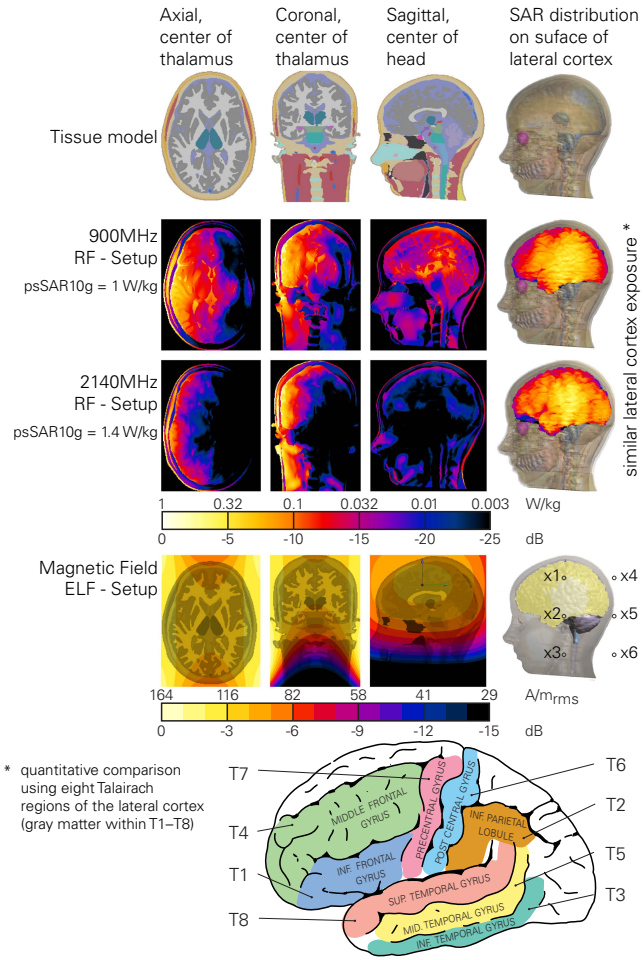

Figure 9.2: SAR distribution (axial, coronal, sagittal slices; lateral exposed cortex surface view) and selected Talairach regions (T1-T8). RF exposure levels are optimized for similar lateral cortex exposure (outermost 2-4 mm of the cortex). Maximum SAR not present in depicted slices. Illustration with RF exposure of the left hemisphere.

	Both hemispheres				Exposed hemisphere				Nonexposed hem.			Variation		Uncert.		Talairach region			
	1g[a]	av[b]	SD[c]	Loss[d]	1g	av	SD	Loss	1g	av	SD	1g	av	1g	av	No.	av	Var.	Unc,
	W/kg	W/kg	W/kg	mW	W/kg	W/kg	W/kg	mW	W/kg	W/kg	W/kg	%	%	%	%		W/kg	%	%
Zurich Setup, Ella																T1	0.33	15	3
Grey matter	1.06	0.16	0.20	116	1.06	0.29	0.22	102	0.18	0.04	0.03	12	20	5	3	T2	0.44	22	4
White matter	0.72	0.12	0.13	51	0.72	0.20	0.13	44	0.12	0.03	0.03	17	27	3	5	T3	0.71	18	2
Grey+White matter	1.02	0.15	0.18	167	1.02	0.26	0.20	146	0.18	0.04	0.03	12	21	7	3	T4	0.17	17	5
Thalamus	0.31	0.18	0.07	2.4	0.31	0.23	0.06	1.5	0.15	0.13	0.02	35	35	15	16	T5	0.64	16	3
Brain (without CSF)	1.32	0.15	0.18	201	1.32	0.26	0.20	174	0.18	0.04	0.04	21	22	4	4	T6	0.36	18	5
Brain (with CSF)	1.33	0.18	0.24	284	1.33	0.30	0.28	241	0.29	0.05	0.05	16	22	4	3	T7	0.28	17	3
Total head	1.72	0.13	0.24	605	1.72	0.23	0.31	525	0.29	0.04	0.05	16	16	8	1	T8	0.57	16	2
BoX-900MHz																T1	0.37	15	3
Grey matter	1.06	0.19	0.22	135	1.06	0.33	0.24	117	0.22	0.05	0.04	12	20	5	3	T2	0.69	22	4
White matter	0.72	0.14	0.14	61	0.72	0.24	0.14	51	0.16	0.04	0.04	17	27	3	5	T3	0.64	18	2
Grey+White matter	1.03	0.17	0.20	196	1.03	0.30	0.21	168	0.21	0.05	0.04	12	21	7	3	T4	0.25	17	5
Thalamus	0.37	0.21	0.07	2.9	0.37	0.25	0.08	1.7	0.18	0.17	0.02	35	35	15	16	T5	0.66	16	3
Brain (without CSF)	1.19	0.17	0.19	228	1.19	0.29	0.21	193	0.21	0.05	0.04	21	22	4	4	T6	0.59	18	5
Brain (with CSF)	1.42	0.20	0.27	327	1.42	0.34	0.32	272	0.42	0.07	0.07	16	22	4	3	T7	0.42	17	3
Total head	1.55	0.14	0.26	648	1.55	0.24	0.33	549	0.42	0.04	0.06	16	16	8	1	T8	0.63	16	2
BoX-2140MHz																T1	0.18	36	15
Grey matter	0.81	0.09	0.14	64	0.81	0.17	0.16	59	0.06	0.01	0.01	16	38	6	7	T2	0.40	37	3
White matter	0.40	0.05	0.07	22	0.40	0.09	0.08	20	0.04	0.01	0.01	15	39	6	12	T3	0.31	14	3
Grey+White matter	0.73	0.08	0.12	86	0.73	0.14	0.14	79	0.06	0.01	0.01	14	38	6	9	T4	0.18	35	9
Thalamus	0.049	0.019	0.014	0.26	0.049	0.029	0.013	0.20	0.013	0.009	0.005	45	60	10	11	T5	0.37	27	7
Brain (without CSF)	0.73	0.07	0.12	94	0.73	0.13	0.14	87	0.06	0.01	0.01	14	37	6	7	T6	0.36	37	6
Brain (with CSF)	0.92	0.09	0.15	139	0.92	0.16	0.19	125	0.17	0.02	0.03	21	37	13	8	T7	0.26	37	9
Total head	2.66	0.12	0.30	556	2.66	0.22	0.40	512	0.24	0.02	0.04	10	26	4	4	T8	0.34	35	11

Table Explanation	System	Antenna	Exposed hemisphere	10g-psSAR whole head	10g-psSAR without ear	10g-psSAR efficiency
[a] 1g-psSAR						
[b] avSAR	Zurich Setup, Ella	SPA920/65/9/0/V	left	1 W/kg	1 W/kg	0.645 (W/kg)/W
[c] SD of avSAR	BoX-900MHz	SPA860/65/9/0/V	left	1 W/kg	1 W/kg	0.503 (W/kg)/W
[d] total power losses	BoX-2140MHz	SPA2000/80/8/0/V	left	1 W/kg	0.93 W/kg	0.391 (W/kg)/W

Table 9.1: SAR values for different brain tissues and selected Talairach areas.

9.7 Study Configurations

A first hypothesis-driven study is to investigate if similar fields (amplitude and modulation) induced in the cortex result in the same effects independent of the carrier frequency and exposure of subcortical structures [Schmid et. al, 2011b]. With the presented optimized configuration, the average SAR in the thalamus is 8 times lower at 2140 MHz than at 900 MHz, while maintaining similar cortex exposure. Figure 9.2 illustrates the SAR distribution for both carrier frequencies in three orthogonal cuts. The system also enables the study of whether ELF and RF exposures have similar physiological responses when the modulation envelope of the RF signal corresponds to the ELF signal, and the effects of the ELF exposures posed by the mobile phones [65, 88]. All exposures were compliant with the safety guidelines defined by the International Commission on Non-Ionizing Radiation Protection [1], i.e., maintaining the basic restriction of 2 W/kg psSAR10g for RF exposures and complying with the summation of the multifrequency ELF field with the corresponding reference levels.

9.8 Uncertainty

The uncertainty and variability analysis for the dosimetric study was performed following the concept of the National Institute of Standards and Technology (NIST) TN1297 [Taylor and Kuyatt, 1994]. The uncertainty analysis included: (a) ±10% variation of the tissues' relative permittivity and conductivity [17]; (b) discretization of the head, estimated with half and double voxel sizes; and (c) segmentation of the head anatomy, based on the differences between left and right hemisphere. The variation analysis included: (a) changes in antenna position relative to the head (±5 mm in x direction, ±10 mm in y, z direction); (b) different head size, assessed by scaling the reference head model ('Ella') by ±10%; and (c) usage of two additional head models, relevant for the representation of the inter-subject and age-related structural differences of the population. The European female model 'HR-EF1' made the most significant contribution to variability (see Tab. 9.1), demonstrating the need for enhanced imaging and

segmentation techniques.

9.9 Conclusions

In conclusion, a novel system for double-blind human EM provocation studies has been developed and fully characterized. It satisfies the precision, control of fields and potential artifacts, and provides the exposure flexibility necessary to investigate the response of hypotheses-driven electromagnetic field exposure schemes on brain function. It allows the exposure of the CNS to ELF magnetic fields and RF fields of different carrier frequencies (900 MHz and 2140 MHz). Very similar induced field distributions in the lateral cortex are provided at both radio frequencies and uniform exposure at ELF. Furthermore, modulation and the ELF signals are obtained by a freely programmable arbitrary signal generator allowing a wide range of worst-case exposure scenarios to be simulated with peak RF exposures of up to 60 W/kg and ELF exposures up to 800 A/m at 50 Hz. The system is therefore suitable for testing a wide range of hypotheses of EMF interaction with brain function.

Chapter 10

Evaluation of Electrode Artifacts and Thermal Ripples of EEG RF Experiments

10.1 Abstract

[1] The effects of radiofrequency (RF) exposure on waking and sleep electroencephalography (EEG) have been in focus since mobile phone usage became pervasive. It has been hypothesized that effects may be explained by 1) enhanced induced fields due to RF coupling with the electrode assembly, 2) the subsequent temperature increase around the electrodes, or 3) RF/thermal pulsing caused by localized exposure in the head. We evaluate these three hypotheses by means of both numerical and experimental assessments made with appropriate phantoms and anatomical human models. Typical and worst-case electrode placements were examined at 900 and 2140 MHz. Our results indicate that hypothesis 1 can be rejected, as the induced fields cause $< 20\%$ increase in the 10g-averaged specific absorption rate (SAR). Simula-

[1] This Chapter has been published in [91].

tions with an anatomical model indicate that hypothesis 2 is also not supported, as the realistic worst-case electrode placement results in a maximum skin temperature increase of 0.31 °C while brain temperature elevations remained < 0.1 °C. These local short-term temperature elevations are unlikely to change brain physiology during the time period from minutes to several hours after exposure. The maximum observed temperature ripple due to RF pulses is $\ll 0.001$ °C for GSM-like signals and < 0.004 °C for 20-fold higher pulse energy, and offers no support for hypothesis 3. Thus, the mechanism of interaction between RF and changes in the EEG power spectrum remains unknown.

10.2 Introduction

Research into the effects of pulsed radiofrequency (RF) electromagnetic field (EMF) exposure on brain physiology has been in focus since the usage of mobile phones became pervasive. The most consistently reported effects in various studies conducted by different laboratories are changes in the electroencephalogram (EEG) power spectrum, e.g., [92, 79, 80, 81, 93, 94, 68, 82, 65, 66]. A recent summary can be found in the publication of [95], in which the authors conclude that Global System for Mobile Communications (GSM)-type signals may result in minor effects on brain activity with no adverse health effects. Interesting findings regarding potential mechanisms include that unilateral RF exposure of the brain does not induce hemispheric asymmetry of the EEG power [80], that continuous wave (CW) non-pulsed RF does not enhance EEG power [81, 85], that a dose-response relationship can be demonstrated [82], and that pulse modulation schemes with frequency components below 20 Hz seem to be sufficient to affect EEG power [66]. Further reported effects include changes in regional cerebral blood flow [81, 85], brain glucose metabolism [69], and sleep-dependent performance improvement [76].

To minimize the time between RF EMF exposure, e.g., from a cell phone, and sleep onset, many but not all human provocation studies have been performed with attached electroencephalography (EEG) electrodes, e.g., [79, 82, 65, 66], or the EEG has been recorded during RF exposure [79, 96, 97, 76]. These effects have usually been

referred to as the "non-thermal biological response" of RF EMF exposure. Thermal interaction is not a plausible explanation for the observed effects, as the resulting temperature increases are considered biologically non-relevant. In the case of the cited experiments, the temperature increases remained below 0.5 °C in the whole head and below 0.25 °C in the brain, as the exposure levels did not exceed the corresponding general public guideline limits of the International Commission on Non-Ionizing Radiation Protection (ICNIRP) [1, 74]. The limit is defined by the specific absorption rate (SAR), with a maximum peak spatial SAR averaged over 10 g of tissue (psSAR10g) of 2 W/kg.

On the other hand, three hypotheses have often been discussed, namely, that the observed effects are caused by 1) the locally increased induced fields in the brain due to the coupling of the incident field with the assembly of the electrodes and electronics, 2) the subsequent temperature increase induced by the locally enhanced fields around the electrodes, or 3) the thermal pulses in the brain tissue due to the absorption of the RF pulses of the mobile phone signal. In most published studies, the RF pulsing has been derived from GSM signals. The objective of this paper is to thoroughly investigate the plausibility of these three hypotheses. We do not introduce or discuss any new or alternative hypotheses for the observed biological responses.

In earlier experimental studies, shielding effects from field attenuation below the EEG leads of up to 10% for the psSAR1g/10g have been estimated for typical lead orientations [90]. The localized enhancements around the electrode tip do not affect the psSAR10g ($< 1\%$), but increase the psSAR1g by 35%. Recent numerical studies showed altered field levels caused by the EEG electrodes of $< 20\%$ in psSAR1g/10g for typical lead orientations and up to 60% for worst-case alignments in psSAR1g [97, 98]. In another simulation study, an increase of ca.12% in psSAR10g due to the EEG electrodes was reported [99]. Head average SAR remains unaffected by these localized field enhancements. However, it should also be noted that not all of the cited studies involved attachment of electrodes during exposure, e.g., [68] found similar effects with electrodes attached only after the exposure period, providing evidence that the electrodes are at most a minor confounding factor. In this study, we investigated the configurations of lead and electrode placements typically used in

the cited studies. In general, all EEG recording electronics were either well-protected by means of appropriate RF filtering elements, or the recording electronics were entirely disconnected, both of which approaches satisfy good laboratory practice (GLP) requirements (as described in the Methods section). The 900 MHz and 2140 MHz carrier frequencies represent the lower and upper limits of typical mobile phone frequency bands. For reasons of completeness, we also investigated the worst-case configurations for the maximum upper limit. In addition, we assessed the magnitude of the thermal pulses for GSM-like exposures and for a signal with a peak-to-average ratio (PAR) of 50 at 10Hz that is much larger than the PAR in any of the cited studies.

10.3 Methods

The basic interactions between the incident field and the EEG recording system are induced currents on the leads and electrodes that may have the following effects [100]: (a) direct interaction by rectification of the RF at the non-linear elements of the EEG recording system; (b) strongly enhanced fields at the electrode tip that may induce fields in the brain that greatly exceed direct exposure to the source or result in significant temperature increases below the electrode, which, in turn, modulate EEG via an unknown mechanism; and (c) RF shielding or enhancement, as the electrodes may act as reradiators of the incident fields in close proximity to the tissue. The experiments are designed to test the three hypotheses introduced above; no new or alternative hypotheses are considered.

The electronics of all involved systems were appropriately shielded by full metallic enclosure, and all electrodes and other cables were connected via effective feed-through filters (RF attenuation better than –70dB, factor > 3100 in field level) [97, 76]. Artifacts via interaction (a) could thus be excluded. The interactions (b) and (c) and their implications on our three hypotheses were investigated by means of the following four scenarios: Setup A, a flat homogeneous model, simulation and measurement; Setup B, a flat tissue-layered head model, simulation only; Setup C, a homogeneous specific anthropomorphic mannequin (SAM) model, simulation and measurement; and Setup

D, an anatomical model Ella [35], simulation only. Setups A and D include thermal evaluations. An overview of the different configurations is shown in Figure 1.

The gold-plated silver EEG electrodes investigated have a diameter of 8 mm and a thickness of 1 mm (GRASS Technologies, West Warwick, RI, USA). In the simulation models, the electrodes were placed in direct contact with the skin, which results in sharp RF interfaces between metal and tissue. More-realistic modeling is challenging, as the contact area may vary, depending on the contact paste used, interference from hair, etc., and result in different contact qualities. Smaller contact areas, e.g., a tilted electrode that touches only one side, did not increase psSAR10mg/1g/10g in simulations and, therefore, indicate that local temperature is not greatly affected by the contact area. Furthermore, the small temperature changes are not believed to cause electrode contact impedance shift and have no effect on the recording system in the majority of the studies, where all EEG sampling has been performed after RF exposure.

The electrode leads were modeled as perfect conductors with a surrounding isolator and a length of > 120 mm (standard leads are longer than 600 mm). The highest exposure at the tip was found at the resonant length $\lambda/4$, i.e., 80 mm at 900 MHz, with the lead normal to the surface and perfectly aligned with the incident E-field. Therefore, this single generic lead corresponds to the worst-case lead configuration with respect to the current induced below the electrode, i.e., realistic configurations of multiple EEG leads will generally result in lower exposures. The RF field was generated with linearly polarized planar patch antennas (SPA860/65/9/0/V and SPA2000/80/8/0/V, Huber & Suhner, Herisau, Switzerland) at the investigated carrier frequencies of 900 and 2140 MHz. The simulation models of the antennas were validated by comparing the broadband input impedance. All measurements were performed with CW with an output power drift less than 0.3 dB (7%). The effect of RF pulsing on temperature was investigated with the anatomical head, Setup D, as this represents the most realistic scenario.

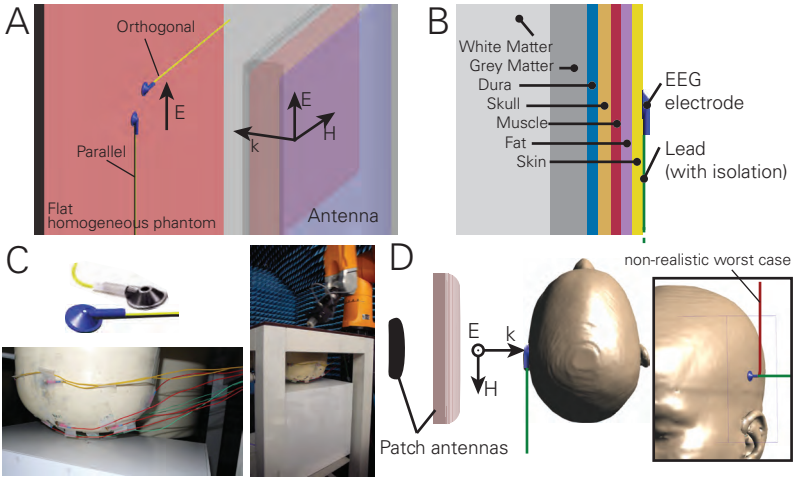

Figure 10.1: Overview of simulation and measurement configurations. A: Flat homogenous phantom with one electrode-lead orthogonal to incident E-field and one parallel. B: Flat tissue-layered model of the human head. C: EEG electrodes attached to SAM for measurements with DASY5/NEO (SPEAG). D: Ella from the Virtual Population with one EEG electrode attached above the psSAR10g hotspot location.

10.3.1 Setup A: Flat homogeneous model

The worst case in terms of peak global head exposure is an EEG electrode attached at the location of the natural SAR hotspot of the head. This scenario was measured and simulated with a flat homogeneous phantom and two electrodes, one with parallel and the other with orthogonal lead orientation relative to the E-field (see Figure 1A). Dosimetric temperature probes (TV3LAB; SPEAG, Zurich, Switzerland) were placed at the estimated hotspot location and, as a reference, at a sufficient distance to the electrodes (T1 – T3, Fig. 2). To avoid thermally induced convection, a tissue simulating gel ($\varepsilon_{900MHz} = 56$, $\sigma_{900MHz} = 0.96$ S/m; $\varepsilon_{2140MHz} = 53$, $\sigma_{2140MHz} = 1.83$ S/m, thermal conductivity $\kappa = 0.62$ W/m/K, $\rho = 993$ kg/m3, c = 3200 J/kg/K) was used. The numerical simulations were conducted with SEMCAD X V14.8 (SPEAG) and compared to the thermal measurements.

10.3.2 Setup B: Flat tissue layered head model

The configuration of Setup A was extended to a tissue-layered simulation model (Fig. 1B), where the human head is approximated with subsequent planar layers of the different head tissues [101]. The smallest estimated thicknesses — 1 mm skin, 1 mm fat, 1 mm muscle, 1.5 mm skull, 1 mm dura, no cerebrospinal fluid (CSF), 4 mm gray matter, > 20 mm white matter — have been used to mimic the worst-case scenario, where the brain is closest to the surface.

10.3.3 Setup C: Homogeneous SAM model

Figure 1C shows the measurements performed with a twin SAM phantom filled with a broadband liquid (SPEAG, Zurich, Switzerland, HSL-U10: $\varepsilon_{900MHz} = 42$, $\sigma_{900MHz} = 0.97$ S/m; $\varepsilon_{2140MHz} = 39.5$, $\sigma_{2140MHz} = 1.58$ S/m) to simulate brain tissue. The near-field scanner DASY5/NEO (SPEAG) was used with calibrated dosimetric SAR probes of type ET3DV6 and EX3DV4 (SPEAG). The antenna positioning was identical to that used by [78], and a typical EEG electrode configuration — derivation C3A2, electro-oculogram, electromyogram, with a total of 15 electrodes on the head — was mounted onto the SAM head as described, e.g., in [65]. The RF absorption pattern without

electrodes/leads was compared to a set of ten different configurations for both RF frequencies, A1 – A5 & B1 – B5. The electrode-tissue contact quality was configured with (A) electrical isolation of the electrodes outside the SAM shell and (B) electrical contact between the electrodes and the tissue simulating liquid. Measurements were performed for (A) and (B) in combination with (1) ideal lead positioning orthogonal to the E-field, (2) realistic typical positions with $< 15°$ angles between leads and E-field polarization, (3) realistic worst-case placement with up to 30° angles, (4) 10 mm head distance to mimic thick hair density, and (5) with electrical contact cream (EC2, GRASS Technologies).

As good electrical contact of the electrodes is a prerequisite for EEG recording, the B2-configuration — electrical contact combined with realistic lead alignment — is the most realistic measurement scenario, and was simulated to confirm the exposure pattern of the measurements. SAR values at a distance of 1 – 2 mm from the SAM surface were extracted to match the actual measurement location of the EXDV4 probes.

10.3.4 Setup D: Anatomical model Ella

Finally, the EEG electrode attached above the normal SAR hotspot location to the head of Ella from the Virtual Population [35] was simulated. The dielectric and thermal tissue parameters were assigned according to [16]. A temperature increase simulation, which assumes thermal equilibrium at the onset of heating, was performed. Thermoregulated blood flow was not considered, as the estimated temperature increases are very low [21]. A convective thermal boundary condition (h = 6 W/m2/K) to the surrounding air was set. The electrode was modeled as a perfect thermal isolator a conservative approach to the unknown convection boundary. Setting a similar boundary as to air, however, had a marginal effect on the temperature increase ($< 1\%$) due to the small dimensions of the electrode.

Voxel size was refined down to 0.3 mm within the estimated psSAR10g cube, yielding a time step according to the Courant–Friedrichs–Lewy (CFL) condition of 0.06 s for the subsequent thermal simulation. The exposure level was normalized to a psSAR10g of 2 W/kg without the electrode, which is the relevant guideline limit ICNIRP, 1998], and

without including the ear volume in the evaluations. The ear was modeled as pressed. A set of non-realistic lead orientations was investigated to find the worst-case pathway for picking up RF energy along the wire, with variations in lead orientation and length, which is important for resonant configurations. The highest localized exposure was achieved with a horizontally oriented electrode-lead connector, the lead bent thereafter heading along the vertical E-field polarization, and a lead length of roughly $\lambda/4$, i.e., 80 mm (Fig. 1D). Other resonant lead lengths of $3\lambda/4$ and longer lead to lower contact currents due to the narrow beam-width of the antenna. Such a configuration was not used in any of the cited experimental studies.

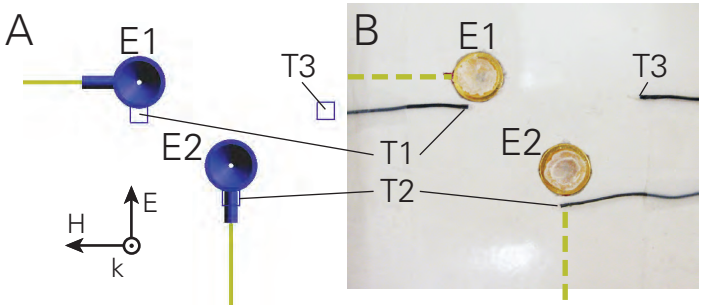

Figure 10.2: A: Flat homogenous phantom simulation model and B: measurement setup. The electrode E1 and its lead is orthogonal, E2 is parallel to the E-field. The cubic representation of the temperature probes T1-T3 within the simulation model accounts for sensor placement uncertainty.

10.4 Results

The typical field alterations inherent to all configurations were (1) slight attenuation of the fields below the path of the lead, (2) high localized attenuation directly below the electrodes, and (3) enhancement of the fields at their edges aligned with the linear polarized E-field. These three effects can be seen best in Figure 10.3.

10.4.1 Setup A: Flat homogeneous model

Figure 3 shows the resulting SAR distribution around the EEG electrodes E1 and E2 in the flat homogeneous model (Setup A). The shielding effect is most prominent when the leads are parallel to the E-field, while the effect vanishes in an orientation orthogonal to the E-field (E2 vs. E1 in Fig. 3). The resulting temperature distribution after 300 s of heating (Fig. 3B) is much more equalized than the SAR distribution due to the thermally small distances. Although the localized SAR hotspots around the electrodes are of similar magnitude, the E1 induces higher temperatures due to the absence of lead-shielding near to the E2 electrode. This lead-shadow (Fig. 3AB) is thermally very close to the hotspot and prevents excessive heating. It is more developed at 2140 MHz (not depicted), explaining the higher temperature drop in T2 (Fig. 3C).

A comparison between numerically estimated temperature increases and the corresponding measurements T1 – T3 can be seen in Figure 3C. T3 shows a linear increase corresponding to the local SAR of 3.6 W/kg, as the probe is within the homogeneous non-perfused gel at a location without strong field-gradients. The measurements are all within one standard deviation (SD, k = 1) of the simulated transient temperatures with respect to probe placement uncertainty within the cubic areas T1 – T3 (Fig. 3C).

10.4.2 Setup B: Flat tissue layered head model

In Figure 4, the effect of the EEG electrodes on the SAR in the human head anatomy is estimated with the flat tissue-layered model (Setup B). The induced currents lead to localized superficial field enhancements, but have very limited effect on brain exposure, with a SAR enhancement below 25%.

10.4.3 Setup C: Homogeneous SAM model

Figure 5 shows the SAM surface SAR distributions with and without attached electrodes (Setup C) for realistic lead placement and electrodes electrically connected to the tissue simulating liquid (B2-configuration). The simulation results (Fig. 5A) correspond well to

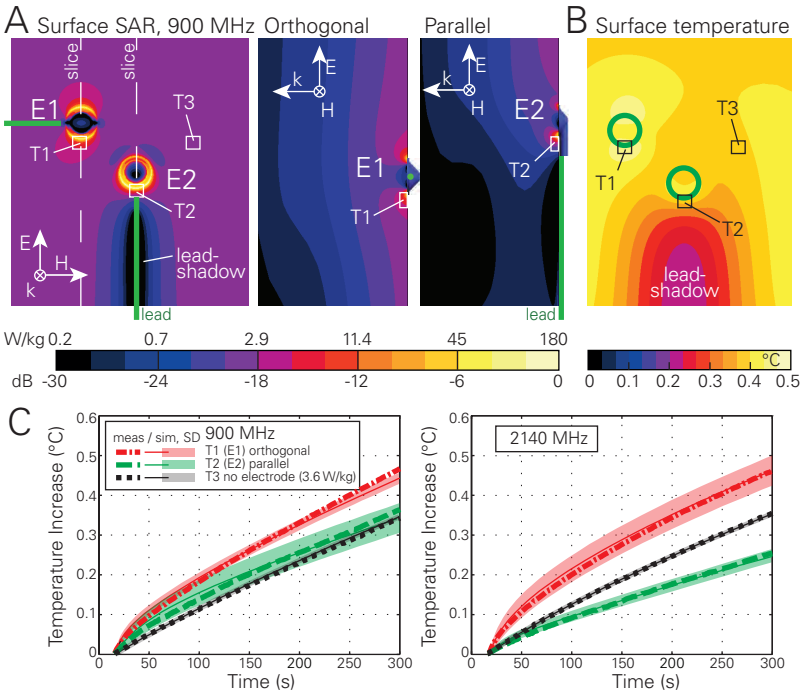

Figure 10.3: A: Simulated SAR distribution in the flat homogeneous phantom (only the 900 MHz distribution is depicted as the distribution is similar at 2140 MHz). B: Simulated temperature distribution at 900 MHz after 300 s heating. C: Thermal validation measurements compared to simulated temperature increases. The exposure level was adjusted to 3.6 W/kg local SAR at the temperature probe T3. Mean and standard deviation is shown for the cubic areas T1 T3 in the simulation. T2 (at 900 MHz) shows a large uncertainty because of the strong temperature gradient in this region.

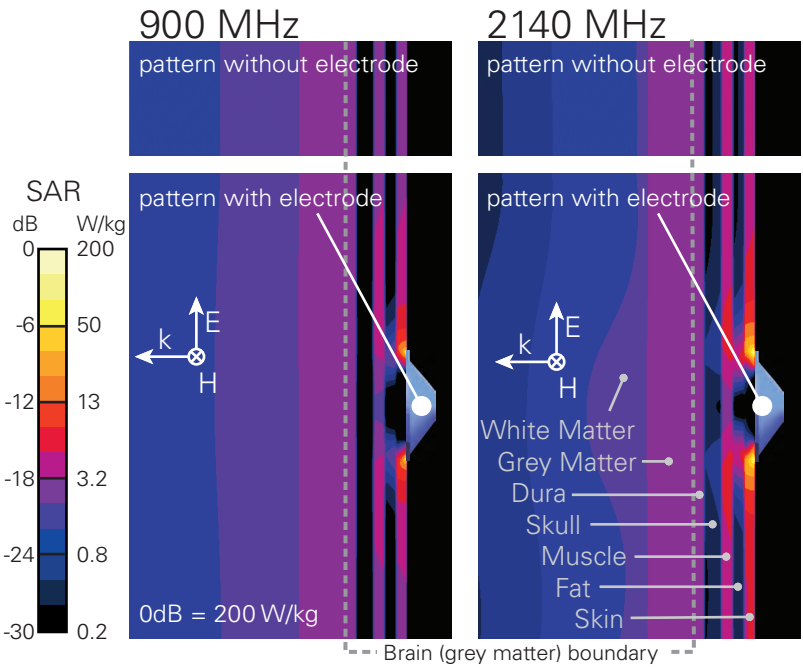

Figure 10.4: SAR distribution in the tissue-layered model with the EEG electrode assembly orthogonal to the E-field. The figure illustrates the localized effect on SAR as field enhancements generally remain within the superficial layers. The 30 dB (factor 1000) dynamic range corresponds to 2 dB (factor 1.6) per contour; linear values are provided.

the measured absorption pattern (Fig. 5B). The magnitude of the effect of the attached EEG electrodes can be seen in Figure 5C, which shows the deviation of the measurement with and without electrodes.

Ten different lead configurations were investigated, from ideal to worst-case placement of the 15-EEG-electrode setup with and without electrical contact to the tissue simulating liquid; a maximum attenuation of the psSAR1g/10g of less than 14% at 900 MHz (max. in B3-configuration) and less than 17% at 2140 MHz (max. in B4-configuration) was observed, compared to the psSAR1g/10g at the same location in the reference measurement without electrodes. The order of attenuation is well within the range of recent numerical estimations [97, 98] and measurement results [90].

The localized hotspot around the electrode positions increases the psSAR1g by up to 90% in the B3-configuration with realistic worst-case lead alignment, but does not significantly affect the psSAR10g. These results are in agreement with the cited simulation studies. However, none of the attached electrodes was located directly on the natural hotspot of the SAM head (see Fig. 5).

10.4.4 Setup D: Anatomical model Ella

An overview on the simulation results with Ella (Setup D) can be seen in Figure 6 and is summarized in Table 1. The EEG electrode affects the psSAR10g of the whole head by less than 10% due to the very localized field enhancement. The peak temperature increase (pΔT) is 0.22 – 0.24 °C without and 0.26 – 0.31 °C (+15%/+30% at 900/2140 MHz) with the electrode attached, with an applied antenna input power corresponding to 2 W/kg psSAR10g without the electrode. Steady state is reached after about 20 min (Fig. 7A).

For the worst-case configuration, i.e., monopole configuration with a resonant lead length of $\lambda/4$ or 80 mm and normal orientation to the surface (Fig. 1D), a temperature increase in the superficial skin layer of 3.5 °C and in the brain of 0.3 °C were estimated. This emphasizes the need to align the leads carefully with respect to the incident fields. If optimal alignment is not possible, e.g., in circularly polarized fields [76], specific measures should be taken, e.g., addition of absorbing material or selection of off-resonance lead lengths.

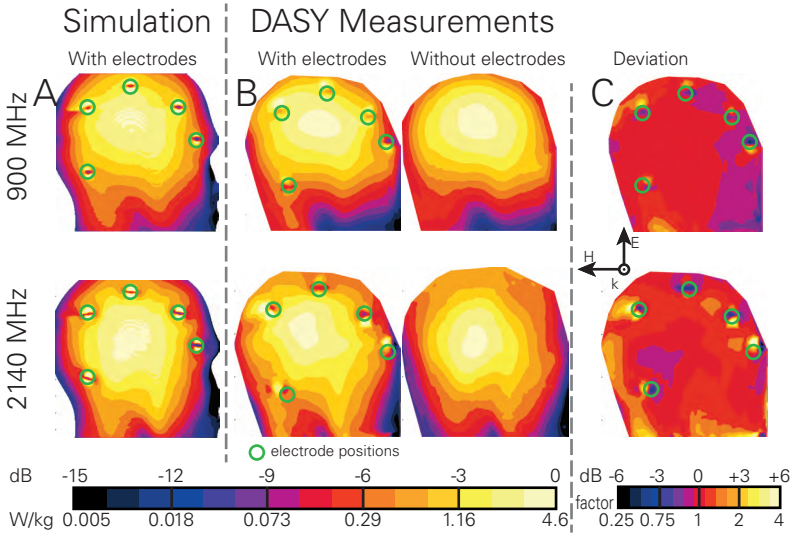

Figure 10.5: SAR simulations and measurements on the specific anthropomorphic mannequin (SAM) surface with and without attached electrodes at two RF frequencies (900 and 2140 MHz). Leads in typical configuration and electrodes electrically connected to the tissue simulating liquid (B2-configuration). The field is enhanced at the edges of the EEG electrodes, aligned with the incident E-field polarization. View from inside the SAM head, lateral exposure from left, eyes/nose on the right side of the graphs. A+B: 0 dB corresponds to 4.6 W/kg. C: The local SAR deviation caused by the electrodes stays within ±6 dB (factor 4) in the DASY5/NEO (SPEAG) measurements.

	psSAR10g whole head	psSAR1g whole head	psSAR10mg whole head	pΔT whole head	pΔT brain
900 MHz	[W/kg]	[W/kg]	[W/kg]	[K]	[K]
w/o electrode	2	2.4	17.4	0.24	0.096
with electrode	2.02	2.52	36.8	0.31	0.097
difference	1%	5%	111%	30%	< 1%
2140 MHz					
w/o electrode	2	2.86	10.6	0.22	0.072
with electrode	2.19	3.72	32.1	0.26	0.074
difference	9%	30%	202%	15%	2%
900 MHz NR[1]	[W/kg]	[W/kg]	[W/kg]	[K]	[K]
with electrode	13.9	57.4	452	3.5	0.31
difference	595%	2390%	2490%	1460%	225%

[1]Non-realistic worst case lead alignment with resonant length

Table 10.1: SAR levels and maximum temperature increases in Ella with and without an EEG electrode at the SAR hotspot location. Values evaluated without the ear.

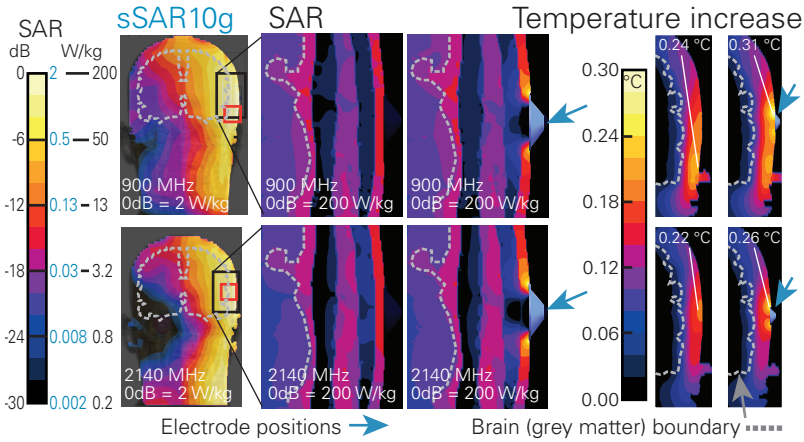

Figure 10.6: SAR and thermal simulation of Ella with and without a single electrode attached near the psSAR10g location for 900 and 2140 MHz. Exposure level was normalized to psSAR10g of 2 W/kg (without ear, location indicated with red square), unilateral exposure with planar patch antennas.

10.4.5 Translation of RF pulses to ΔT ripples

Many of the modern digital communication systems generate signal emissions with low frequency power variations and relative large peak-to-average ratios (PAR). The time-division multiple access system (TDMA) GSM emits signals with pulses of width 0.57 ms at a basic repetition rate of 217 Hz and a PAR of 8.32. As CW exposure does not enhance EEG spectral power [81, 85], the obvious question is whether the resulting thermal pulsing/expansion, i.e., hypothesis 3, could explain the differences.

The simulation results for the thermal ripples were estimated with the human head model (Setup D) and are shown in Figure 7B. The ripple of GSM is much less than 0.001 °C. Even for pulses with a PAR of 50 and a slow repetition rate of 10 Hz (leading to 100 W/kg psSAR10g pulses of 2 ms length), the temperature ripples would be less than 0.004 °C with attached EEG electrodes and 0.001 °C without electrodes. This is less than 2% of the steady-state temperature increase for both cases (Fig. 7B). In the most aggressive modulation function applied in the human provocation studies cited above, a PAR of 32 with 14 Hz repetition rate (64 W/kg psSAR10g pulses for 2.2 ms) was used [65].

10.4.6 Uncertainty Analysis

The uncertainty analysis for the dosimetry study (Setup D) was evaluated according to the concept elaborated by the National Institute of Standards and Technology (NIST) TN1297 [41], and is summarized in Table 2. The uncertainties for psSAR10g/1g remain below 10% (SD, k = 1). The RF-induced peak temperature increase is subjected to the non-correlated uncertainties of (1) SAR, (2) simulation convergence, (3) thermal model discretization, (4) thermal conductivity, (5) boundary conditions, (6) blood heat capacity, and (7) volumetric blood perfusion. The tissue heat capacity has no influence on the pΔT values attained, and the metabolic heat generation in thermal increase simulations is assumed to be in thermal equilibrium. The total temperature increase uncertainty is less than 30% (SD, k = 1), in agreement with [39] (31%).

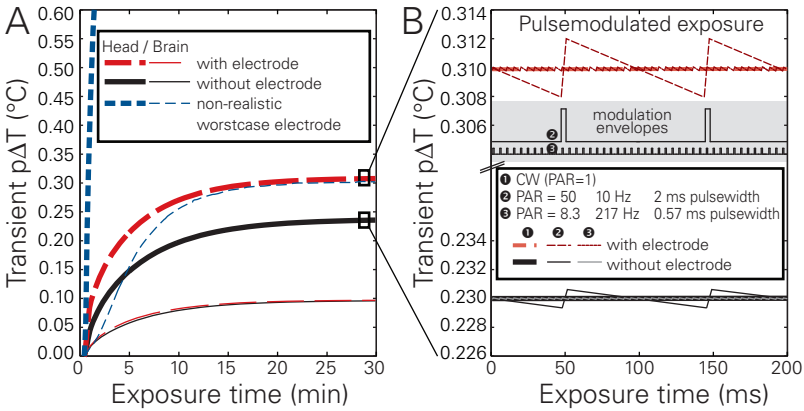

Figure 10.7: A: Transient peak temperature increase in the whole head and in the brain for exposure with psSAR10g = 2 W/kg at 900 MHz. B: Temperature ripple of pulse-modulated RF exposure with different peak-to-average ratios (PAR) and pulse repetition rates. Signal (2) represents a worst-case modulation envelope, signal (3) the main component of a typical GSM modulation.

A. EM Simulation Uncertainty		
Parameter	Range	psSAR10g/1g
Convergence	Simulation length: + 100%	0.9%
Model discretization	Voxel size: 0.3 mm, 2 mm	1.9%
Dielectric conductivity	σ: ± 10%	3.9%
Dielectric permittivity	ε: ± 10%	1.9%
Density	r: ± 10%, in single tissue	5.8%
RSS: Local SAR uncertainty		**7.5%**
B. Thermal Simulation Uncertainty		
Parameter	Range	pΔT
Local SAR uncertainty	from (A)	7.5%
Convergence	Simulation length and time step	1.2%
Model discretization	Voxel size: 0.3 mm, 2 mm	4.8%
Thermal conductivity	κ: ± 20%	5.7%
Thermal boundary cond.	h: ± 50%	3.1%
Blood heat capacity	$\varrho_b \cdot c_b$: ± 10%	3.7%
Basal (constant) perfusion	B_0: ± 50% (all tissues)	26.6%
RSS: Peak temperature increase uncertainty		**29.1%**

Table 10.2: Standard combined uncertainties for the numerical evaluations in Ella (Setup D). Stated uncertainty values are standard deviations (k = 1) in the assumed normal probability distribution. As they are uncorrelated, they can be combined by root-sum-square (RSS) procedures.

10.4.7 Discussion and Conclusion

We have shown that the fields induced in the brain are increased by less than 20% for the psSAR10g, by less than 90% for psSAR1g, and by less than 210% for psSAR10mg when the recording system is attached to the numerical head model compared to the same exposures without the recording system. The subsequent temperature increases in brain tissues remain below 0.1 °C (+2%). These simulation results contradict hypothesis 1, that the reported effects are a result of the field enhancements caused by the presence of the electrodes and would not be observed without the EEG recording system attached.

The maximum realistic temperature increase below the electrode was 0.31 °C with electrodes, compared to 0.24 °C without electrodes, an increase of ca. 30%. It should also be noted that, in studies where the electrodes were attached only after exposure, effects comparable to those from studies with electrodes attached during exposure were observed [68]. Thus, the reported effects are unlikely to be caused by the induced fields and subsequent heating at the tip of the electrodes predicted by hypothesis 2. The use of custom-made high-impedance leads that are nearly RF transparent in place of the metal leads would further reduce the small induced fields effects and also give more freedom regarding orientation of the leads with respect to the incident field polarization [100].

The thermal ripple caused by the GSM modulation is very small ($\ll$0.001 °C) and, therefore, offers no support for hypothesis 3, that the reported changes in the EEG spectral power are a result of the thermal pulsing in the brain.

Therefore, the interaction mechanism between pulse-modulated RF and changes in the EEG power spectrum remains unknown, and future exploration of putative mechanism requires innovative basic research and new approaches. Potential mediators of RF interactions proposed include oscillatory brain activity caused by sensory perception of RF and non-synaptic or ephaptic coupling of cortical neurons [76].

Chapter 11

Stimulation of the brain with radiofrequency electromagnetic field pulses affects sleep-dependent performance improvement

11.1 Abstract

[1]**Background:** Sleep-dependent performance improvements seem to be closely related to sleep spindles (12–15 Hz) and sleep slow-wave activity (SWA, 0.75–4.5 Hz). Pulse-modulated radiofrequency electromagnetic fields (RF EMF, carrier frequency 900 MHz) are capable

[1]This Chapter has been published in [76].

to modulate these electroencephalographic (EEG) characteristics of sleep.

Objective: The aim of our study was to explore possible mechanisms how RF EMF affect cortical activity during sleep and to test whether such effects on cortical activity during sleep interact with sleep- dependent performance changes. Methods: Sixteen male subjects underwent 2 experimental nights, one of them with all-night 0.25–0.8 Hz pulsed RF EMF exposure. All-night EEG was recorded. To investigate RF EMF induced changes in overnight performance improvement, subjects were trained for both nights on a motor task in the evening and the morning.

Results: We obtained good sleep quality in all subjects under both conditions (mean sleep efficiency $> 90\%$). After pulsed RF EMF we found increased SWA during exposure to pulse-modulated RF EMF compared to sham exposure ($P < 0.05$) toward the end of the sleep period. Spindle activity was not affected. Moreover, subjects showed an increased RF EMF burst-related response in the SWA range, indicated by an increase in event-related EEG spectral power and phase changes in the SWA range. Notably, during exposure, sleep-dependent performance improvement in the motor sequence task was reduced compared to the sham condition (-20.1%, $P = 0.03$).

Conclusion: The changes in the time course of SWA during the exposure night may reflect an interaction of RF EMF with the renormalization of cortical excitability during sleep, with a negative impact on sleep-dependent performance improvement.

11.2 Introduction

Large public and occupational populations are exposed to radiofrequency electromagnetic fields (RF EMF) as those emitted by mobile phones. Since these fields are mainly absorbed by the head, numerous studies investigated the effect of RF EMF exposure on brain physiology. Indeed, several studies consistently showed that RF EMF can alter brain activity. For example, studies focusing on electroencephalographical (EEG) spectral power showed that pulse-modulated RF EMF exposure increased power in the alpha and spindle frequency range (7.5–14.5 Hz) during non-rapid eye movement (NREM) sleep

[79, 80, 68, 82, 66, 65]. Recently, also an increase of delta power (<4.5 Hz) was observed [66]. Similarly, exposure during wakefulness increased alpha power in the spontaneous waking EEG (8–12 Hz, [102, 81, 103]). The crucial factor for these effects is the extremely low-frequency (<300 Hz) pulse modulation of the RF EMF, since exposure to the RF carrier frequency alone had no effect [102, 81]. Thus, RF EMF pulses affect brain activity but do they also have an impact on daily performance? Indeed, though not very consistently, studies found performance changes after or during pulsed RF EMF exposure [104]. All of these studies investigated the effects of RF EMF exposure during wakefulness on performance. Since various studies support a crucial role of sleep in memory and learning processes (for a review see Ref. [105]) the question arises whether the RF EMF induced changes of brain activity during sleep may interact with these processes. Interestingly, the beneficial effects of sleep on post-sleep performance in specific learning tasks are closely related to sleep spindles (e.g., [106, 107]) and to sleep slow-wave activity (SWA, EEG power between 0.75 and 4.5 Hz; (e.g., [108, 109, 110]).

Since we have profound knowledge about how sleep spindles and slow waves are generated and regulated, we took advantage of this knowledge to study changes in brain activity during sleep. Slow waves are the main characteristic of deep sleep and visible as high-amplitude, low-frequency oscillations in the EEG [111]. They have a cortical origin and are closely related to the homeostatic regulation of sleep [112]. Thus, as sleep pressure dissipates in the course of a sleep period also SWA decreases [112]. Sleep spindles are generated by the thalamocortical system [113, 114] and can be observed across the scalp (i.e., in different surface EEG derivations placed all over the scalp). Both sleep rhythms are involved in learning and memory processes and may be manipulated by pulsed RF EMF. We took advantage of these observations and aimed at 1) exploring possible mechanisms how pulsed RF EMF may affect cortical activity during sleep and 2) whether these effects on cortical activity during sleep interact with sleep-dependent performance changes. To do so, in our experiment each subject was exposed to RF EMF pulses during the sleep episode in one of 2 experimental nights. Our intermittent pulse modulation design of the RF EMF allowed us to investigate whether single RF EMF bursts directly evoke EEG responses during sleep. We further

investigated whether pulsemodulated RF EMF during sleep interact with the reported sleep- dependent performance improvement in a well-characterized motor sequence learning task (e.g., [115]).

11.3 Materials and methods

11.3.1 Subjects

Sixteen healthy male subjects (18–21 years, 19.9 ± 0.2, mean ± SEM) participated and completed the study. The number of subjects was chosen based on previous studies that also investigated the effects of pulsed RF EMF and showed significant changes in spectral power in the sleep EEG (e.g., 1, 4, 8). Only male subjects were included since in female subjects spindle activity varied systematically across the menstrual cycle [116]. Participants underwent a telephone and questionnaire screening to exclude personal or family history of psychopathology, chronic diseases, sleep disorders, and current use of psychoactive agents or other medications. No subject traveled across more than 1 time zone 2 months before the start of the study. Subjects were right handed, non-smokers, free of sleep complaints, drugs, medication and were moderate mobile phone user (use $<$ 2 h/week, 44.1 ± 9.0 min). They had to adhere to regular bedtimes (8 h time in bed, according to scheduled bedtime in the lab) 1 week before the experimental nights and abstain from caffeine, naps, and alcohol 3 days prior to the study nights. Compliance was controlled by breath alcohol test, wrist-worn actometers and sleep logs. During the day of the study night, physical exercise and the use of mobile phones were prohibited. The Cantonal Ethic Commission in Zurich (Switzerland) approved the study and written informed consent was obtained from all participants.

11.3.2 Procedure

In a randomized, double-blind, crossover design, each subject had 2 experimental nights with EEG recordings, one of them with all-night pulse-modulated RF EMF exposure (field study). An adaptation night was scheduled prior to each experimental night. Time in

bed was 8 h for all subjects and all nights. Bedtimes were adjusted to the subject's preference and ranged from 22:00–24:00 to 06:00–08:00. For both experimental nights, subjects were trained on a motor sequence tapping task in the evening right before they went to bed. In the morning they were retested on the task to assess sleep-dependent performance improvement (e.g., [115]).

11.3.3 Exposure setup

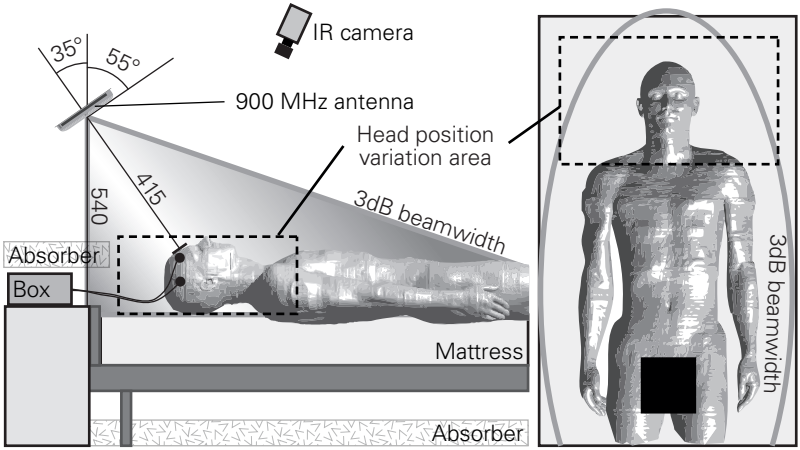

Figure 11.1: Schematic view of the exposure setup, with the Duke phantom in the reference position (lying on the back) and the circular polarized patch antenna pointing towards his forehead. A metal shielding box is protecting the EEG amplifier against electromagnetic interference, and absorbers prevent undesired reflections. The infrared camera was electrically shielded as well.

During the whole sleep episode, the subject's head was exposed to RF EMF using a circular-polarized antenna facing down toward the volunteer's forehead (see Fig. 11.1 and in Chapter 11.6 for details about the exposure setup). The 900 MHz RF signal was pulsed, with 7 consecutive 7.1 ms pulses forming one 500 ms burst. These 500 ms

bursts were repeated every 4 s (Intermittent-1 phase, 0.25 Hz, corresponding approximately to occurrence of sleep spindles), and every 1.25 s (Intermittent-2 phase, 0.8 Hz, corresponding approximately to frequency of slow oscillations), respectively. Exposure of 5 min Intermittent-1 was followed by 1 min with no exposure (OFF phase), then 5 min Intermittent-2 was followed by a 7 min OFF phase. This 18 min sequence was repeated throughout the night. The peak spatial specific absorption rate averaged over any 10 g tissue (psSAR10 g) during the 7.1 ms pulses was set to 10 W/kg. This resulted in a burst average of 1.0 W/kg. The whole night psSAR10 g averaged to 0.15 W/kg. A detailed description of the exposure setup and the dosimetric exposure assessment is given in the Supplementary material.

11.3.4 EEG recordings

EEG channels (10–20-system, F3, F4, C3, C4, P3, P4, O1, O2, A1, A2, referenced to vertex Cz), submental electromyogram (EMG) and vertical electrooculogram (EOG) were continuously recorded during the 8-h nighttime sleep period. The signals were recorded with a polygraphic amplifier Artisan (Micromed, Mogliano, Veneto, Italy), digitized at 1024 Hz (0.16–270 Hz) and transmitted via fiber- optic cables to a computer, running the software REMbrandt DataLab (Version 8.0; Embla Systems, Broomfield, CO, USA). The EEG signals were re-referenced to the mastoids (A1, A2) and filtered (0.5 Hz high-pass filter and 50 Hz low-pass filter). The sleep stages were scored for 20-s epochs according to standard criteria [117]. Artefacts were identified on a 20-s basis by visual inspection and with a semi-automatic procedure [80].

During sleep we undergo a characteristic sequence of NREM and rapid eye movement (REM) sleep with a period of approximately 90e100 min. This cyclic alternation of NREM and REM sleep is a basic feature of sleep. NREM and REM sleep episodes were defined according to standard criteria and adapted when skipped REM sleep episodes were observed (6 of 32 nights, 4 subjects). In this case, we subdivided the first cycle manually. The first 4 NREM and REM sleep episodes were analyzed. All participants had at least 4 NREM and REM sleep episodes. In each subject, the minimal common number of 20-s epochs in the 2 conditions was analyzed in each NREM and

REM sleep episode.

11.3.5 Spectral analysis

Spectral power of consecutive 20-s epochs was computed using a Fast Fourier routine (Hanning window, average of five 4 s epochs, frequency resolution 0.25 Hz). We used the C4A1 referential derivation for spectral analysis and for event-related responses because previous studies mainly found RF EMF induced effects in sleep EEG over central derivations (e.g., [79, 66, 65]). Frequencies between 0.75 and 15 Hz were analyzed. SWA was calculated as the spectral EEG power between 0.75 and 4.5 Hz. The initial REM sleep episode was only considered for analysis, when at least 3 min REM sleep occurred (n = 10). The relative decrease of SWA across night was defined as the SWA difference between the NREM episode expressing the maximal SWA and the NREM episode expressing the minimal SWA (episode number average: sham, 3.68; field, 3.5; Wilcoxon signed rank $P > 0.5$) relative to the episode with maximal SWA (sham, 1; field, 1.06; Wilcoxon signed rank $P > 0.5$).

11.3.6 Event-related spectral power (ERSP) and inter-trial coherence (ITC)

ERSP and ITC are methods of time-frequency analysis classically used to assess power (ERSP) and phase (ITC) changes across single trials time-locked to experimental events [118]. Synchronization in specific frequency bands indicates an induced activity due to an event (e.g., [119]). To establish how our specific RF EMF bursts lead to changes in EEG spectral power we performed ERSP and ITC in the NREM episode and frequency range that was significantly affected by exposure. We therefore compared ERSP and ITC of sham bursts and real Intermittent-1 phase bursts using the EEGLAB toolbox [118]. Furthermore, ERSP and ITC were calculated for the first and the second half of bursts within the significantly affected NREM sleep episode to assess the time course of the effect. Only the Intermittent-1 phase bursts provided enough data (4 s between bursts) to perform this analysis. For both conditions, only bursts during artifact-free epochs of

the 4th NREM sleep episode were included in the analysis (referential derivation C4A1).

ERSP is an analysis that calculates the EEG power spectrum (short-time Fourier transform using 185 Hanning windows of 1024 data points (1 s)) time-locked to the RF EMF bursts. This time course of EEG power is next averaged across all RF EMF bursts [118, 120]. ITC, also termed "phase-locking factor" [121], quantifies the phase consistency of activity in a specific frequency range across single trials time-locked to a stimulus, i.e., the RF EMF bursts. Thus, the higher the ITC value the higher is the synchronization between EEG data and the time-locking RF EMF bursts (i.e., EEG phase reproducibility across trials at a given latency; [118, 122]). We used the same window parameters as for the ERSP analysis.

The EEG signal was band pass-filtered (0.5e5 Hz). Thereafter, the ERSP and ITC were calculated for the first 3500 ms after the bursts for the frequency range between 1 and 4 Hz (1-Hz resolution). Only artifact-free trials were included. Since we could not use a pre-event baseline (baseline was affected by bursts itself), we compared the ERSP and ITC between RF EMF bursts and sham bursts (trigger signal at similar time points as RF EMF bursts during the sham night) to asses RF EMF induced power and phase-locking changes.

11.3.7 Motor performance

A finger sequence tapping task before and after sleep was performed to assess motor performance. This task was adapted from Walker et al. [115]. Parallel versions were used in a balanced and randomized order for the 2 experimental sessions. This task required subjects to repeatedly complete, with their left hand, a five-element sequence (sequence 4–3–2–1–4 or 2–3–1–4–2; 1 is the digit finger) as fast and accurately as possible on a keyboard.

The training before sleep consisted of twelve 30-s trials with 30-s breaks between the trials. During retest they performed 3 30-s trials interspersed with 30-s breaks. The sequence was continuously presented on the screen to prevent a working memory component and no feedback on pressing keys or about their performance was given. A keyboard (DirectIN keyboard, Empirisoft, New York) with a millisecond accuracy to measure response times (RT) between key-presses

was used. Performance improvement in motor tasks are reflected in an increase of speed and a decrease of variability. Earlier studies exclusively investigated speed (as assessed by number of correct key-presses per time or mean RT) to investigate the consolidating role of sleep on performance (e.g., [115]). However, more recent studies question this sleep-dependent improvement in speed because it is also seen after 5 min wake and may depend on a decrease in fatigue [123, 124]. We therefore focused on the variability of the RT between key-presses to assess sleep-dependent performance improvement since there is evidence that sleep might reduce variability in a motor task [110]. Moreover, such a decrease of variability due to sleep in a visuomotor adaptation task seems to be closely related to sleep SWA [110]. This study further showed that additional learning after a training session did not improve variability, but a night of sleep did. We calculated the variance of RT to assess variability between the correct key-presses for each trial. Post-training performance was defined as the mean of the last 2 trials in the training session and retrieval performance as the mean of the first 2 trials during retest according to literature (e.g., [115]). Sleep-dependent performance improvement of variability was specified by the relative difference between the evening post-training and morning retrieval performance (%, [(retrieval performance - post-training performance)/ post-training performance]).

To exclude possible confounding effects on performance we compared different subjective measures for both conditions. To do so, prior to each motor learning task subjects were asked about their alertness and mood (assessed by a 6 item visual analog scale) and in the morning subjective sleep quality was assessed by a questionnaire. Subjects' answers did not differ between the conditions (all $P > 0.15$). Subjects did not perceive the field since their answers were below chance level.

11.3.8 Statistics

Spectral power changes were analyzed using 2-way repeated- measures ANOVA with the 2 within subject factors 'condition' (field vs. sham) and 'sleep episode' (1st–4th NREM sleep episode). Absolute EEG spectral power data was log transformed prior to testing to approximate normal distribution. To quantify differences in the SWA

time course between field and sham condition post hoc 2-tailed paired t-test were applied.

The difference in the ERSP and ITC in the SWA range between the field exposure and sham night was obtained using 2-tailed paired t-tests for each time point after the pulse. Sleep-dependent performance improvement difference between the 2 conditions was analyzed with a repeated-measures analysis of covariance (ANCOVA) with the factor condition (field vs. sham) covarying for post-training performance difference (baseline difference). Correlations of performance and SWA were obtained using Pearson correlation.

11.4 Results

11.4.1 Minor effects of RF EMF exposure on sleep architecture

In a first step, we quantified the RF EMF effects on sleep architecture (see Table 11.1). Only minor changes were observed. Subjects during exposure showed a 2.1% decrease of total sleep time (-9.23 ± 3.40 min, mean ± SEM; t = -2.31, P = 0.04) and, as a consequence, exhibited reduced sleep efficiency (-1.92 ± 0.83%; t = -2.31, P = 0.04). This reduction was primarily due to an increase of wake after sleep onset (6.63 ± 2.60 min; t = 2.55, P = 0.03). NREM and REM sleep episode duration did not differ between the 2 conditions (all P > 0.1).

11.4.2 RF EMF changed EEG spectral power during NREM sleep

Field exposure induced an NREM sleep episode specific increase in spectral power in the low-frequency range. Frequencies up to 10 Hz were affected by exposure (Fig. 11.2). Looking at the relative change (% increase), the strongest effects were observed in the SWA frequency range. Thus, for further analysis we focused on SWA since it also reflects the major characteristic of deep NREM sleep, which was shown to be related to sleep-dependent performance changes [109, 110, 125]. Characteristically, SWA decreases in the course of sleep, reflecting the recuperative function of sleep [112]. To assess changes in the

Sleep variables	Condition Sham	Field
Total Sleep Time (min)	448.4 ± 2.7	439.2 ± 4.9*
Sleep latency (min)	9.0 ± 1.3	9.2 ± 1.5
Wake after Sleep onset (min)	7.0 ± 1.1	13.6 ± 1.1*
Sleep efficiency (%)	93.4 ± 0.6	91.5 ± 1.0*
Stage 1 (min)	18.7 ± 2.2	21.0 ± 3.5
Stage 2 (min)	170.2 ± 8.1	171.0 ± 7.8
Stage 3 (min)	161.3 ± 9.0	154.9 ± 8.3
REM sleep (min)	116.9 ± 4.0	113.0 ± 4.8

Table 11.1: Values in mean ±SEM. REM sleep: Rapid eye movement sleep. Total sleep time: total amount of NREM (Stage 2 and Stage 3) and REM sleep. Sleep latency: latency to the first occurrence of stage 2 sleep. Sleep efficiency: Total sleep time expressed as a percentage of time in bed (8 h). Paired t-tests revealed significant differences as indicated by stars ($p < 0.05$). Field: exposure to intermittent bursts of RF EMF. Sham: no field applied.

time course of SWA, we calculated average SWA in each NREM sleep episode. During both conditions SWA decreased in the course of the night. However, we found higher SWA in the 4th NREM sleep episode compared to the sham exposure ($P < 0.05$, Fig. 11.3) and thus, the decrease of SWA from the 1st to the 4th NREM sleep episode tended to be less pronounced during exposure ($P = 0.07$). No other NREM or REM sleep episodes revealed significant differences between the conditions (all $P > 0.25$).

11.4.3 Induction of SWA by pulsed RF EMF

Given this SWA enhancement toward the end of sleep, we further analyzed the EEG of the 4th NREM sleep episode during exposure to test whether single RF EMF bursts may lead to an event-related response in the SWA range. Thus, we investigated whether the increase in SWA is related to phase-locking, i.e., reflected in ITC, or amplitude changes, i.e., reflected in ERSP. RF EMF bursts increased ERSP in the SWA frequency range for several time points in the inter-burst in-

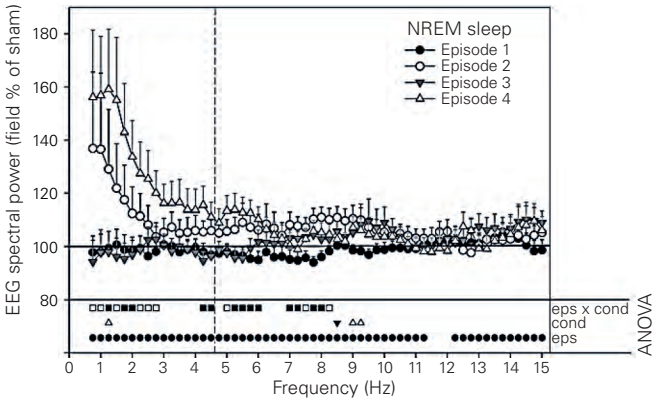

Figure 11.2: EEG power density of the field night as a percentage of the sham night (100%, solid black horizontal line) for the first 4 NREM sleep episodes (mean + SEM). Frequencies were analyzed between 0.75 and 15 Hz (0.25 Hz resolution). Lower panel of the figure shows results of the 2-way repeated-measures ANOVA (episode [eps]: 1st–4th NREM episode; condition [cond]: field vs. sham and their interaction [eps × cond]). Filled black symbols in the lower panel indicate significance ($P < 0.05$) and open symbols trends ($P < 0.1$). Vertical gray dashed line delineates the end of the SWA range (0.75–4.5 Hz). Post hoc paired t-test revealed significant differences in the SWA range bins only for the 4th NREM sleep episode.

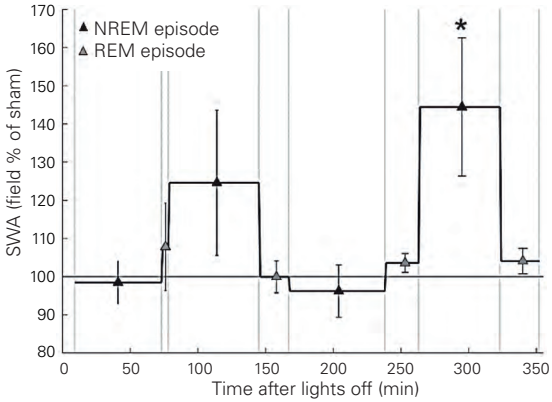

Figure 11.3: Time course of slow-wave activity (SWA; 0.75–4.5 Hz) during RF EMF exposure as a percentage of the corresponding sham condition for the first 4 NREM and REM sleep episodes (n = 16, mean ± SEM). Black and gray triangles indicate NREM and REM sleep episodes, respectively. Gray vertical lines delineate the average beginning and end of NREM and REM sleep episodes. The first REM sleep episode includes data of 10 subjects only. The star indicates a significant difference between sham and field exposure ($P < 0.05$, paired t-test).

terval mainly for the first half of the bursts (Fig. 11.4A). In addition, we found that RF EMF bursts increased phase-locking of the EEG signal in the SWA frequency range at around 2300–2500 ms after the burst both, in the first and second half of the bursts (Fig. 11.4B). These findings suggest an RF EMF burst-related increased phase-locking and synchronization in the SWA range in specific time windows after the RF EMF bursts and therefore indicate an induction of SWA due to pulsed RF EMF exposure. SWA in NREM sleep episodes 1–3 did not show a significant increase in ERSP and ITC after RF EMF bursts.

11.4.4 RF EMF exposure affected sleep-dependent motor performance improvement

Subjects significantly improved their performance quality, as assessed by the reduced variance of the RT, from evening to morning during sham ($49.04 \pm 6.40\%$ reduction, $P < 0.05$) and exposure ($28.97 \pm 10.69\%$, $P < 0.02$). The baseline values in the evening did not differ between the field and sham condition (field: 24,270.3 ms $\pm$ 7166.9 ms; sham: 23,581.8 ms $\pm$ 6414.3 ms; $P > 0.8$). Thus, learning was comparable between the 2 conditions. However, sleep-dependent performance improvement was reduced during exposure compared to the sham condition ($-20.08 \pm 10.57\%$, Greenhouse–Geisser $F = 5.76$, $P = 0.03$). In a next step, we explored the relationship between the recuperative function of sleep, as measured by the decrease of SWA across the night, and sleep-dependent performance improvement. We found a positive correlation between the sleep-dependent performance improvement (variance of RT) and the decrease of SWA during the sham night ($r = 0.63$, $P < 0.01$). No significant correlation was present during the exposure night ($r = 0.27$, $P > 0.3$). To test whether the increased SWA in the 4th NREM sleep episode observed under field exposure might be related to the reduced sleep-dependent performance improvement we correlated SWA in the 4th NREM sleep episode with post-sleep performance improvement. This analysis showed that indeed higher SWA in the 4th NREM sleep episode was related to a reduced sleep-dependent performance improvement in RT variance ($r = -0.59$, $P = 0.02$) in the sham condition. Again, no significant correlation was observed for the active field condition ($r = -0.21$, $P > 0.4$). Moreover, we found

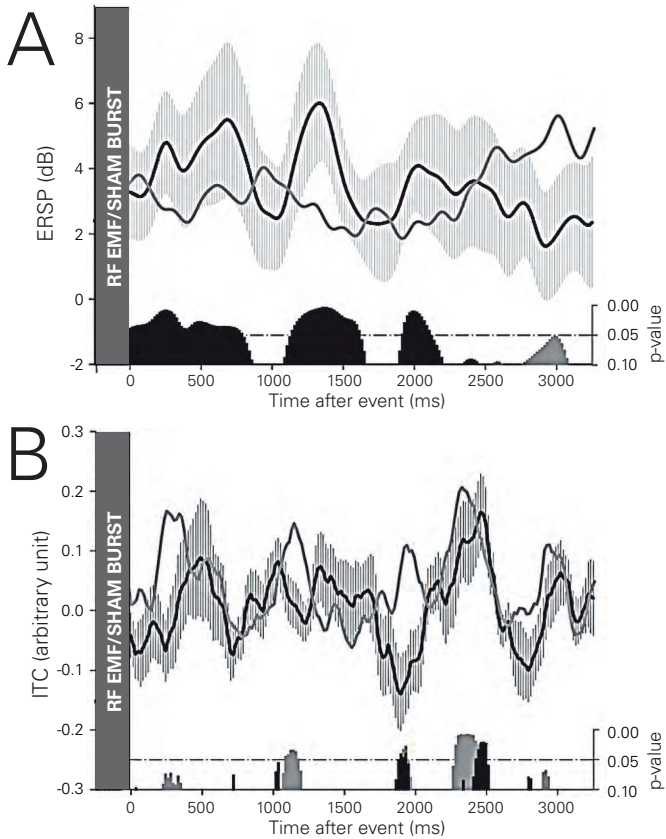

Figure 11.4: Event-related responses (ERSP and ITC) in the SWA frequency range during exposure compared to sham in the 4th NREM sleep episode. 'Event' indicates RF EMF bursts (field) or a corresponding trigger burst during the sham condition. Horizontal lines indicate the mean event-related response differences between the field and sham condition in the SWA frequency range (1–4 Hz) for the first half (black line) and second half of the bursts (gray line). Error bars indicate SEM of the first half of the bursts. Bars in the lower (statistic) panels illustrate P-values ($\leq$0.1, black: first half of bursts, gray: second half of bursts). (A) Time course of the event-related spectral power (ERSP) after RF EMF bursts relative to sham bursts. (B) Time course of the inter-trial coherence (ITC, phase-locking) after RF EMF bursts relative to sham bursts.

a trend that a larger increase of SWA from sham to field condition in the 4th NREM sleep episode was reflected in a larger reduction of sleep-dependent performance improvement from the sham to the field condition (r = 0.47, P = 0.07).

11.5 Discussion

In this study, we showed that very-low-frequency pulse- modulated RF EMF exposure resulted in increased SWA towards the end of the sleep period and reduced sleep-dependent motor performance improvement. Furthermore, we provide first evidence that the increased SWA results from a direct induction of sleep slow waves by RF EMF pulses.

Our data support the notion that changes in EEG activity during sleep due to RF EMF exposure are among the most robust effects EMF have on biological systems [95]. RF EMF exposure resulted in increased SWA compared to the sham condition. However, most previous studies reported effects in the spindle frequency range [79, 80, 68, 82, 66, 65]. A possible explanation comes from a dose response study showing that pulsed RF EMF with average SAR levels equal or lower than 0.2 W/kg were not sufficient to significantly increase spindle activity in the sleep EEG [82], whereas exposure at SAR levels equal or above 1 W/kg showed a significant increase (e.g., 1, 4). Our average all-night SAR value was 0.15 W/kg, and the relevant 6 min average never exceeded 0.34 W/kg, and therefore, might be below the intensity that would lead to a significant increase in spindle activity. A recent study showing increased SWA during NREM sleep after 2-Hz pulse-modulated RF EMF exposure suggests that a prominent or principal pulse modulation in the delta range (<5 Hz) of the RF EMF might be needed to induce an increase in SWA during sleep [66]. Our bursts were presented in this low- frequency range (0.25/0.8 Hz).

We provide first evidence that single RF EMF bursts may affect sleep EEG activity by induction of SWA. However, potential mechanisms explaining how these fields may induce SWA are so far unknown. Using a special intermittent pulse modulation design of the RF EMF exposure we demonstrated that single RF EMF bursts may directly change EEG activity in the SWA range. This was demonstrated by the increased ERSP and by the increased phase coherence (ITC) in

the SWA range after the RF EMF bursts. The results show that the effect in ERSP is most pronounced during the first half of the bursts and that significant effects in the ERSP and ITC are seen particularly during early time points during the inter-burst interval. We do see also late ERSP and ITC changes for which we have no good explanation. Our results suggest that RF EMF may be capable to directly induce or entrain EEG activity during sleep.

The question arises why the SWA increase was only significant toward the end of sleep. There is evidence that applied weak electrical fields can entrain spiking activity of neurons and synchronize them [126]. Thus our RF EMF may also entrain and synchronize neuronal activity in the SWA range. We have good evidence that the level of neuronal synchronization is a key feature determining the amplitude of slow waves, i.e., the level of SWA [127]. Thus, an entrainment of ongoing activity by field expo- sure may rely on a similar mechanistic explanation for the changes in SWA. At the beginning of the sleep period, neurons are almost perfectly synchronized, which is reflected in high values of SWA [128]. Thus, it seems to be plausible that at the beginning of sleep a weak RF EMF may not be able to further enhance synchronization of neural activity. However, toward the end of the sleep period the level of synchronization decreases [128] allowing RF EMF to exert their capability to enhance synchronization. A similar explanation may apply for our observation that increased ERSP in the SWA frequency range is most pronounced in the first half of the bursts. It is established that SWA shows a gradual build up during the initial phase of each NREM sleep episode [129] and as a result average SWA is at a lower level during the first half of the episode. Considering that the field may increase neuronal synchronization especially when SWA is less pronounced, we would expect a stronger effect on ESRP during this initial phase.

An ultimate cellular mechanism explaining this synchronization still remains elusive. Among others, we see 2 candidate mechanisms. First, inducing an event-related brain response may suggest that there is a receptor or an unknown human sensor that perceives RF EMF and causes oscillatory brain activity when exposed to such fields [130]. The second candidate mechanism is based on recent findings of Anastassiou et al. [131]. They introduce the concept of non-synaptic or ephaptic coupling of cortical neurons. In other words, EMF develops outside

of neurons due to neuronal activity. These fields are not just a mere epiphenomenon of neuronal activity, but rather feedback onto neuronal activity. Even though these fields are very weak, they were able to strongly entrain and synchronize the spike-timing of the neurons. Considering that small changes of these endogenous fields could affect neuronal functioning, further investigations should explore whether pulse-modulated RF EMF interact with these endogenous fields.

Both candidate mechanisms might lead to changes in SWA as they are not mutually exclusive. Additional studies are needed to explore such fundamental mechanisms for brain functioning. Our study shows that RF EMF can be used to explore such mechanisms. An interesting example for the usefulness of RF EMF expo- sure to study brain function is provided by our observation that the induced SWA is related to reduced sleep-dependent performance improvement.

Increasing evidence shows that SWA during NREM sleep is critically involved in the regulation of cortical excitability and synaptic strength across 24 h [128, 132]. Thus, during waking cortical excitability increases through synaptic potentiation. During sleep a reduction of synaptic strength takes place, normalizing the increase in excitability observed during the day [128, 132, 133]. This reduction of synaptic strength is mirrored in SWA [132]. Therefore, the changes in the time course of SWA during the field night may reflect an interference of RF EMF with the normalization of cortical excitability during sleep. Consistent with previous research, low- frequency pulse-modulated RF EMF may affect cortical excitability [134]. Following field exposure Ferreri et al. [134] found increased intracortical facilitation measured with a paired pulse transcranial magnetic stimulation paradigm. This is up to now the most direct evidence that pulse-modulated RF EMF may directly affect cortical plasticity. There is evidence that slow waves might also causally affect and not just reflect synaptic strength[135]. Thus, the altered time course of SWA may result in an imbalance in the regulation of synaptic strength. The renormalization of synaptic strength during sleep showed beneficial effects of motor performance [110]. Since sleep-dependent improvement of motor performance was reduced under RF EMF exposure, our behavioral data further support the suggestion of an imbalance in the regulation of synaptic strength. We confirmed this finding since the decrease of SWA across the sham night correlated with sleep-

dependent performance improvement. Thus, the more SWA in the 4th NREM sleep episode was increased during RF EMF exposure the more tended sleep-dependent performance improvement to deteriorate. Taken together, our findings suggest that the interaction of pulsed RF EMF with the regulation of synaptic strength may explain our behavioral results. We performed a single exposure and thus cannot exclude adaptation effects. As a consequence we can- not state anything about long-term effects. The large interindividual differences within our well-defined subject population clearly showed that our results cannot be generalized e other subpopulations may show opposite effects. Further studies are needed to investigate the cause of such large interindividual differences.

In summary, our study showed that RF EMF may directly affect ongoing brain activity during sleep, and as a consequence alter sleep-dependent performance improvement. RF EMF may there- fore represent a non-invasive stimulation tool that is not consciously perceived for the manipulation of brain activity to study basic mechanisms of sleep and wake regulation, and performance behavior and may lead in the future to new therapeutic approaches.

11.6 Supplementary Materials

11.6.1 Exposure Setup

The exposure system was designed and optimized for best uniformity in exposing the volunteer's head, while allowing different sleep postures and positions. This was achieved using a circular polarized, directional antenna at 900 MHz with a 3 dB beam width of 70° (SPA-915/70/8/0/RCP, Huber+Suhner, Herisau, Switzerland), mounted on the wall at a height of 490 mm above the mattress, facing down towards the volunteer's head (55° angle from the wall, 415 mm nominal distance between antenna and head for the reference position, Fig. 11.1). The exposure system was fully computer controlled, enabling a double-blind protocol and continuous measurement, monitoring and logging of the radiated power.

The conductive EEG leads reflect the RF EMF when the leads are parallel and are largely invisible when leads are normal to the incident

E-field. Hence, the variability of the head exposure caused by the lead orientation has been reduced by applying the circular-polarized field. Furthermore, electrode leads were braid into a net to keep them in a fixed position relative to the head. The EEG amplifier box was shielded from electromagnetic interference with two layers of enclosing metal. EEG leads and other connecting cables were fed through π-filters. This resulted in a > 75 dB suppression of the 900 MHz coupling into the EEG signals, such that the RF signal was not visually detectable in the EEG.

11.6.2 Dosimetric Evaluation

The dosimetric exposure assessment was performed with SEMCAD X V14.4 (Speag, Zurich, Switzerland) using the anatomical human models Ella, Duke, and Louis [35]. For the standard reference position with Duke (Fig. 11.1), 1 W forward power at the antenna feed point caused a peak spatial specific absorption rate averaged over any 10 g tissue (psSAR10g) of 0.051 W/kg in the whole head. Normalized to 1 W/kg psSAR10g (19.6 W forward power), this results in psSAR1g and average-SAR ($\pm$SD) of 2.25 $\pm$ 0.19 W/kg (136%) for the whole head, and 0.77 $\pm$ 0.18 W/kg (77%) for the brain without cerebro spinal fluid. The uncertainty (SD, k=1) for the evaluation without EEG electrodes stayed below 14% (psSAR1g) and 6% (average-SAR). The effect of the electrodes remains localized. Recent studies [97, 98] indicate no influence on whole head average SAR, a maximum change of 20% in psSAR10g, and 46% uncertainty for psSAR1g in worst-case positioning. This results in an overall psSAR1g uncertainty of 48%.

The variation analysis included: (a) three different anatomical heads, (b) head sizes $\pm$10%, (c) dielectric parameters $\pm$10%, and (d) different sleep postures and positions of the volunteers, which have been evaluated based on whole night surveillance videos. The following worst-case positions have been identified: (d1) head positions of $\pm$ 90 mm in head-feet axis and $\pm$ 250 mm left-right shifting, (d2) 45° head tilting, (d3) 90° head rotation, (d4) combinations of (d1-d3). The combined exposure variation is estimated to be 40% in psSAR1g and 15% in average-SAR (SD, k=1). Compared to the reference position with Duke, worst-case variations came from sleep postures and positions ranging from -54% to +34% in psSAR1g, and from -9% to

+19% in average-SAR.

11.6.3 Exposure Condition

The 900 MHz RF signal was pulsed, with seven consecutive 7.14 ms pulses forming one 500 ms burst (64.3 ms pause after each pulse). These 500 ms bursts were repeated every 4 s (Intermittent-1 phase, 0.25Hz), and every 1.25 s (Intermittent-2 phase, 0.8Hz), respectively. Exposure of 5 min Intermittent-1 was followed by 1 min without exposure (OFF phase), then 5 min Intermittent-2 was followed by a 7 min OFF phase. This 18 min sequence was repeated throughout the night. The psSAR10g during the 7.1 ms pulses was set to 10 W/kg (196 W peak forward power). This resulted in a 500-ms burst average of 1.0 W/kg, an Intermittent-1 average of 0.125 W/kg, and an Intermittent-2 average of 0.4 W/kg. The whole night psSAR10g averaged to 0.15 W/kg, while the relevant 6 min average never exceeded 0.34 W/kg, staying well below the exposure limit of 2 W/kg for the general public [1], even when assuming a 20% increase due to the influence of EEG leads.

Chapter 12

Outlook

12.1 Current Status of EMF Sleep Research

There is an accumulating body of evidence that EMFs interact with brain physiology [62, 63, 64, 65, 66, 67, 68, 69]. However, there are many contradictions and inconsistancies. The effect on EEG power density, e.g., occurs occasionally in different frequency-bands and in different sleep episodes. Effects on cognitive function render a rather inconsistent overall picture [82]. Hence, final conclusion remain premature, except for the effect-magnitude, which may be considered relatively small, e.g., below the effect of caffeine on EEG spectral density [136].

12.2 Interaction Mechanisms

Regarding the vast complexity of our central nervous system, there are many potential interaction mechanisms between EMF and brain physiology. Various measures have been taken to avoid confounding factors, such as the acoustic perception of RF transmission [103, 65] via battery currents or loudspeaker behavior of antennas, or the localized RF-induced temperature ripples around EEG electrodes (see Chapter 10). And yet, a robust EMF effect still remains elusive.

Proposed interaction mechanisms range from small-scale thermoplastic expansions and ephaptic coupling of cortical neurons, i.e., non-synaptic neuron interaction [76], to some sort of obscure resonant sensory perception of EMF within the CNS.

The intrinsic problem in safety assessments of non-thermal EMF exposure levels persists: the field level cannot be increased without increasing the thermal load. While the levels of chemical toxins can be increased until a clear effect is established, higher EMF will ultimately cause higher temperatures and, thus, lead to a thermal effect. Carrier frequencies below 1 MHz clearly have non-thermal effects, e.g., nerve stimulation in the kHz region. MRI and mobile phone RF frequency bands, however, exhibit the only established and sufficiently explained non-thermal effect of microwave hearing, which is due to thermoelastic expansion rather than temperature alone [137]. Other reported effects such as pearl chaining [100] are non-thermal in suspended particles, but seem to require thermally relevant high levels of EMF in biological tissues. One could, therefore, justifiably ask whether the observed effects on EEG spectral power could be elicited by the small temperature changes in the range of $< 0.6°C$, potentially via thermoplastic expansion through the pulsed RF fields.

12.3 Future Research

The challenge from a biomedical engineering perspective is to further reduce the overall exposure uncertainties, as well as to provide innovative exposure modalities. A rigorous double-blind protocol that includes full RF shielding of the recording equipment (EEG amplifier, monitoring cameras, etc.) and inhibition of any conscious field perception by the volunteer or operator (acoustic signals, heating, microwave hearing) must be maintained.

For future human provocation studies with EMF, I envision mainly the following topics where improvements are desirable or necessary.

- Exposure Signal:
  - frequency components of modulation envelope:
    there is increasing evidence that specific modulation frequency components may elicit observed effects [65, 138]

  - high peak field levels (large PAR signals):
    the CNS may be more susceptible to peak fields levels, rather than average levels

- Sites of interaction
  - penetration depth of RF can be varied by adjusting the carrier frequency, as certain specific structures may be more involved than others, e.g., thalamus vs. cortex
  - antenna design and distance can define the area of maximum exposure

- Further elimination potential confounders
  - acoustic perceptions of RF components needs to be suppressed by a defined background noise level
  - the effects of metallic objects at the head, e.g., EEG electrodes, need to be investigated for each study configuration

- Alternative assessment of brain physiology
  - EEG and PET have been used in many studies
  - MRI may not be ideal, as there already are very high levels of EMF present
  - a study in which magnetoencephalography (MEG) is used may reveal EMF effects in subcortical areas such as the thalamus

Part III

Epilogue

Chapter 13

Conclusions

The objectives of this thesis were achieved: Various safety aspects of human exposure to radio frequency (RF) electromagnetic fields (EMF) are addressed. Electrothermal investigations of high RF induced fields (MRI), as well as for low exposure levels (human provocation studies) have significantly enhanced knowledge and state-of-the-art methodologies for safety assessment of EMF.

A profound insight into MRI-specific exposure schemes has been elaborated by means of a large number of scan scenarios of various anatomical human models in many imaging positions. The results help us to understand MRI-specific RF absorption mechanisms in terms of whole-body and localized energy deposition, and subsequent thermal loading. By including the human thermoregulatory responses, the key parameters for potentially dangerous scan scenarios could be identified. Many MRI operators still attempt to solve temperature issues by increasing ventilation during the scan (audience question during platform presentation at ISMRM 2012 in Melbourne, Australia, [139]). While ventilation and sweating play a major role in overall heat dissipation, local internal hotspots in MR imaging almost entirely depend on local thermoregulation [21, 45].

As thermal dose — in combination with tissue-specific thresholds — appears to be the best proxy for actual tissue damage [24], the linking of MR exposures to thermal dose evaluation may open a new

era for safety standards in upcoming MR scanner generations.

Various issues in hypothesis-driven research on acute effects of human mobile phone exposures have been addressed within this thesis. Novel exposure systems that foster innovative research on EMF effects, including different RF frequencies, ELF magnetic field exposures, and all–night exposure with circularly polarized fields, have been developed and presented. The impact of potential confounders has been investigated, and appropriate measures were taken to avoid any perception of the EMF condition by the volunteer or operator. An actual sleep study in collaboration with the University Children's Hospital Zurich revealed changes in EEG slow-wave activity and effects on sleep-dependent performance improvement after overnight RF EMF exposure.

As direct dosimetric measurements in humans are challenging or not feasible, the usage of numerical electrothermal models — as described in this thesis — is particularly important to predict the complex interactions of EMF with biological tissues. Validations of simulation results can be obtained 1) invasively, in case of medical indication, e.g., in hyperthermia cancer treatment; 2) indirectly via non-invasive temperature measurements as described in this thesis; or 3) with an MRI thermometry approach. However, these validation measurements cannot replace numerical predictions. Subsequently, future advances in the research field of EMF safety are subjected to the progress in the following areas (non-exhaustive collection):

- High quality anatomical human models for simulation studies
  - representative for the entire population in terms of age, stature, ethnic group, and gender
  - pregnant models in different periods of gestation
  - improved resolution and anatomical details
- Electrothermal model input parameter
  - further investigation of dielectric and thermal properties of living human tissues, including a high level of public availability [17, 16]

  - assessment of human local thermoregulation capabilities, including estimations of the lower bounds for pathologic cases (e.g., diabetics, the elderly)
  - establishing better thermoregulation models
- Electromagnetic simulation and measurement tools
  - hardware accelerated electrothermal simulation platforms with advanced parametrized evaluation tools
  - time-domain RF probes for effective characterization of exposure patterns
- Laboratory research in vitro, in vivo, and in human
  - innovative assessments of immediate responses to EMF
  - establishing hypotheses on EMF interaction
- Epidemiological studies
  - monitoring of potential correlations of EMF and adverse health conditions
  - exposure assessment and modeling for different population groups
- MRI techniques
  - advances in MRI thermometry for future validation concepts or safety implementations
  - indirect exposure assessment via B1+ mapping

Study results shall be made available to the maintenance consortiums of the according product or safety standards, e.g., ICNIRP, IEC, and IEEE [3, 1, 2]. Monitoring of new evidence-based data will allow updating of these guidelines wherever necessary. Currently, the standards do not consider exposure time, or they only rudimentarily include overall dosage. As tissue damage is associated with exposure level and time, i.e., with thermal dose, a revision is recommended.

Overall, the complex and to some extent counter-intuitive absorption mechanisms of non-ionizing radiation form a very interesting field

of research. The inclusion of biology fosters fascinating interdisciplinary studies. Our project partners have a broad spectrum of scientific backgrounds: engineers and physicists; medical doctors, toxicologists, biologists, epidemiologists and neuropsychologists; regulatory offices and standard building bodies. As the societal debate about adverse health effects from "electro-smog" is ongoing, the media and politics have a broad interest as well.

The work performed within this thesis was funded by two research project conglomerations: the international EURKA/CTI project "MRI+", and the Swiss National Research Project "NFP57". The sleep study was generously supported by "Forschungsstiftung Mobilkommunikation".

In summary, significant contributions regarding the safe application of EMF in both everyday life exposures as well as in the clinical environment within MRI scanners are presented in this thesis. Most results presented here have been published in journals and conference proceedings, ensuring broad dissemination to other researchers, standards building bodies, and regulatory offices.

Part IV

Appendix

Appendix A

List of Acronyms

BMI	Body Mass Index
CAD	Computer Aided Design
CW	Continuous Wave
DASY	Dosimetric Assessment System (SPEAG)
DAQ	Data Acquisition
EASY	Exposure Acquisition System (SPEAG)
EM	Electromagnetic
EMF	Electromagnetic Field
ETHZ	Eidgenössische Technische Hochschule Zürich
FDTD	Finite-Difference Time-Domain
FSE	Fast Spin Echo
GSM	Global System for Mobile Communications
ICNIRP	International Commission on Non-Ionizing Radiation Protection
IEC	International Electrotechnical Commission
IEEE	Institute of Electrical and Electronics Engineers
IT'IS	IT'IS Foundation for Information Technologies in Society
MRI	Magnetic Resonance Imaging
RF	Radio Frequency
RMS	Root Mean Square
SAM	Specific Anthropomorphic Mannequin
SAR	Specific Absorption Rate

SEMCAD	Simulation Platform for Electromagnetic Compatibility Antenna Design and Dosimetry (SPEAG)
SPEAG	Schmid & Partner Engineering AG
TSE	Turbo Spin Echo
UMTS	Universal Mobile Telecommunications System

Appendix B

List of Symbols

Symbol	Quantity	Unit
E	Electric field	V/m
H	Magnetic field	A/m
B	Magnetic flux density	T
ΔT	Temperature increase	K
$\overline{\varepsilon}$	Complex permittivity $\overline{\varepsilon} = \varepsilon_0 \cdot \overline{\varepsilon_r}$	F/m
σ	Conductivity	S/m
c	Specific heat capacity	$J/(kgK)$
ρ	Mass density	kg/m^3
SAR	Specific absorption rate	W/kg
$psSAR1g$	peak SAR spatially averaged over 1 g	W/kg
$psSAR10g$	peak SAR spatially averaged over 10 g	W/kg
$wbSAR$	SAR spatially averaged over the whole body	W/kg

Appendix C

List of Publications

C.1 Journal Publications Included in this Thesis

Within the framework of this thesis, the following scientific publications have been written by the author.

(1) Murbach M, Cabot E, Neufeld E, Gosselin MC, Christ A, and Kuster N. Local SAR enhancements in anatomically correct children and adult models as a function of position within 1.5 T MR body coil. *Progress in Biophysics and Molecular Biology*, 107(3):428–433, 2011.

(2) Murbach M, Christopoulou M, Crespo-Valero P, Achermann P, and Kuster N. Exposure system to study hypotheses of ELF and RF electromagnetic field interactions of mobile phones with the central nervous system. *Bioelectromagnetics*, 33(6):527–533, 2012.

(3) Murbach M, Neufeld E, Kainz W, Pruessmann KP, and Kuster N. Whole-body and local RF absorption in human models as a function of anatomy and position within 1.5T MR body coil. *Magnetic Resonance in Medicine*, (published online ahead of print), 2013.

(4) Murbach M, Neufeld E, Capstick M, Kainz W, Brunner DO, Samaras T, Pruessmann KP, and Kuster N. Thermal tissue

damage model analyzed for different hole-body SAR and scan durations for standard MR body coils. *Magnetic Resonance in Medicine*, (published online ahead of print), 2013.

(5) Murbach M, Neufeld E, Christopoulou M, Achermann P, and Kuster N. Evaluation of electrode artifacts and thermal ripples of EEG RF experiments. *Bioelectromagnetics*, submitted, 2013.

(6) Lustenberger C, Murbach M, Dürr R, Schmid MR, Kuster N, Achermann P, and Huber R. Stimulation of the brain with radiofrequency electromagnetic field pulses affects sleep-dependent performance improvement. *Brain Stimulation*, (published online ahead of print), 2013.

C.2 Other Journal Publications

In addition, the author has co-authored the following journal publications.

(1) Loughran S, Benz D, Schmid MR, Murbach M, Kuster N, and Achermann P. No increased sensitivity in brain activity of adolescents exposed to mobile phone-like emissions. *Clinical Neurophysiology*, (published online ahead of print), 2013.

(2) Neufeld E, Gosselin MC, Murbach M, Christ A, Cabot E, and Kuster N. Analysis of the local worst-case SAR exposure caused by an MRI multi-transmit body coil in anatomical models of the human body. *Physics in Medicine and Biology*, 56(15):4649–4659, 2011.

(3) Schmid MR, Loughran SP, Regel SJ, Murbach M, Bratic Grunauer A, Rusterholz T, Bersagliere A, Kuster N, and Achermann P. Sleep EEG alterations: effects of different pulse-modulated radio frequency electromagnetic fields. *Journal of Sleep Research*, 21(1):50–58, 2012.

(4) Schmid MR, Murbach M, Lustenberger C, Maire M, Kuster N, Achermann P, and Loughran SP. Sleep EEG alterations: effects of pulsed magnetic fields versus pulse-modulated radio frequency

electromagnetic fields. *Journal of Sleep Research*, 21(6):620–629, 2012.

(5) Waldmann P, Bohnenberger S, Greinert R, Hermann-Then B, Heselich A, Klug SJ, Koenig J, Kuhr K, Kuster N, Merker M, Murbach M, Pollet D, Schadenboeck W, Scheidemann-Wesp U, Schwab B, Volkmer B, Weyer V, and Blettner M. Influence of GSM signals on human peripheral lymphocytes: study of genotoxicity. *Radiation Research*, (published online ahead of print), 2013.

(6) Xu S, Chen G, Chen C, Sun C, Zhang D, Murbach M, Kuster N, Zeng Q, and Xu Z. Cell type-dependent induction of DNA damage by 1800 MHz radiofrequency electromagnetic fields does not result in significant cellular dysfunctions. *PLoS ONE*, 8(1):e54906, 2013.

C.3 Other Publications

The author has presented or co-authored various other publications.

(1) Murbach M, Neufeld E, Gosselin MC, Christ A, Cabot E, and Kuster N. Local SAR vs. Whole Body SAR, and in vivo validation in an MR environment. Presentation at the 2011 Thermal Workshop on RF Hotspots, Zurich, Switzerland, March 21–22, 2011, 2011. Presentation in Session 2: SAR and Temperature Modeling.

(2) Murbach M, Neufeld E, Gosselin MC, Christ A, Cabot E, and Kuster N. Temperature, incident field and b1+ comparison in MR simulation and measurement, using a detailed anatomical model. Presentation at the 10th International Conference of the European Bioelectromagnetics Association (EBEA 2011), Rome, Italy, February 21–24, 2011, 2011. Presentation in session: Dosimetry (February 23, mmu).

(3) Murbach M, Kühn S, Christ A, and Kuster N. Effects of pulse-modulated radio frequency electromagnetic fields on the human

brain: Critical field parameters, site of interaction and sensitivity in early adolescence. Presentation at the NRP 57 (Non-Ionising Radiation – Health and Environment) Final Workshop, Zurich, Switzerland, September 20, 2010. Presentation in Session: Modul 1: Dosimetry and Exposure Assessment.

(4) Murbach M, Kuehn S, Christopoulou M, Christ A, Achermann P, and Kuster N. Evaluation of artifacts by EEG electrodes during RF exposures. In *Abstract Collection of BioEM 2009 Davos, the Joint Meeting of the Bioelectromagnetics Society and the European BioElectromagnetics Association, June 14–19*, Davos, Switzerland, 2009. Presentation 5-2 in Session 5: Dosimetry III (June 16).

(5) Murbach M, Kuehn S, Christopoulou M, Christ A, Achermann P, and Kuster N. Evaluation of artifacts by EEG electrodes during RF exposures. Presentation at the Joint Meeting of the Bioelectromagnetics Society and the European BioElectromagnetics Association (BioEM 2009 Davos), Davos, Switzerland, June 14–19, 2009. Presentation 5-2 in Session 5: Dosimetry III (June 16).

(6) Murbach M, Mevissen M, and Kuster N. Dosimetric assessment of C. elegans exposure in vivo to 900 MHz electromagnetic fields. In *Abstract Collection of BioEM 2009 Davos, the Joint Meeting of the Bioelectromagnetics Society and the European BioElectromagnetics Association, June 14–19*, Davos, Switzerland, 2009. Poster presentation P-40 in Poster session 2: Dosimetry (June 16).

(7) Murbach M, Mevissen M, and Kuster N. Dosimetric assessment of C. elegans exposure in vivo to 900 MHz electromagnetic fields. Poster presentation at the Joint Meeting of the Bioelectromagnetics Society and the European BioElectromagnetics Association (BioEM 2009 Davos), Davos, Switzerland, June 14–19, 2009. Poster presentation P-40 in Poster session 2: Dosimetry (June 16).

(8) Murbach M, Christopoulou M, Christ A, Crespo-Valero P, Zefferer M, Kuehn S, Achermann P, and Kuster N. System to study CNS responses of ELF modulation and cortex versus subcortical

RF exposures. In *Abstract Collection of BioEM 2009 Davos, the Joint Meeting of the Bioelectromagnetics Society and the European BioElectromagnetics Association, June 14–19*, Davos, Switzerland, 2009. Poster presentation P-41 in Poster session 1: Dosimetry (June 15).

(9) Gosselin MC, Neufeld E, Murbach M, Christ A, Cabot E, and Kuster N. Analysis of the SAR enhancement from a multitransmit coil. In *Proceedings of the 10th International Conference of the European Bioelectromagnetics Association (EBEA 2011), February 21–24, 2011*, Rome, Italy, 2011. Presentation in session: Dosimetry (February 23, mcg).

(10) Kuster N, Christ A, Gosselin MC, Oberle M, and Murbach M. MT40: From quadrature feed to multi phase. Presentation at the IEC SC62B MT40 Meeting, Washington, DC, USA, September 14–17, 2010. Presentation.

(11) Neufeld E, Murbach M, Gosselin MC, Christ A, and Kuster N. Human exposures of quadrature feed versus multiphase systems as function of anatomy. Presentation at the IEC SC 62 / MT 40 Meeting, Washington, DC, USA, September 14–17, 2010. Presentation.

(12) Loughran S, Schmid M, Regel S, Bratic A, Maire M, Bersagliere A, Rusterholtz T, Dürr R, Murbach M, Kuster N, and Achermann P. Effects of pulse-modulated RF-EMF on the human brain: Site of interaction. In *Proceedings of the 32nd Annual Meeting of the Bioelectromagnetics Society (BEMS2010), June 14–18, 2010*, Seoul, Korea, 2010. Poster P-B-97 in Poster Session 2: Human Studies (June 17).

(13) Loughran S, Schmid M, Regel S, Bratic A, Maire M, Bersagliere A, Rusterholtz T, Dürr R, Murbach M, Kuster N, and Achermann P. Effects of pulse-modulated RF-EMF on the human brain: Site of interaction. Presentation at the 32nd Annual Meeting of the Bioelectromagnetics Society (BEMS2010), June 14–18, 2010, Seoul, Korea, 2010. Poster P-B-97 in Poster Session 2: Human Studies (June 17).

(14) Schmid M, Bratic A, Loughran S, Regel S, Murbach M, Kuster N, and Achermann P. Effects of pulse-modulated radio frequency electromagnetic fields on the human brain: Critical field parameters. In *Proceedings of the 32nd Annual Meeting of the Bioelectromagnetics Society (BEMS2010), June 14–18, 2010*, Seoul, Korea, 2010. Presentation 12-1 in Session 12: Human Studies & Medical Applications (June 17).

(15) Guionaud C, Alaeddine F, Murbach M, Kuster N, and Mevissen M. Effects of RF-EMF on stress response and alternative splicing in rat and human cell lines. In *Proceedings of the 32nd Annual Meeting of the Bioelectromagnetics Society (BEMS2010), June 14–18, 2010*, Seoul, Korea, 2010. Presentation 14-3 in Session 14: In Vitro Studies (June 18).

(16) Gosselin MC, Murbach M, Kün S, and Kuster N. Multi band mobile phone power control in real environments. In *Programme of the EMF Bordeaux Event (EBEA, COST & URSI 2010), May 26–28, 2010*, pages 53–54, Bordeaux, France, 2010. Presentation in COST Session: RF Strategy in Dosimetry and Exposure Assessment (May 28).

(17) Gosselin MC, Zefferer M, Valero PC, Christ A, Murbach M, Kühn S, and Kuster N. Novel estimation procedure to estimate brain specific SAR in anatomical heads from compliance measurements in SAM. In *Proceedings and Programme of the EMF Bordeaux Event (EBEA, COST & URSI 2010), May 26–28, 2010*, Bordeaux, France, 2010. Poster P3 in Poster Session: Strategies for Dosimetry and Exposure Assessment (May 27).

(18) Gosselin MC, Zefferer M, Valero PC, Christ A, Murbach M, Kühn S, and Kuster N. Novel estimation procedure to estimate brain specific SAR in anatomical heads from compliance measurements in SAM. Presentation at the EMF Bordeaux Event (EBEA, COST & URSI 2010), Bordeaux, France, May 26–28, 2010, 2010. Poster P3 in Poster Session: Strategies for Dosimetry and Exposure Assessment (May 27, Manuel Murbach).

(19) Kyriacou A, Christ A, Neufeld E, Murbach M, Cabot E, Kühn S, Douglas M, and Kuster N. Risk assessment of tissue heat-

ing for wearers of medical implants exposed to electromagnetic fields. In *Proceedings and Programme of the EMF Bordeaux Event (EBEA, COST & URSI 2010), May 26–28, 2010*, Bordeaux, France, 2010. Poster P1 in Poster Session: Strategies for Dosimetry and Exposure Assessment (May 27, not presented).

(20) Alaeddine F, Guionaud C, Murbach M, Kuster N, and Mevissen M. RF-EMF and stress response: Effect of RF-EMF on alternative splicing of acetylcholinesterase. Poster presentation at the Joint Meeting of the Bioelectromagnetics Society and the European BioElectromagnetics Association (BioEM 2009 Davos), Davos, Switzerland, June 14–19, 2009. Poster presentation P-141 in poster session 1: In Vitro Studies (June 15).

(21) Alaeddine F, Guionaud C, Kuster N, Murbach M, and Mevissen M. RF-EMF and stress response: Effect of RF-EMF on alternative splicing of acetylcholinestrase. In *Abstracts of Satellite Symposium BioEM 2009 Davos, NRP 57 Non-Ionising Radiation - Health and Environment, June 14*, Davos, Switzerland, 2009. Presentation 5 in Module 2: Cell Biology (June 14).

(22) Alaeddine F, Guionaud C, Kuster N, Murbach M, and Mevissen M. RF-EMF and stress response: Effect of RF-EMF on alternative splicing of acetylcholinestrase. Presentation at the Satellite Symposium BioEM 2009 Davos, NRP 57 Non-Ionising Radiation - Health and Environment, Davos, Switzerland, June 14, 2009. Presentation 5 in Module 2: Cell Biology (June 14).

(23) Loughran S, Schmid M, Regel S, Bratic A, Murbach M, Kuster N, and Achermann P. Effects of pulse-modulated RF-EMF on the human brain: Critical field parameters, site of interaction and sensitivity in early adolescence. In *Abstracts of Satellite Symposium BioEM 2009 Davos, NRP 57 Non-Ionising Radiation - Health and Environment, June 14*, Davos, Switzerland, 2009. Presentation 7 in Module 3: Laboratory Studies and Epidemiology (June 14).

(24) Loughran S, Schmid M, Regel S, Bratic A, Murbach M, Kuster N, and Achermann P. Effects of pulse-modulated RF-EMF on the human brain: Critical field parameters, site of in-

teraction and sensitivity in early adolescence. Presentation at the Satellite Symposium BioEM 2009 Davos, NRP 57 Non-Ionising Radiation - Health and Environment, Davos, Switzerland, June 14, 2009. Presentation 7 in Module 3: Laboratory Studies and Epidemiology (June 14).

(25) Gosselin MC, Christ A, Murbach M, Ryf S, Kühn S, Christopoulou M, Neufeld E, Gabriel C, Peyman A, and Kuster N. Influences of age dependent tissue parameters and anatomical structures on SAR and temperature increase in the heads of cellular phone users. Presentation at the XXIX General Assembly of URSI 2008, Chicago, IL, USA, August 7–16, 2008. Presentation KAE.9 in Session KAE: Exposure Assessment and Emerging New Technologies (August 15).

(26) Gosselin MC, Christ A, Murbach M, Ryf S, Kühn S, Christopoulou M, Neufeld E, Gabriel C, Peyman A, and Kuster N. Influences of age dependent tissue parameters and anatomical structures on SAR and temperature increase in the heads of cellular phone users. In *Proceedings of the XXIX General Assembly of the International Union of Radio Science (URSIGA 2008), August 7–16*, Chicago, IL, USA, 2008. Presentation KAE.9 in Session KAE: Exposure Assessment and Emerging New Technologies (August 15).

(27) Kuster N, Murbach M, Christopoulou M, Kühn S, and Christ A. Experimental outcome of human provocation studies depend on the design specifics of the exposure setup. Presentation at the XXIX General Assembly of URSI 2008, Chicago, IL, USA, August 7–16, 2008. Presentation K02c.2 in Session K02c: Biological Effects of EMF: Imaging the Human Response (August 15).

(28) Christopoulou M, Murbach M, Christ A, Crespo-Valero P, Zefferer M, Kuehn S, Achermann P, and Kuster N. Exposure systems for testing hypotheses of site and mechanism of interaction in the human brain. In *Abstracts of the 30th Annual Meeting of the Bioelectromagnetics Society (BEMS 2008), June 9–12*, pages 240–241, San Diego, CA, USA, 2008. Poster presentation P-21 in Poster Session: Dosimetry (June 10).

(29) Kuster N, Murbach M, Christopoulou M, Kühn S, and Christ A. Experimental outcome of human provocation studies depend on the design specifics of the exposure setup. In *Proceedings of the XXIX General Assembly of the International Union of Radio Science (URSIGA 2008), August 7–16*, Chicago, IL, USA, 2008. Presentation K02c.2 in Session K02c: Biological Effects of EMF: Imaging the Human Response (August 15).

(30) Christ A, Gosselin MC, Murbach M, Ryf S, Christopoulou M, Neufeld E, Gabriel C, Peyman A, and Kuster N. Age dependent changes in SAR and temperature distribution induced in the user's head by cellular phones. Presentation at the 30th Annual Meeting of the Bioelectromagnetics Society (BEMS 2008), San Diego, CA, USA, June 7–13, 2008. Presentation 7-8 in Session 7: Dosimetry I (June 11).

(31) Christ A, Gosselin MC, Murbach M, Ryf S, Christopoulou M, Neufeld E, Gabriel C, Peyman A, and Kuster N. Age dependent changes in SAR and temperature distribution induced in the user's head by cellular phones. In *Abstracts of the 30th Annual Meeting of the Bioelectromagnetics Society (BEMS 2008), June 7–13*, pages 131–132, San Diego, CA, USA, 2008. Presentation 7-8 in Session 7: Dosimetry I (June 11).

(32) Christ A, Gosselin MC, Murbach M, Kühn S, Zefferer M, Honegger K, Negovetic S, and Kuster N. Age dependent effects of RF electromagnetic fields on the base of relevant biological parameters. Presentation at the DMF-Workshop 'Long Term Effects', Ismaning, Munich, Germany, October 12, 2007.

(33) Murbach M, Gosselin MC, Christ A, Neufeld E, and Kuster N. Report: Development of a methodology to investigate, monitor and control local SAR enhancements for parallel transmit RF coils in MRI scanners: Project 0332. Techreport, IT'IS Foundation, Zeughausstrasse 43, 8004 Zurich, Switzerland, 2010.

(34) Christ A, Oberle M, Kühn S, Murbach M, Capstick M, Cabot E, Kyriacou A, Neufeld E, and Kuster N. MR safety of pacemaker leads: Final report. Techreport, IT'IS Foundation, ETH Zurich, Zeughausstrasse 43, 8004 Zurich, Switzerland, 2009.

(35) Murbach M, Christopoulou M, Kühn S, Neufeld E, Christ A, Achermann P, and Kuster N. System to study CNS responses of ELF modulation and cortex versus subcortical RF exposures: Version 0.8. Techreport, IT'IS Foundation, ETH Zurich, Zeughausstrasse 43, 8004 Zurich, Switzerland, 2009. 25pp.

(36) Murbach M and Kuster N. Dosimetric report for the exposure of reconstituted epidermis within the sXc900 system. Techreport, IT'IS Foundation, ETH Zurich, Zeughausstrasse 43, 8004 Zurich, Switzerland, 2009. 16pp.

(37) Murbach M and Kuster N. Dosimetric report for the exposure of C. elegans within the sXc900 system. Techreport, IT'IS Foundation, ETH Zurich, Zeughausstrasse 43, 8004 Zurich, Switzerland, 2009. 19pp.

(38) Christ A, Schmid G, Djafarzadeh R, Überbacher R, Cecil S, Zefferer M, Neufeld E, Lichtsteiner M, Bouterfas M, and Kuster N. Numerische Bestimmung der Spezifischen Absorptionsrate bei Ganzkörperexposition von Kindern: Projekt stsch4517 Abschlußbericht. Techreport, IT'IS Foundation, ETH Zurich, Zeughausstrasse 43, 8004 Zurich, Switzerland, 2009.

(39) Gosselin MC, Christ A, Ryf S, Murbach M, Kühn S, Christopoulou M, Neufeld E, Cherubini E, Peyman A, Gabriel C, and Kuster N. Untersuchung zu altersabhängigen Wirkungen hochfrequenter elektromagnetischer Felder auf der Basis relevanter biophysikalischer und biologischer Parameter: Abschlussbericht. Techreport, IT'IS Foundation, ETH Zurich, Zeughausstrasse 43, 8004 Zurich, 2009. BfS M8835.

(40) Christ A, Oberle M, Kühn S, Murbach M, Capstick M, Cabot E, Kyriacou A, Neufeld E, and Kuster N. Draft - Final Report: Project 200D Extension: Project 227G - Amendment of March 19th, 2009. Techreport, IT'IS Foundation, ETH Zurich, Zeughausstrasse 43, 8004 Zurich, 2009.

(41) Christ A, Gosselin MC, Ryf S, Murbach M, Kühn S, Christopoulou M, Neufeld E, Cherubini E, Peyman A, Gabriel C,

and Kuster N. Untersuchung zu altersabhängigen Wirkungen hochfrequenter elektromagnetischer Felder auf der Basis relevanter biophysikalischer und biologischer Parameter: Abschlussbericht. Techreport, IT'IS Foundation, ETH Zurich, Zeughausstrasse 43, 8004 Zurich, Switzerland, 2008.

(42) Murbach M, Oberle M, Christ A, Capstick M, and Kuster N. Assessment of the cumulative exposure of children the electromagnetic fields. Presentation of progress report, The Hague, Netherlands, September 28 2009, 2009.

(43) Murbach M. IT'IS exposure systems: Overview. Presentation at visit to Telecommunication Metrology Center, Beijing, China, December 19, 2009, 2009.

(44) Murbach M. IT'IS sXcRF systems. Presentation at visit to Telecommunication Metrology Center, Beijing, China, December 19, 2009, 2009.

(45) Murbach M. IT'IS exposure setups - overview. Presentation at the China Academy of Telecommunication Research visit, Zurich, Switzerland, January 14, 2009.

(46) Murbach M. IT'IS exposure systems: Overview. Presentation at visit to Zheijang University, Hangzhou, China, September 29, 2009, 2009.

Bibliography

[1] ICNIRP. Guidelines for limiting exposure to time-varying electric, magnetic, and electromagnetic fields (up to 300 GHz). *Health Physics*, 74(4):494–522, 1998.

[2] IEEE. IEEE standard for safety levels with respect to human exposure to radio frequency electromagnetic fields, 3 KHz to 300 GHz. *IEEE Standard C95.1-2005*, 2005.

[3] IEC. Medical electrical equipment - particular requirements for the basic safety and essential performance of magnetic resonance equipment for medical diagnosis, 3rd edition. *IEC Standard 60601-2-33*, 2010.

[4] Maxwell J. A dynamical theory of the electromagnetic field. *Philosophical Transactions of the Royal Society of London*, 155:459–512, 1865.

[5] Bloch F, Hansen W, and Packard M. The nuclear induction experiment. *Physical Review*, 70(7-8):474–485, 1946.

[6] Brunner DO, De Zanche N, Fröhlich J, Paska J, and Pruessmann KP. Travelling-wave nuclear magnetic resonance. *Nature*, 457(7232):994–8, 2009.

[7] IEEE. IEEE recommended practice for measurements and computations of radio frequency electromagnetic fields with respect to human exposure to such fields, 100 kHz-300 GHz. *IEEE Standard C95.3-2002 (R2008)*, 2008.

[8] Bottomley PA and Andrew ER. RF magnetic field penetration, phase shift and power dissipation in biological tissue: implications for NMR imaging. *Physics in Medicine and Biology*, 23(4):630–43, 1978.

[9] Shellock FG and Bierman H. The safety of MRI. *JAMA*, 261(23):3412, 1989.

[10] Shellock FG, Schaefer DJ, and Crues JV. Alterations in body and skin temperatures caused by magnetic resonance imaging: is the recommended exposure for radiofrequency radiation too conservative? *The British journal of radiology*, 62(742):904–909, 1989.

[11] Watanabe S, Taki M, Tanaka T, and Watanabe Y. FDTD analysis of microwave hearing effect. *IEEE Transactions on Microwave Theory and Techniques*, 48(11):2126–2132, 2000.

[12] Price DL, De Wilde JP, Papadaki AM, Curran JS, and Kitney RI. Investigation of acoustic noise on 15 MRI scanners from 0.2 T to 3 T. *Journal of Magnetic Resonance Imaging*, 13(2):288–293, 2001.

[13] Leifer MC. Resonant modes of the birdcage coil. *Journal of Magnetic Resonance*, 124:51–60, 1997.

[14] Neufeld E, Gosselin MC, Murbach M, Christ A, Cabot E, and Kuster N. Analysis of the local worst-case SAR exposure caused by an MRI multi-transmit body coil in anatomical models of the human body. *Physics in Medicine and Biology*, 56(15):4649–4659, 2011.

[15] Christ A, Kainz W, Hahn EG, Honegger K, Zefferer M, Neufeld E, Rascher W, Janka R, Bautz W, Chen J, Kiefer B, Schmitt P, Hollenbach HP, Shen J, Oberle M, Szczerba D, Kam A, Guag JW, and Kuster N. The Virtual Family - development of surface-based anatomical models of two adults and two children for dosimetric simulations. *Physics in Medicine and Biology*, 55(2):N23–N38, 2010.

[16] Hasgall PA, Neufeld E, Gosselin MC, Klingenböck A, and Kuster N. IT'IS database for thermal and electromagnetic parameters of biological tissues. Last accessed July 2012. *www.itis.ethz.ch/database*, 2012.

[17] Gabriel S, Lau R, and Gabriel C. The dielectric properties of biological tissues : II . Measurements in the frequency range 10 Hz to 20 GHz. *Physics in Medicine and Biology*, 41:2251–2269, 1996.

[18] Wust P, Nadobny J, Szimtenings M, Stetter E, and Gellermann J. Implications of clinical RF hyperthermia on protection limits in the RF range. *Health Physics*, 92(6):565–573, 2007.

[19] Graven-Nielsen T, Arendt-Nielsen L, and Mense S. Thermosensitivity of muscle: high-intensity thermal stimulation of muscle tissue induces muscle pain in humans. *The Journal of Physiology*, 540(2):647–656, 2002.

[20] Taylor WF, Johnson JM, O'Leary D, and Park MK. Effect of high local temperature on reflex cutaneous vasodilation Effect of high local temperature on reflex cutaneous vasodilation. *J. Appl. Physiol.: Respirat. Environ. Exercise Physiol.*, 57(1):191–196, 1984.

[21] Laakso I and Hirata A. Dominant factors affecting temperature rise in simulations of human thermoregulation during RF exposure. *Physics in Medicine and Biology*, 56(23):7449–7471, 2011.

[22] Foster KR and Adair ER. Modeling thermal responses in human subjects following extended exposure to radiofrequency energy. *Biomedical Engineering Online*, 3:4, 2004.

[23] Sapareto SA and Dewey WC. Thermal dose determination in cancer therapy. *International Journal of Radiation Oncology, Biology, Physics*, 10(6):787–800, 1984.

[24] Dewhirst MW, Viglianti BL, Lora-Michiels M, Hanson M, and Hoopes PJ. Basic principles of thermal dosimetry and thermal

thresholds for tissue damage from hyperthermia. *International Journal of Hyperthermia*, 19(3):267–94, 2003.

[25] Yarmolenko PS, Moon EJ, Landon C, Manzoor A, Hochman DW, Viglianti BL, and Dewhirst MW. Thresholds for thermal damage to normal tissues: an update. *International Journal of Hyperthermia*, 27(4):320–43, 2011.

[26] Neufeld E, Kühn S, Szekely G, and Kuster N. Measurement, simulation and uncertainty assessment of implant heating during MRI. *Physics in Medicine and Biology*, 54(13):4151–69, 2009.

[27] Shrivastava D, Hanson T, Schlentz R, Gallaghar W, Snyder C, Delabarre L, Prakash S, Iaizzo P, and Vaughan JT. Radiofrequency heating at 9.4T: in vivo temperature measurement results in swine. *Magnetic Resonance in Medicine*, 59(1):73–8, 2008.

[28] Brunner DO and Pruessmann KP. B1(+) interferometry for the calibration of RF transmitter arrays. *Magnetic Resonance in Medicine*, 61(6):1480–8, 2009.

[29] Lüdemann L, Wlodarczyk W, Nadobny J, Weihrauch M, Gellermann J, and Wust P. Non-invasive magnetic resonance thermography during regional hyperthermia. *International Journal of Hyperthermia*, 26(3):273–82, 2010.

[30] Marshall J, Martin T, Downie J, and Malisza K. A comprehensive analysis of MRI research risks : in support of full disclosure. *Can. J. Neurol. Sci.*, 34:11–17, 2007.

[31] Personal-Communication. Siemens Medical Solutions. 2007.

[32] Capstick M, McRobbie D, Hand J, Christ A, Kuehn S, Hansson Mild K, Cabot E, Li Y, Melzer A, Papadaki A, Prüssmann K, Quest R, Rea M, Ryf S, Oberle M, and Kuster N. An investigation into occupational exposure to electromagnetic fields for personnel working with and around medical magnetic resonance imaging equipment. *available online*

www.myesr.org/html/img/pool/VT2007017FinalReportv04.pdf, 2007.

[33] Murbach M, Cabot E, Neufeld E, Gosselin MC, Christ A, and Kuster N. Local SAR enhancements in anatomically correct children and adult models as a function of position within 1.5 T MR body coil. *Progress in Biophysics and Molecular Biology*, 107(3):428–433, 2011.

[34] Nadobny J, Szimtenings M, Diehl D, Stetter E, Brinker G, and Wust P. Evaluation of MR-induced hot spots for different temporal SAR modes using a time-dependent temperature gradient treatment. *IEEE Transactions on Biomedical Engineering*, 54(10):1837–1850, 2007.

[35] Christ A, Gosselin MC, Christopoulou M, Kühn S, and Kuster N. Age-dependent tissue-specific exposure of cell phone users. *Physics in Medicine and Biology*, 55(7):1767–83, 2010.

[36] Mosteller R. Simplified calculation of body-surface area. *New England Journal of Medicine*, 317(17):1098, 1987.

[37] Hand JW, Li Y, Thomas EL, Rutherford Ma, and Hajnal JV. Prediction of specific absorption rate in mother and fetus associated with MRI examinations during pregnancy. *Magnetic Resonance in Medicine*, 55(4):883–93, 2006.

[38] Peyman a, Gabriel C, Benedickter HR, and Fröhlich J. Dielectric properties of human placenta, umbilical cord and amniotic fluid. *Physics in Medicine and Biology*, 56(7):N93–8, 2011.

[39] Bakker JF, Paulides MM, Christ A, Kuster N, and van Rhoon GC. Assessment of induced SAR in children exposed to electromagnetic plane waves between 10 MHz and 5.6 GHz. *Physics in Medicine and Biology*, 56(9):2883–2883, 2011.

[40] Benkler S, Chavannes N, and Kuster N. Novel FDTD Huygens source enables highly complex simulation scenarios on ordinary PCs. In *Antennas and Propagation Society International Symposium, 2009. APSURSI'09. IEEE*, number 1, pages 1–4. IEEE, 2009.

[41] Taylor BN and Kuyatt CE. Guidelines for evaluating and expressing the uncertainty of NIST measurement results. *NIST, Gaithersburg, MD, USA, Technical Note 1297*, 1994.

[42] Hand JW, Li Y, and Hajnal JV. Numerical study of RF exposure and the resulting temperature rise in the foetus during a magnetic resonance procedure. *Physics in Medicine and Biology*, 55(4):913–30, 2010.

[43] Murbach M, Neufeld E, Kainz W, Pruessmann KP, and Kuster N. Whole-body and local RF absorption in human models as a function of anatomy and position within 1.5T MR body coil. *Magnetic Resonance in Medicine*, (published online ahead of print), 2013.

[44] Homann H, Börnert P, Eggers H, Nehrke K, Dössel O, and Graesslin I. Toward individualized SAR models and in vivo validation. *Magnetic Resonance in Medicine*, 66(6):1767–76, 2011.

[45] Murbach M, Neufeld E, Capstick M, Kainz W, Brunner DO, Samaras T, Pruessmann KP, and Kuster N. Thermal tissue damage model analyzed for different hole-body SAR and scan durations for standard MR body coils. *Magnetic Resonance in Medicine*, (published online ahead of print), 2013.

[46] Wang Z, Lin JC, Mao W, Liu W, Smith MB, and Collins CM. SAR and temperature: simulations and comparison to regulatory limits for MRI. *Journal of Magnetic Resonance Imaging*, 26(2):437–441, 2007.

[47] Fiala D, Lomas K, and Stohrer M. A computer model of human thermoregulation for a wide range of environmental conditions: the passive system. *Journal of Applied Physiology*, 87(5):1957, 1999.

[48] Lang J, Erdmann B, and Seebass M. Impact of nonlinear heat transfer on temperature control in regional hyperthermia. *IEEE Transactions on Biomedical Engineering*, 46(9):1129–38, 1999.

[49] ISO/TS. 10974:2012, Requirements for the safety of magnetic resonance imaging for patients with an active implantable medical device.

[50] Stolwijk JAJ. Mathematical models of thermal regulation. *Annals of the New York Academy of Sciences*, 335:98–106, 1980.

[51] Barcroft H and Edholm O. The effect of temperature on blood flow and deep temperature in the human forearm. *J. Physiol.*, 102(1):5–20, 1943.

[52] Bernardi P, Cavagnaro M, Pisa S, and Piuzzi E. Specific absorption rate and temperature elevation in a subject exposed in the far-field of radio-frequency sources operating in the 10-900-MHz range. *IEEE Transactions on Biomedical Engineering*, 50(3):295–304, 2003.

[53] Fiala D, Lomas KJ, and Stohrer M. Computer prediction of human thermoregulatory and temperature responses to a wide range of environmental conditions. *International Journal of Biometeorology*, 45(3):143–59, 2001.

[54] Neufeld E, Chavannes N, Samaras T, and Kuster N. Novel conformal technique to reduce staircasing artifacts at material boundaries for FDTD modeling of the bioheat equation. *Physics in Medicine and Biology*, 52(15):4371–81, 2007.

[55] Wust P, Stahl H, Löffel J, Seebass M, Riess H, and Felix R. Clinical, physiological and anatomical determinants for radiofrequency hyperthermia. *International Journal of Hyperthermia*, 11(2):151–67, 2000.

[56] Paprottka FJ, Machens HG, and Lohmeyer JA. Third-degree burn leading to partial foot amputation - Why a notebook is no laptop. *Journal of plastic, reconstructive & aesthetic surgery : JPRAS*, pages 10–13, 2012.

[57] Shellock FG and Crues JV. Radiology MR procedures : biologic effects, safety, and patient care. *Radiology*, 232:635–652, 2004.

[58] Kikuchi S, Saito K, Takahashi M, Ito K, and Ikehira H. SAR computation inside fetus by RF coil during MR imaging employing realistic numerical pregnant woman model. *IEICE Transactions on Communications*, E92-B(2):431–439, 2009.

[59] Pediaditis M, Leitgeb N, and Cech R. RF-EMF exposure of fetus and mother during magnetic resonance imaging. *Physics in Medicine and Biology*, 53(24):7187–95, 2008.

[60] Voigt T, Homann H, Katscher U, and Doessel O. Patient-individual local SAR determination: In vivo measurements and numerical validation. *Magnetic Resonance in Medicine*, 000, 2011.

[61] van den Bergen B, van den Berg CaT, Klomp DWJ, and Lagendijk JJW. SAR and power implications of different RF shimming strategies in the pelvis for 7T MRI. *Journal of Magnetic Resonance Imaging*, 30(1):194–202, 2009.

[62] Borbely A, Huber R, Graf T, Fuchs B, Gallmann E, and Achermann P. Pulsed high-frequency electromagnetic field affects human sleep and sleep electroencephalogram. *Neuroscience Letters*, 275:207–210, 1999.

[63] Huber R, Graf T, Cote KA, Wittmann L, Gallmann E, Matter D, Schuderer J, Kuster N, Borbély AA, and Achermann P. Exposure to pulsed high-frequency electromagnetic field during waking affects human sleep EEG. *NeuroReport*, 11(15):3321–3325, 2000.

[64] Regel SJ, Tinguely G, Schuderer J, Adam M, Kuster N, Landolt HP, and Achermann P. Pulsed radio-frequency electromagnetic fields: Dose-dependent effects on sleep, the sleep EEG and cognitive performance. *Journal of Sleep Research*, 16(3):253–258, 2007.

[65] Schmid MR, Loughran SP, Regel SJ, Murbach M, Bratic Grunauer A, Rusterholz T, Bersagliere A, Kuster N, and Achermann P. Sleep EEG alterations: effects of different pulse-modulated radio frequency electromagnetic fields. *Journal of Sleep Research*, 21(1):50–58, 2012.

[66] Schmid MR, Murbach M, Lustenberger C, Maire M, Kuster N, Achermann P, and Loughran SP. Sleep EEG alterations: effects of pulsed magnetic fields versus pulse-modulated radio

frequency electromagnetic fields. *Journal of Sleep Research*, 21(6):620–629, 2012.

[67] Loughran S, Benz D, Schmid MR, Murbach M, Kuster N, and Achermann P. No increased sensitivity in brain activity of adolescents exposed to mobile phone-like emissions. *Clinical Neurophysiology*, (published online ahead of print), 2013.

[68] Loughran SP, Wood AW, Barton JM, Croft RJ, Thompson B, and Stough C. The effect of electromagnetic fields emitted by mobile phones on human sleep. *NeuroReport*, 16(17):1973–1976, 2005.

[69] Volkow ND, Vaska P, Fowler JS, Telang F, Alexoff D, Logan J, and Wong C. Effects of cell phone radiofrequency signal exposure on brain glucose metabolism. *JAMA*, 305(8):808–813, 2011.

[70] Lehmann H, Pollara L, Spichtig S, Kühn S, and Wolf M. Head exposure system for a human provocation study to assess the possible influence of UMTS-like electromagnetic fields on cerebral blood circulation using near-infrared imaging. *Bioelectromagnetics*, (June), 2011.

[71] Regel SJ, Negovetic S, Röösli M, Berdiñas V, Schuderer J, Huss A, Lott U, Kuster N, and Achermann P. UMTS base station-like exposure, well-being, and cognitive performance. *Environmental Health Perspectives*, 114(8):1270–1275, 2006.

[72] Wood AW, Loughran SP, and Stough C. Does evening exposure to mobile phone radiation affect subsequent melatonin production? *International Journal of Radiation Biology*, 82(2):69–76, 2006.

[73] Kühn S and Kuster N. Field evaluation of the human exposure from multiband , multisystem mobile phones. *IEEE Transactions on Electromagnetic Compatibility*, 55(2):275–287, 2013.

[74] Hirata A and Shiozawa T. Correlation of maximum temperature increase and peak SAR in the human head due to handset

antennas. *IEEE Transactions on Microwave Theory and Techniques*, 51(7):1834–1841, 2003.

[75] Lin JC. Hearing microwaves : the microwave auditory phenomenon. *IEEE Antennas ond Propagation Magazine*, 43(6):6–8, 2001.

[76] Lustenberger C, Murbach M, Dürr R, Schmid MR, Kuster N, Achermann P, and Huber R. Stimulation of the brain with radiofrequency electromagnetic field pulses affects sleep-dependent performance improvement. *Brain Stimulation*, 6(5):805–811, 2013.

[77] Loughran SP, McKenzie RJ, Jackson ML, Howard ME, and Croft RJ. Individual differences in the effects of mobile phone exposure on human sleep: rethinking the problem. *Bioelectromagnetics*, 33(1):86–93, 2012.

[78] Murbach M, Christopoulou M, Crespo-Valero P, Achermann P, and Kuster N. Exposure system to study hypotheses of ELF and RF electromagnetic field interactions of mobile phones with the central nervous system. *Bioelectromagnetics*, 33(6):527–533, 2012.

[79] Borbély A, Huber R, Graf T, Fuchs B, Gallmann E, and Achermann P. Pulsed high-frequency electromagnetic field affects human sleep and sleep electroencephalogram. *Neuroscience Letters*, 275(3):207–210, 1999.

[80] Huber R, Graf T, Cote KA, Wittmann L, Gallmann E, Matter D, Schuderer J, Kuster N, Borbély A, and Achermann P. Exposure to pulsed high-frequency electromagnetic field during waking affects human sleep EEG. *NeuroReport*, 11(15):3321–3325, 2000.

[81] Huber R, Treyer V, Borbély A, Schuderer J, Gottselig JM, Landolt HP, Werth E, Berthold T, Kuster N, Buck A, and Achermann P. Electromagnetic fields, such as those from mobile phones, alter regional cerebral blood flow and sleep and waking EEG. *Journal of Sleep Research*, 11(4):289–295, 2002.

[82] Regel SJ, Tinguely G, Schuderer J, Adam M, Kuster N, Landolt HP, and Achermann P. Pulsed radio-frequency electromagnetic fields: dose-dependent effects on sleep, the sleep EEG and cognitive performance. *Journal of Sleep Research*, 16(3):253–258, 2007.

[83] Bernardi P. Specific absorption rate and temperature increases in the head of a cellular-phone user. *IEEE Transactions on Microwave Theory and Techniques*, BME-31(2):120–1126, 2000.

[84] Samaras T, Kalampaliki E, and Sahalos JN. Influence of thermophysiological parameters on the calculations of temperature rise in the head of mobile phone users. *IEEE Transactions on Electromagnetic Compatibility*, 49(4):936–939, 2007.

[85] Huber R, Treyer V, Schuderer J, Berthold T, Buck A, Kuster N, Landolt HP, and Achermann P. Exposure to pulse-modulated radio frequency electromagnetic fields affects regional cerebral blood flow. *European Journal of Neuroscience*, 21(4):1000–1006, 2005.

[86] Kuster N, Schuderer J, Christ A, Futter P, and Ebert S. Guidance for exposure design of human studies addressing health risk evaluations of mobile phones. *Bioelectromagnetics*, 25(7):524–9, 2004.

[87] Boutry CM, Kühn S, Achermann P, Romann A, Keshvari J, and Kuster N. Dosimetric evaluation and comparison of different RF exposure apparatuses used in human volunteer studies. *Bioelectromagnetics*, 29(1):11–19, 2008. published online August 10, 2007.

[88] Ebert S. *EMF Risk Assessment: Exposure Systems for Large-Scale Laboratory and Experimental Provocation Studies*. phdthesis, Swiss Federal Institute of Technology, Zurich, Switzerland, Hartung-Gorre Verlag Konstanz. Germany, 2009. ETHZ PhD Thesis, Defense: 29 September 2009.

[89] Crespo-Valero P, Christopoulou M, Zefferer M, Christ A, Achermann P, Nikita KS, and Kuster N. Novel methodology to

characterize electromagnetic exposure of the brain. *Physics in Medicine and Biology*, 56(2):383–396, 2010.

[90] Huber R, Schuderer J, Graf T, Jütz K, Borbély A, Kuster N, and Achermann P. Radio frequency electromagnetic field exposure in humans: Estimation of SAR distribution in the brain, effects on sleep and heart rate. *Bioelectromagnetics*, 24(4):262–276, 2003.

[91] Murbach M, Neufeld E, Christopoulou M, Achermann P, and Kuster N. Evaluation of electrode artifacts and thermal ripples of EEG RF experiments. *Bioelectromagnetics*, submitted, 2013.

[92] Reiser H, Dimpfel W, and Schober F. The influence of electromagnetic fields on human brain activity. *European Journal of Medical Research*, 1(1):27–32, 1995.

[93] Croft RJ, Chandler JS, Burgess AP, Barry RJ, Williams JD, and Clarke AR. Acute mobile phone operation affects neural function in humans. *Clinical Neurophysiology*, 113(10):1623–1632, 2002.

[94] Curcio G, Ferrara M, Moroni F, D'Inzeo G, Bertini M, and De Gennaro L. Is the brain influenced by a phone call? An EEG study of resting wakefulness. *Neuroscience Research*, 53(3):265–270, 2005.

[95] Van Rongen E, Croft R, Juutilainen J, Lagroye I, Miyakoshi J, Saunders R, De Seze R, Tenforde T, Verschaeve L, Veyret B, and Xu Z. Effects of radiofrequency electromagnetic fields on the human nervous system. *Journal of Toxicology and Environmental Health, Part B*, 12(8):572–597, 2009.

[96] Krause CM, Björnberg CH, Pesonen M, Hulten A, Liesivuori T, Koivisto M, Revonsuo A, Laine M, and Hämäläinen H. Mobile phone effects on children's event-related oscillatory EEG during an auditory memory task. *International Journal of Radiation Biology*, 82(6):443–450, 2006.

[97] Schmid G, Cecil S, Goger C, Trimmel M, Kuster N, and Molla-Djafari H. New head exposure system for use in human provocation studies with EEG recording during GSM900- and UMTS-like exposure. *Bioelectromagnetics*, 28(8):636–647, 2007.

[98] Angelone LM, Bit-Babik G, and Chou CK. Computational electromagnetic analysis in a human head model with EEG electrodes and leads exposed to RF-field sources at 915 MHz and 1748 MHz. *Radiation Research*, 174(1):91–100, 2010.

[99] Christopoulou M, Kazasidis O, and Nikita KS. Numerical assessment of EEG electrode artifacts during EMF exposure in human provocation studies. *Wireless Mobile Communication and Healthcare, Lecture Notes of the Institute for Computer Sciences, Social Informatics and Telecommunications Engineering*, 83:408–415, 2012.

[100] Johnson C and Guy A. Nonionizing electromagnetic wave effects in biological materials and systems. *Proceedings of the IEEE*, 60(6):692–718, 1972.

[101] Drossos A, Santomaa V, and Kuster N. Absorption upon human head tissue composition in the frequency range of 300-3000 MHz. *IEEE Transactions on Microwave Theory and Techniques*, 48(11):1988–1995, 2000.

[102] Regel SJ, Gottselig JM, Schuderer J, Tinguely G, Rétey JV, Kuster N, Landolt HP, and Achermann P. Pulsed radio frequency radiation affects cognitive performance and the waking electroencephalogram. Technical Report 8, University of Zürich, Institute of Pharmacology and Toxicology, Zürich, Switzerland., 2007.

[103] Croft RJ, Hamblin DL, Spong J, Wood aW, McKenzie RJ, and Stough C. The effect of mobile phone electromagnetic fields on the alpha rhythm of human electroencephalogram. *Bioelectromagnetics*, 29(1):1–10, 2008.

[104] Regel SJ and Achermann P. Cognitive performance measures in bioelectromagnetic research–critical evaluation and recommen-

dations. *Environmental health : a global access science source*, 10(1):10, 2011.

[105] Diekelmann S and Born J. The memory function of sleep. *Nature Reviews Neuroscience*, 11(2):114–126, 2010.

[106] Gais S, Mölle M, Helms K, and Born J. Learning-dependent increases in sleep spindle density. Technical Report 15, Department of Neuroendocrinology, University of Lübeck, 23564 Lübeck, Germany., 2002.

[107] Schabus M, Hödlmoser K, Gruber G, Sauter C, Anderer P, Klösch G, Parapatics S, Saletu B, Klimesch W, and Zeitlhofer J. Sleep spindle-related activity in the human EEG and its relation to general cognitive and learning abilities. *European Journal of Neuroscience*, 23(7):1738–1746, 2006.

[108] Huber R, Ghilardi MF, Massimini M, Ferrarelli F, Riedner BA, Peterson MJ, and Tononi G. Arm immobilization causes cortical plastic changes and locally decreases sleep slow wave activity. *Nature Neuroscience*, 9(9):1169–1176, 2006.

[109] Huber R, Ghilardi MF, Massimini M, and Tononi G. Local sleep and learning. *Nature*, 430(6995):78–81, 2004.

[110] Hill S, Tononi G, and Ghilardi MF. Sleep improves the variability of motor performance. *Brain Research Bulletin*, 76(6):605–611, 2008.

[111] Steriade M, Nuñez A, and Amzica F. A novel slow (¡ 1 Hz) oscillation of neocortical neurons in vivo: depolarizing and hyperpolarizing components. *Journal of Neuroscience*, 13(8):3252–3265, 1993.

[112] Borbély AA and Achermann P. Sleep homeostasis and models of sleep regulation. *Journal of Biological Rhythms*, 14(6):557–568, 1999.

[113] Steriade M. Grouping of brain rhythms in corticothalamic systems. *Neuroscience*, 137(4):1087–1106, 2006.

[114] De Gennaro L and Ferrara M. Sleep spindles : an overview. *Sleep Medicine*, 7(5):423–440, 2003.

[115] Walker MP, Brakefield T, Morgan A, Hobson JA, and Stickgold R. ScienceDirect - Neuron : Practice with Sleep Makes Perfect: Sleep-Dependent Motor Skill Learning. *Neuron*, 35:205–211, 2002.

[116] Driver HS, Dijk DJ, Werth E, Biedermann K, and Borbély AA. Sleep and the sleep electroencephalogram across the menstrual cycle in young healthy women. *The Journal of Clinical Endocrinology & Metabolism*, 81(2):728–735, 1996.

[117] Iber C, Ancoli-Israel S, Chesson A, and Quan SF. *The AASM Manual for the Scoring of Sleep and Associated Events: Rules, Terminology and Technical Specifications*. American Academy of Sleep Medicine, 2007.

[118] Delorme A and Makeig S. EEGLAB: an open source toolbox for analysis of single-trial EEG dynamics including independent component analysis. *Journal of Neuroscience Methods*, 134(1):9–21, 2004.

[119] Pfurtscheller G and Lopes Da Silva FH. Event-related EEG/MEG synchronization and desynchronization: basic principles. *Clinical Neurophysiology*, 110(11):1842–1857, 1999.

[120] Barrett G, Neshige R, and Shibasaki H. Auditory event-related dynamics of the EEG spectrum and effects of exposure to tones. *Electroencephalography and Clinical Neurophysiology*, 66(4):409–419, 1987.

[121] Tallon-Baudry C, Bertrand O, Delpuech C, and Pernier J. Stimulus specificity of phase-locked and non-phase-locked 40 Hz visual responses in human. *Journal of Neuroscience*, 16(13):4240–9, 1996.

[122] Makeig S, Debener S, Onton J, and Delorme A. Mining event-related brain dynamics. *Trends in Cognitive Sciences*, 8(5):204–210, 2004.

[123] Brawn TP, Fenn KM, Nusbaum HC, and Margoliash D. Consolidating the effects of waking and sleep on motor-sequence learning. *Journal of Neuroscience*, 30(42):13977–13982, 2010.

[124] Rickard TC, Cai DJ, Rieth CA, Jones J, and Ard MC. Sleep does not enhance motor sequence learning. *Journal of experimental psychology Learning memory and cognition*, 34(4):834–842, 2008.

[125] Marshall L, Helgadóttir H, Mölle M, and Born J. Boosting slow oscillations during sleep potentiates memory. Technical Report 7119, University of Lübeck, Department of Neuroendocrinology, Haus 23a, Ratzeburger Allee 160, 23538 Lübeck, Germany. marshall@kfg.uni-luebeck.de, 2006.

[126] Ozen S, Sirota A, Belluscio MA, Anastassiou CA, Stark E, Koch C, and Buzsáki G. Transcranial electric stimulation entrains cortical neuronal populations in rats. *The Journal of Neuroscience*, 30(34):11476–11485, 2010.

[127] Vyazovskiy VV, Olcese U, Lazimy YM, Faraguna U, Esser SK, Williams JC, Cirelli C, and Tononi G. Cortical firing and sleep homeostasis. *Neuron*, 63(6):865–878, 2009.

[128] Vyazovskiy VV, Cirelli C, and Tononi G. Electrophysiological correlates of sleep homeostasis in freely behaving rats. *Progress in Brain Research*, 193(608):17–38, 2011.

[129] Aeschbach D and Borbely AA. All-night dynamics of the human sleep EEG. *Journal of Sleep Research*, 2(2):70–81, 1993.

[130] Carrubba S, Frilot C, Chesson AL, and Marino AA. Evidence of a nonlinear human magnetic sense. Technical Report 1, Department of Orthopedic Surgery, Louisiana State University Health Sciences Center, P.O. Box 33932, 1501 Kings Highway, Shreveport, LA 71130-3932, USA., 2007.

[131] Anastassiou CA, Perin R, Markram H, and Koch C. Ephaptic coupling of cortical neurons. *Nature Neuroscience*, 14(2):217–223, 2011.

[132] Tononi G and Cirelli C. Sleep function and synaptic homeostasis. *Sleep Medicine Reviews*, 10(1):49–62, 2006.

[133] Vyazovskiy VV, Cirelli C, Pfister-Genskow M, Faraguna U, and Tononi G. Molecular and electrophysiological evidence for net synaptic potentiation in wake and depression in sleep. *Nature Neuroscience*, 11(2):200–208, 2008.

[134] Ferreri F, Curcio G, Pasqualetti P, De Gennaro L, Fini R, and Rossini PM. Mobile phone emissions and human brain excitability. *Annals of Neurology*, 60(2):188–196, 2006.

[135] Czarnecki A, Birtoli B, and Ulrich D. Cellular mechanisms of burst firing-mediated long-term depression in rat neocortical pyramidal cells. *The Journal of Physiology*, 578(Pt 2):471–479, 2007.

[136] Landolt HP, Dijk DJ, Gaus SE, and Borbély AA. Caffeine reduces low-frequency delta activity in the human sleep EEG. *Neuropsychopharmacology*, 12(3):229–238, 1995.

[137] Lin J. The microwave auditory phenomenon. *Proceedings of the IEEE*, 68(1):67–73, 1980.

[138] Costa FP, de Oliveira aC, Meirelles R, Machado MCC, Zanesco T, Surjan R, Chammas MC, de Souza Rocha M, Morgan D, Cantor a, Zimmerman J, Brezovich I, Kuster N, Barbault a, and Pasche B. Treatment of advanced hepatocellular carcinoma with very low levels of amplitude-modulated electromagnetic fields. *British Journal of Cancer*, pages 1 – 9, 2011.

[139] Murbach M, Neufeld E, Pruessmann KP, and Kuster N. Safe MR scan times based on CEM43 tissue damage thresholds, using electromagnetic and thermal simulations with anatomically correct human models and considering local thermoregulation. In *Proceedings ISMRM*, page 2140, 2012.

Curriculum Vitae

Personal Information

- **Date of birth** July 26th, 1979
- **Place of birth** Zürich, Switzerland
- **Citizenship** Swiss
- **Parents** Lea and Herbert Murbach

Education

- **Kantonsschule am Burggraben, St. Gallen, Schweiz**
  1993 - 1998
- **Department of Information Technology and Electrical Engineering, ETH Zurich, Switzerland**
  1999 - 2004
- **Master of Advanced Studies in Secondary and Higher Education (MAS SHE, "Höheres Lehramt") , ETH Zurich, Switzerland**
  2004 - 2005

- **Foundation for Research on Information Technologies in Society, Zurich, Switzerland**
  Scientific Assistant
  2007 - 2008

- **Foundation for Research on Information Technologies in Society, Zurich, Switzerland**
  PhD Studies
  2008 - 2013

Awards

- **Best Student Platform Presentation Award of the Bioelectromagnetics Society,**
  BioEM 2009, Davos, Switzerland
  2009

- **Best Poster Award of the Bioelectromagnetics Society, BioEM 2009, Davos, Switzerland**
  2009

- **Best Student Platform Presentation Award at the 4th International Workshop on Computational Phantoms, CP 2013, Zurich, Switzerland**
  2013

Theses & Internships

- **Industrial Internship, Benninger AG**
  Uzwil, Switzerland
  February - May 2004

- **Temporary R&D Assisstant, Leica Geosystems AG**
  Heerbrugg, Switzerland
  May - September 2005

- **Semester Thesis: Hivoltage Lab**
  ETH Zurich, Switzerland
  Supervisor: Wolfgang Hribernik
  2003

- **Semester Thesis: NIRS**
  ETH Zurich, Switzerland
  Supervisor: Dr. Martin Wolf
  2004

- **Master Thesis: Electromagnetic Compatibility (EMC): Cerebral Hemodynamic Effects of Cellular Phone Use**
  Supervisor: Dr. Martin Wolf
  2004